

2015

CHARACTERIZATION OF TRANSPORT AND TRANSFORMATION OF AIR POLLUTANTS OBSERVED IN THE FREE TROPOSPHERE OVER THE CENTRAL NORTH ATLANTIC

Bo Zhang
Michigan Technological University

Follow this and additional works at: <https://digitalcommons.mtu.edu/etds>

 Part of the [Other Chemistry Commons](#)


Copyright 2015 Bo Zhang

Recommended Citation

Zhang, Bo, "CHARACTERIZATION OF TRANSPORT AND TRANSFORMATION OF AIR POLLUTANTS OBSERVED IN THE FREE TROPOSPHERE OVER THE CENTRAL NORTH ATLANTIC", Dissertation, Michigan Technological University, 2015.

<https://doi.org/10.37099/mtu.dc.etds/1018>

Follow this and additional works at: <https://digitalcommons.mtu.edu/etds>

 Part of the [Other Chemistry Commons](#)

CHARACTERIZATION OF TRANSPORT AND TRANSFORMATION OF AIR
POLLUTANTS OBSERVED IN THE FREE TROPOSPHERE OVER THE
CENTRAL NORTH ATLANTIC

By

Bo Zhang

A DISSERTATION

Submitted in partial fulfillment of the requirements for the degree of

DOCTOR OF PHILOSOPHY

In Atmospheric Sciences

MICHIGAN TECHNOLOGICAL UNIVERSITY

2015

© 2015 Bo Zhang

This dissertation has been approved in partial fulfillment of the requirements for the Degree of DOCTOR OF PHILOSOPHY in Atmospheric Sciences.

Department of Civil and Environmental Engineering

Dissertation Co-advisor: *Dr. Judith Perlinger*

Dissertation Co-advisor: *Dr. R. Chris Owen*

Committee Member: *Dr. Louisa Kramer*

Committee Member: *Dr. Lynn Mazzoleni*

Committee Member: *Dr. Noel Urban*

Department Chair: *Dr. David Hand*

Dedication

To my parents

who named me a "doctor" ("Bo" has a meaning of "doctor" in Chinese), which has always been encouraging me in my life as a student and will do the same in the future.

Contents

List of Figures	xiii
List of Tables	xvii
Preface	xix
Acknowledgments	xxi
Abstract	xxiii
1 Introduction	1
1.1 Background	1
1.1.1 Tropospheric ozone	2
1.1.2 Tropospheric aerosol age	6
1.1.3 Modeling tools	8
1.1.4 Previous research at PMO	10
1.2 Research objectives	12
1.3 Dissertation overview	14

2	A Semi-Lagrangian view of ozone production tendency in North American outflow	15
2.1	Introduction	16
2.2	Methods	19
2.2.1	Pico Mountain Observatory and measurements	19
2.2.2	Application of FLEXPART	22
2.2.3	Application of GEOS-Chem	24
2.2.4	Folded GEOS-Chem and FLEXPART technique	26
2.3	Characteristics of North American transport events during summers 2009 and 2010	30
2.3.1	Criteria applied for transport event identification	30
2.3.1.1	Elevated CO	30
2.3.1.2	$d[O_3]/d[CO]$	33
2.3.1.3	Transport pathway	34
2.3.1.4	Anthropogenic versus fire emission impacts	35
2.3.1.5	Upslope flow	36
2.3.1.6	Capture of events in GEOS-Chem	37
2.3.2	Characteristics of transport plumes and quantified events	37
2.3.3	Simulation of transport for selected events	39
2.3.3.1	FLEXPART folded retroplumes	39
2.3.3.2	Tagged CO simulations	41

2.3.3.3	NMHC aging in the folded GEOS-Chem and FLEX- PART results	43
2.4	Ozone production tendency in North American outflows	46
2.4.1	Event 2 (9–15 June 2009)	46
2.4.2	Event 6 (16–21 July 2010)	54
2.5	Potential causes for enhancement in $d[O_3]/d[CO]$ at PMO	56
2.5.1	$d[O_3]/d[CO]$ evolution during transport of Event 2	57
2.5.2	$d[O_3]/d[CO]$ evolution during transport of Event 6	64
2.6	Conclusions	67
3	Ten-year chemical signatures associated with long range transport observed in the free troposphere over the central North Atlantic	71
3.1	Introduction	72
3.2	Method	75
3.2.1	PMO introduction and measurements	75
3.2.2	Transport and pollution tracer simulations	77
3.2.3	Classification of transport patterns	78
3.2.3.1	Air mass origin	81
3.2.3.2	Impact of pollution emissions and air mass age	82
3.2.3.3	Transport height	85
3.2.3.4	Potential upslope flow	86
3.3	Transport patterns and chemical signatures	87

3.3.1	North Atlantic free troposphere background	91
3.3.2	Transport affected by North America anthropogenic emissions	93
3.3.3	Transport affected by wildfires	98
3.3.4	Transport from the upper troposphere and stratosphere . . .	100
3.3.5	Transport affected by upslope flow	102
3.4	Relationships among observed trace gases	103
3.4.1	$d[O_3]/d[CO]$	104
3.4.2	Oxidation of butane isomers	108
3.4.3	NMHC photochemical clock	109
3.5	Conclusions	116
4	Ages and sources of aerosol ^{210}Po collected in the free troposphere	
	over the central North Atlantic	119
4.1	Introduction	120
4.2	Methods	123
4.2.1	Aerosol sampling at PMO	123
4.2.2	^{210}Po Alpha spectrometry	124
4.2.3	Measured particle mass concentration	127
4.2.4	Transport trajectory simulation and estimation of pollution	
	sources	127
4.3	Results and discussions	129
4.3.1	Time series results	129

4.3.2	African dust impacts	132
4.3.3	Estimated aerosol age at PMO	135
4.4	Conclusions and suggestions for methods improvement	144
5	Conclusions and future research	147
5.1	Ozone production tendency during transport from North American to PMO	148
5.2	Characterization of chemical signatures for different transport pat- terns	149
5.3	Aerosol atmospheric residence time estimated using radionuclide trac- ers	150
5.4	Future research	152
	References	155
A	Technical instructions for running FLEXPART 8.2	171
A.1	Setup	171
A.2	Modified files	172
A.3	Meteorology	173
A.4	IDL programs for running FLEXPART8.2 and visualizing the standard output	173
A.4.1	Backward simulation	173
A.4.2	Forward simulation	174

A.5	Folded FLEXPART	176
A.5.1	Folding FLEXPART retroplumes with forward results	176
A.5.2	Folding FLEXPART retroplumes with emission inventories .	176
B	Technical requirements for using Sheppard’s model	177
C	Letters of Permission	179

List of Figures

1.1	Long-range transport to the central North Atlantic	11
2.1	Time series of chemical measurements and model results	20
2.2	Same as Fig. 2.1 but for summer 2010.	21
2.3	FLEXPART folded retroplumes	40
2.4	Tagged North American CO simulation results for FLEXPART and GEOS-Chem at three upwind times	42
2.5	Relationship between the natural logarithms of NMHCs in folded re- sults during transport	45
2.6	Folded results (UFQs) of pollution plumes at each model time step during Event 2 and 6	47
2.7	GEOS-Chem profiles of tracer gases, ozone production/loss rates, OH concentration and specific humidity (SPHU) at four upwind times along the transport pathway for Event 2	51
2.8	Same format as in Fig. 2.7, but for Event 6 in 2010.	52
2.9	GEOS-Chem-simulated ozone mixing ratio and surface pressure at the arrival time of Event 2	53

2.10	Calculations of dO_3/dCO for the two selected events	58
3.1	Coverage of trace gas observations at PMO	76
3.2	FLEXPART simulated summertime column integrated residence time for determined transport patterns	83
3.3	FLEXPART CO contributions from different sources	84
3.4	FLEXPART simulated summertime column integrated residence time for determined transport patterns	92
3.5	Annual variation of trace gas enhancements	97
3.6	RMA regression results of observed ozone and CO relationship . . .	106
3.7	Same as Figure 3.6, but for summer.	107
3.8	Same as Figure 3.6, but for fall.	107
3.9	Butane isomers observed for frequent transport patterns	110
3.10	Same as Figure 3.9, but for summer.	111
3.11	Same as Figure 3.9, but for fall.	112
3.12	Relationships between $\ln([\text{n-butane}]/[\text{ethane}])$ and $\ln([\text{propane}]/[\text{ethane}])$ for the frequent transport patterns	113
3.13	Same as Figure 3.12, but for summer.	114
3.14	Same as Figure 3.12, but for fall.	115
4.1	Decay chain of ^{222}Rn and radioactive half-lives of its progeny	121
4.2	Time series results of ^{210}Po activity for May and June of 2013. . . .	130
4.3	Same as Figure 4.2, but for July and August of 2013 (b).	131

4.4	FLEXPART simulated CO contributions from anthropogenic emissions of different continents and global wildfire emissions	134
4.5	Relationships between FLEXPART simulated CO contribution . . .	135
4.6	Column-integrated residence time distribution of FLEXPART retro- plumes for two events	136
4.7	Particle equivalent black carbon mass concentration measured by Aethalometer for July and August 2013.	137
4.8	Distribution of aerosol atmospheric residence times.	138
4.9	Relationships between observed ^{210}Po activities and residence time ra- tios	139
4.10	Relationships between estimated aerosol ages and particle mass con- centrations	140

List of Tables

2.1	Summary of analysis used to identify events resulting from anthropogenic outflows from North America.	32
3.1	Constraints to define transport patterns	79
3.2	Statistics of carbon monoxide, ozone, nitrogen oxides and NMHCs for the determined transport patterns in summer	89
4.1	A summary of estimated atmospheric aerosol ages using $^{210}Po/^{210}Pb$ ratios	141

Preface

This dissertation is based on the measurements and modeling work conducted for Pico Mountain Observatory.

Chapter 2. This chapter has been published as Zhang, B., Owen, R. C., Perlinger, J. A., Kumar, A., Wu, S., Val Martín, M., Kramer, L., Helmig D., Honrath, R. E. (2014). A semi-Lagrangian view of ozone production tendency in North American outflow in the summers of 2009 and 2010. *Atmospheric Chemistry and Physics*, 14(5), 2267-2287. Chris Owen, María Val Martín, Detlev Helmig, Louisa Kramer, Mike Dziobak and Richard Honrath provided field data collection. Aditya Kumar and Shiliang Wu provided GEOS-Chem modeling results and wrote the introduction section for GEOS-Chem. I did data analysis and FLEXPART modeling under the guidance of Judith Perlinger and Chris Owen. I wrote the manuscript for publication. Judith Perlinger and Chris Owen carefully reviewed the manuscript. All the authors provided valuable comments before the manuscript was submitted for publication.

Chapter 3. This chapter is based on the material that is intended for publication as Zhang et al., Ten-year chemical signatures associated with long range transport observed in the free troposphere over the central North Atlantic. Chris Owen, Paulo Fialho, Detlev Helmig, María Val Martín, Louisa Kramer, Mike Dziobak and Richard

Honrath provided field data. Chris Owen and I conducted FLEXPART simulations. I developed the method and conducted data analysis under the guidance of Judith Perlinger and Chris Owen.

Chapter 4. This chapter is based on the material that is intended for publication as Zhang et al., Ages and sources of aerosol ^{210}Po collected in the free troposphere over the central North Atlantic. Paulo Fialho, Detlev Helmig, Lynn Mazzoleni, Claudio Mazzoleni, Katja Džepina and Mike Dziobak provided field data. Noel Urban and I developed the method and conducted lab experiments. Judith Perlinger, Chris Owen and Lynn Mazzoleni provided valuable comments for the work.

Acknowledgments

I would like to thank my advisor, Dr. Judith Perlinger, for her patience, guidance and support during my study period at Michigan Tech. Besides the knowledge I learn from her, I also gained precious experience and skills in doing research, including scientific thinking, data analysis and writing through her advising. I would also like to thank my co-advisor, Dr. Chris Owen (EPA, U.S.), who introduced me to atmospheric modeling, shared his modeling expertise with me and contributed to FLEXPART installation at Michigan Tech University. I thank my research committee members (Dr. Noel Urban, Dr. Louisa Kramer and Dr. Lynn Mazzoleni) for sharing their knowledge and suggestions to help me complete this work. Dr. Noel Urban introduced me to the field of atmospheric radionuclides. Dr. Louisa Kramer helped me a lot when I started to learn computer languages and programming. Dr. Lynn Mazzoleni educated me about analytical instruments for aerosol measurements and provided valuable insights in atmospheric aerosols.

I would like to extend my thanks to the scientists who have helped and interacted with me in research related to the Pico Mountain Observatory. I would like to acknowledge Dr. Richard Honrath, who I did not have a chance to meet. His previous achievements are the solid basis of this dissertation. I would like to thank Dr. Claudio Mazzoleni and Dr. Lynn Mazzoleni for providing the opportunity to participate in the DOE and

NSF projects. I would like to thank Dr. Detlev Helmig (Institute of Arctic and Alpine Research), Dr. María Val Martín (University of Sheffield, U.K.), Dr. Paulo Fialho (Azores University, Portugal), and Mike Dziobak for their hard work in running the Observatory and providing me with observation data. I would also like to thank Dr. Swarup China and Dr. Katja Džepina (University of Rijeka) for involvement in their research.

I am grateful for the help and support I received from Dr. Mark Rowe, Aditya Kumar, Tanvir Khan, Ankita Mandelia and Emily Sokol. I would like to thank my wife and daughter, who gave me a lot of support during my study.

The projects in this dissertation are supported by Atmospheric Sciences Program of Michigan Technological University, U.S. NSF Award No. ATM-0720955 and AGS-1110059, and U.S. DOE Award No. DE-SC0006941.

Abstract

Long-range transport of continental pollution emissions has been found to affect air quality in the downwind regions. The Pico Mountain Observatory (PMO), which was established in 2001 in the Azores Islands, has been a perfect site to study long-range transport from North America to the central North Atlantic. The dissertation uses the observations and modeling products created since 2001 to provide insights on ozone production tendency during transport, trace gases observations for varying transport patterns, and aerosol ages in the free troposphere over the central North Atlantic.

The first phase of this dissertation research focused on determining the causes for the high $d[\text{O}_3]/d[\text{CO}]$ values (~ 1 ppbv/ppbv) observed in the summers of 2009 and 2010 at PMO. The folded retroplume technique, developed by Owen and Honrath (2009), was applied to combine upwind FLEXPART transport pathways with GEOS-Chem chemical fields. This technique was used to simulate ozone chemistry during the two selected transport events from North America. Ozone production was found at 2 km a.s.l. above the Azores area in the first event plume, apparently driven by PAN decomposition during subsidence of the air mass in the Azores-Bermuda High. In the second event, net ozone loss occurred during transport in the lower free troposphere, yet observed $d[\text{O}_3]/d[\text{CO}]$ was high. In both events, CO loss through oxidation

contributed significantly to $d[\text{O}_3]/d[\text{CO}]$ enhancement.

The second phase looked into chemical signatures in several transport pathways. The observations associated with different transport patterns were viewed as chemical signatures, which exhibit the consequences of photochemical reactions and physical processes during long-range transport. Enhancement of trace gases at PMO is driven by transport of pollution emissions. Ozone and nitrogen oxides enhancements were also found associated with subsidence of air masses from the upper troposphere and stratosphere. The $d[\text{O}_3]/d[\text{CO}]$ slope and non-methane hydrocarbon concentrations were also studied for the main transport patterns, which indicated that differently aged and polluted plumes intersect PMO as a result of a combination of photochemical oxidation and mixing with North Atlantic free tropospheric background air.

The third phase of this dissertation used radionuclide tracers associated with aerosol samples during summer 2013 at PMO to estimate age of aerosols collected over the central North Atlantic. Due to different rates of decay, the activity ratio of the atmospheric radionuclide tracers, ^{210}Po to ^{210}Pb , can be used to estimate age of the carrier aerosols. Analysis of 18 unbiased samples showed an estimated aerosol atmospheric residence time of 20.7 days at PMO. The long age of the aerosols was attributed to less efficient removal processes in the free troposphere compared to the boundary layer.

Chapter 1

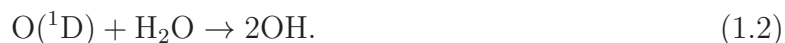
Introduction

1.1 Background

Air pollution not only affects regional air quality, but it can also be transported over thousands or tens of thousand kilometers from a source region, possibly causing air quality issues in remote marine regions and downwind continents. Intercontinental transport of air occurs within days to weeks (Stohl et al., 2002), and it has been found to carry considerable amounts of important air pollutants having atmospheric lifetime of days to downwind continents (Guerova et al., 2006). During transport, gaseous pollutants and aerosol particles undergo complicated chemical and physical processes that change the properties of air pollutants in numerous ways.

1.1.1 Tropospheric ozone

Ozone is a secondary air pollutant generated during photochemical reactions involving hydrocarbons and nitrogen oxides in the troposphere. It is the primary source of hydroxyl radicals (OH, shown in reactions 1.1 and 1.2):



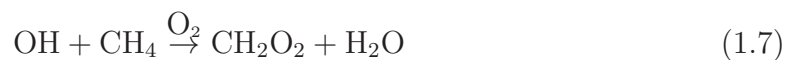
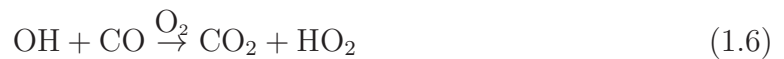
OH is the primary atmospheric oxidant and aerosol producer in the troposphere. Increased tropospheric ozone has also drawn particular concern due to the harm it causes to lives and its greenhouse effect. Tropospheric ozone is produced primarily through a chain of photochemical reactions involving airborne hydrocarbons and nitrogen oxides. Ozone is produced via reactions 1.3 and 1.4:



where M is an air molecule (N_2 and O_2). Once produced, ozone oxidizes NO back to NO_2 via reaction 1.5:



No additional ozone is produced after these reactions (Eq. 1.3 to 1.5). The set of reactions is recognized as the NO_x cycle. However, once emissions of carbon monoxide (CO), methane (CH_4) and hydrocarbons (RH) are provided, peroxy radicals ($PO_2 = CH_3O_2+RO_2+HO_2$) are generated through reactions:



In the NO_x cycle, peroxy radicals act as substitute oxidants of ozone and oxidize NO to NO_2 (reaction 1.9). When the NO_2 gets photolyzed, results in the production of new ozone (reactions 1.3 and 1.4).



Reaction 1.8 is usually faster than 1.6 and 1.7, so volatile organic hydrocarbons (VOC) are usually considered as the primary precursors of ozone. Thus ozone production requires NO_x ($\text{NO} + \text{NO}_2$) and VOC, all of which can limit ozone production in different scenarios. Ozone can be lost in the reactions:



Long-range transport is able to carry ozone and ozone precursors and lead to violations of regional air quality at downwind continents. Ozone has an atmospheric lifetime of a few days to weeks in the troposphere, which makes long-range transport of ozone possible. Production of ozone in remote regions of the troposphere is thought to be limited by available NO_x ($\text{NO} + \text{NO}_2$) in the atmosphere (Chameides et al., 1992). NO_x has a relatively short lifetime, less than 24 h (Liu et al., 1987), and can be quickly oxidized to nitric acid (HNO_3) and peroxyacetylnitrate (PAN). Removal of

NO_x and total reactive nitrogen (NO_y) is very sensitive to ambient conditions such as temperature and relative humidity (RH).

Ozone production tendency in North American outflows further downwind is not completely characterized, and variations in ozone and ozone precursors should be studied more carefully in different transport scenarios, such as differences in pollution sources and transport pathways in the atmosphere. For example, ozone production at remote sites was suggested by studies focusing on the North Atlantic regions (Honrath et al., 2004; Li et al., 2002b). During long-range transport, PAN is an important NO_x reservoir in the troposphere and has a life time of up to several months in the upper troposphere (Kleindienst, 1994), though it can quickly decompose in the marine boundary layer (Parrish et al., 1992). PAN decomposition has been found to be a potential NO_x source, that can lead to ozone production during the transport of pollution plumes (Kotchenruther et al., 2001; Zhang et al., 2008; Fischer et al., 2011). Meteorological conditions during pollution export and transport can also affect deposition of ozone precursors and ozone production tendency. The meteorological conditions at various altitudes vary, with the troposphere composed of the warm and humid air near the ground and cold and dry at higher altitudes. Thus, detailed meteorological conditions and transport pathways should be considered during studies of ozone production tendency.

1.1.2 Tropospheric aerosol age

Particulate species and aerosols are complex solid and liquid particles suspended in the atmosphere, originating from desert dust, volcanic aerosols, sea sprays and plant emissions. Atmospheric aerosol behaves differently from gaseous species. They affect the global radiation budget and climate directly or indirectly. By direct impact, aerosol particles absorb and scatter sunlight, and absorb infra-red radiation as well. Aerosol particles can also interact with cloud and atmospheric gas species, affecting climate indirectly. Compared to long-lived greenhouse gases in the atmosphere, the relatively shorter lifetime (days) of aerosol particles causes highly non-uniform distributions spatially and temporally. Aerosol particles also have immediate impacts on cloud condensation and increase the concentration of cloud droplets, which enhances short-wave albedo and the lifetime of clouds (Baker and Charlson, 1990). Thus, transport and transformation of aerosol particles are essential factors in determining regional air quality and climate. However, the radiative effects of aerosols have the largest uncertainties in global predictions to quantify present and future climate change (IPCC, 2014).

Aerosols participate in physical processes (e.g. coagulation, cloud nucleation and etc.) and atmospheric oxidation reactions. They are eventually removed from the atmosphere by dry deposition, wet deposition and gravitational settling. One of the

most widely applied dry deposition mechanisms in current atmospheric models was developed by Wesely (1989), in which the deposition resistance is parametrized based on various types of surfaces. Wet deposition is divided into wet scavenging in the cloud and washout in precipitation (Balkanski et al., 1998; Giorgi and Chameides, 1986; Hertel et al., 1995).

The determination of aerosol age in the atmosphere is critical to understand its role in air pollution transformation as well as climate change. Lifetimes of aerosols are estimated to range from a few days to a couple of weeks in the atmosphere (Cape et al., 2012; Ramanathan and Carmichael, 2008). Similarly wide ranges of aerosol lifetimes were found in global estimates in modeling studies (Stier et al., 2005). The source and age of aerosols need to be more carefully characterized to improve the theories that apply in weather forecasting and air quality prediction models.

Natural radionuclides have been used as tracers in studying aerosol sources and age (e.g., Gaffney et al., 2004; Hammer et al., 2007). ^{222}Rn ($t_{1/2} = 3.8$ days) is an inert gas species produced throughout the Earth's crust and emitted into the atmosphere (Kraemer, 1986). The first generation daughter product of ^{222}Rn , ^{218}Po attaches to fine aerosol particles within seconds. Due to different rates of decay, the activity ratio of the daughter radionuclides produced on the aerosols can be used to estimate atmospheric residence times of the carrier aerosols.

1.1.3 Modeling tools

Two types of atmospheric models were used to simulate the transport and chemistry of air pollutants and to understand trace gas observations.

Lagrangian particle dispersion models (LPDMs) are useful tools for estimating transport of air pollution in the atmosphere. LPDMs calculate advection and dispersion of air parcels in meteorological fields, such as wind, humidity and temperature. Forward simulations of LPDMs predict transport of emissions forward in time and the influence of the emissions in the downwind regions. For example, one of the popular LPDMs, FLEXPART, has been applied to evaluate the time scale of intercontinental transport and to predict impacts of air pollution at a downwind continent due to intercontinental transport (Stohl et al., 2002). In backward simulations, the transport of air parcels backward in time is calculated and estimates of the sources and transport pathways of air plumes observed at a downwind receptor are provided. The advantage of LPDMs over trajectory models is that the upwind residence time of air plumes can be used to calculate the contributions of air masses from different locations and sources by combining with emission inventories (Seibert and Frank, 2004). Because LPDMs usually have simplified chemical processes only, they are fast and efficient tools to assess sources and transport pathways.

Chemical transport models (CTMs) are usually Eulerian models that simulate reactions and transport of chemicals in the atmosphere. They are also driven by predicted meteorological fields, but with more features in simulating chemical and physical processes in the atmosphere. One CTM, GEOS-Chem, has fully coupled ozone-NO_x-VOC-aerosol chemistry, and can resolve more than 120 species with a Sparse Matrix Vector Gear code chemical solver (Jacobson and Turco, 1994). The GEOS-Chem model has been extensively evaluated and applied to a wide range of research topics related to atmospheric chemistry and air quality (e.g., Martin et al., 2002; Evans and Jacob, 2005; Duncan et al., 2007; Hudman et al., 2007; Wu et al., 2007; Huang et al., 2013). The performance of the model in simulating CO and ozone has been comprehensively evaluated (e.g., Bey et al., 2001; Wang et al., 2009; Kumar et al., 2013). GEOS-Chem has also been applied to simulate outflow events from North America (Liang et al., 1998; Li et al., 2004; Auvray and Bey, 2005; Hudman et al., 2009).

The two types of models can be combined together to study chemical transformation during long-range transport. FLEXPART backward simulation can be converted to a source-receptor relationship factor and folded with forward simulation (Owen and Honrath, 2009). For an upwind time of a backward simulation, a so-called folded retroplume is calculated by multiplying the factor with a quantity matrix (e.g., ozone field at upwind time t simulated by GEOS-Chem). The product represents the contribution of the selected quantity in the grid cell to the entire plume, and the summation of the product over the model domain (all grid cells) measures the total quantity in

the plume at the upwind time. In this way, we can calculate properties in the widely dispersed plume such as chemical mixing ratios, humidity, temperature, etc. Additional details on this method are provided in Chapter 2.

1.1.4 Previous research at PMO

In order to study long-range transport of air pollution in the free troposphere, the Pico Mountain Observatory (PMO) was established in 2001 on top of Pico Mountain (38.47°N, 28.40°W, 2,225 m a.s.l.) in the Azores Islands (Fig. 1.1). Although transport from all neighboring continents is possible, air quality at PMO is mostly impacted by air pollution emitted from North America due to predominantly westerly winds in mid-latitude regions of the Northern Hemisphere (Owen, 2003). Research has been conducted at PMO since 2001 (except 2007), and many important findings were published including elevation of ozone and ozone precursors (Honrath et al., 2004), transport schemes (Owen et al., 2006), anthropogenic and boreal fire impacts (Val Martín et al., 2006), seasonal cycles of hydrocarbons (Helmig et al., 2008), as well as aerosol properties (China et al., 2015). The collection of measurements at PMO and modeling studies are basis for the presented work.

Since PMO was established, trajectory models and transport simulations have been used to study pollution sources and transport characteristics, which has helped to

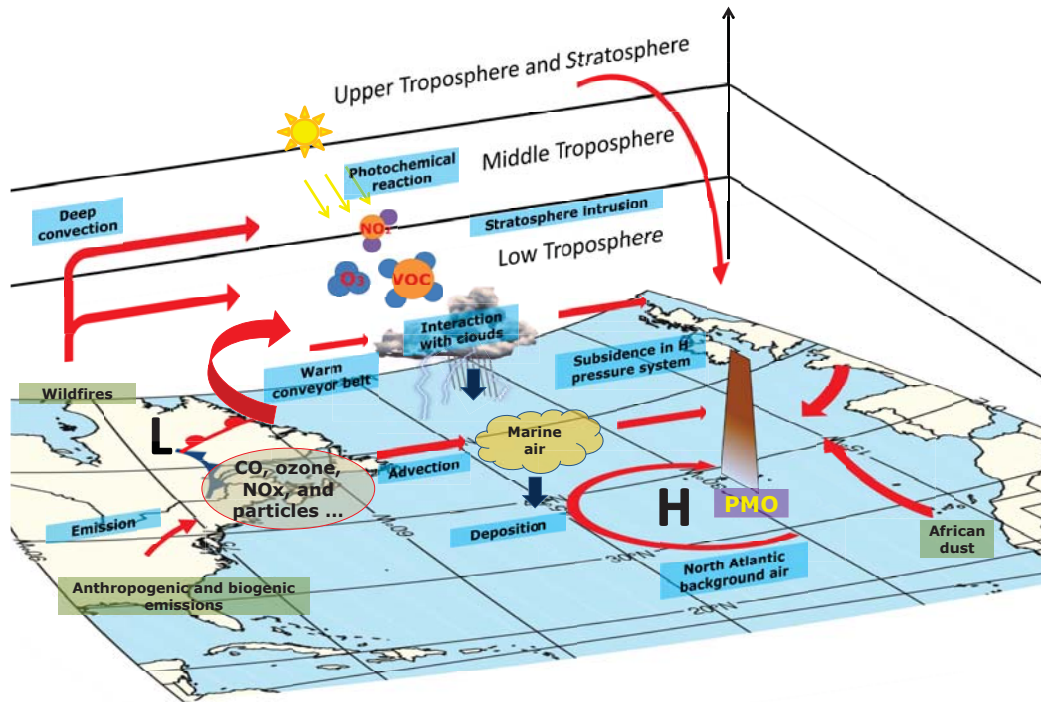


Figure 1.1: Long-range transport to the central North Atlantic with schematics of transport routes, potential sources and physical and chemical processes happening during transport.

understand observations of air pollutants at PMO. Transport to PMO was found to be dominated by westerly flows based on more than 40 years of backward trajectory analysis (Owen, 2003). About 33% of the trajectories originated from the North American continent compared to 35% from the North Atlantic and 31% from the Pacific. Although seasonal variation of these numbers was found, North America was found to be the dominant continental emission source transported to PMO.

The impacts of North American outflows on concentration of air pollutants have been confirmed and investigated in previous works. Elevated ozone and CO mixing ratios

have been found for periods affected by transport from North America (Honrath et al., 2004; Owen et al., 2006), including significant contribution from boreal forest fires (Val Martín et al., 2006; Lapina et al., 2006). Seasonal variations of CO and ozone were studied for specific years. During an intensive measurement campaign of nitrogen oxides from July 2002 to Aug 2005, a consistent correlation between long-range transport events and enhancement of nitrogen oxides was discovered, and higher mixing ratios of NO_y were observed during summertime (Val Martín et al., 2008b). Seasonal cycles of non-methane hydrocarbons (NMHC) transported to PMO and the aging rate of transported plumes were studied by Helmig et al. (2008). Lower concentrations of NMHC were found during summer, which was attributed to more efficient photochemical oxidation. In a sister study, NMHC ratios, also referred to as photochemical clocks, were used to understand ozone observations (Honrath et al., 2008). In spite of the number of studies, ozone production mechanisms and long-term observations of chemical species are not fully understood and require further study.

1.2 Research objectives

The objective of this research are to:

A. Determine ozone production tendency and transformation of ozone precursors in pollution plumes in North American outflows.

In order to understand ozone production tendency and transformation of ozone precursors in plumes exported from North America, measurements of CO, ozone, NO_{xy}, and NMHC data measured in summers 2009–10 were used to identify pollution plumes exported from North America and to examine ozone enhancement at Pico. In addition to anthropogenic and wildfire emissions, other sources of ozone including stratospheric intrusion and lightning were considered. Impacts of weather conditions on transport were investigated.

B. Determine characteristics of transport to PMO and relationships between transport patterns and observations of air pollutants at PMO.

In order to understand observations of air pollutants conducted at PMO during the past twelve years, the trace gas mixing ratios were determined for several different transport patterns. Due to the distinct geographic locations of source regions and associated atmospheric circulation, transport periods and patterns vary for different sources, seasons, and climate. For spring, summer and fall seasons 2001–10, long-term variability in air composition at PMO were studied. Potential impact factors such as types of sources, transport heights, and meteorology conditions were investigated.

C. Estimate aerosol atmospheric residence time using observations of atmospheric radionuclides.

In order to estimate aerosol atmospheric residence time at PMO, the ²¹⁰Po activity collected on filter samples was measured using Alpha spectrometry. The results were

analysed together with aerosol concentrations, FLEXPART transport simulations, and black carbon absorption. Potential sources of ^{210}Po were studied. Based on uncertainty analysis, use of atmospheric radionuclides to estimate aerosol residence time was validated. The estimated residence time range was also compared to the other studies that employed the same radionuclide approach.

1.3 Dissertation overview

This dissertation consisted of three projects. In Chapter 2, a Lagrangian particle dispersion model (FLEXPART) and an Eulerian chemical transport model (GEOS-Chem) are combined to provide a semi-Lagrangian view of chemical transformation in long-range transport plumes. This study focused on observations of trace gas concentration collected at PMO in 2009-10. In Chapter 3, based on more than ten years of observation and an archive of backward transport simulations applied to PMO, a chemical climatology is presented that provides a comprehensive understanding of the diverse observations of trace gaseous species concentrations at PMO. Environmental factors that could potentially affect chemical transformation were considered to categorize the most common transport patterns having specific chemical signatures. In Chapter 4, radionuclide activities of aerosol samples collected at PMO were reported and used to estimate aerosol atmospheric residence time in the free troposphere. The residence time of aerosols at PMO was discussed and compared with other studies.

Chapter 2

A Semi-Lagrangian view of ozone production tendency in North American outflow¹

¹This chapter is based on Zhang et al., A semi-Lagrangian view of ozone production tendency in North American outflow in the summers of 2009 and 2010. *Atmospheric Chemistry and Physics*, 14(5), (2014): 2267-2287. Copyright permission details given in Appendix C.

2.1 Introduction

Ozone plays key roles in tropospheric chemistry and air quality. Photolysis of ozone is a primary source of hydroxyl radical, the primary oxidant in the atmosphere (Logan et al., 1981a; Thompson, 1992). Anthropogenic activities such as fossil-fuel combustion produce large amounts of ozone precursors (CO, hydrocarbons, and nitrogen oxides) (Mahlman et al., 1980). The photochemical lifetime of ozone in the troposphere ranges from days to weeks (Wang et al., 1998a), while intercontinental transport of air pollution can occur in 4–10 days (Stohl et al., 2002). Intercontinental transport has been found to carry considerable amounts of ozone to downwind continents (e.g., Guerova et al., 2006). Ozone production tendency during transport is controlled by the availability of ozone precursors, with net ozone production having been observed in pollution originating in East Asia (Kotchenruther et al., 2001) and North America (e.g., Reeves et al., 2002; Auvray et al., 2007; Hudman et al., 2009).

Production of ozone in remote regions of the troposphere is thought to be limited by available NO_x ($\text{NO} + \text{NO}_2$) in the atmosphere (Chameides et al., 1992). NO_x has a relatively short lifetime, less than 24 h (Liu et al., 1987), and can be quickly oxidized to nitric acid (HNO_3) and peroxyacetylnitrate (PAN). Removal of NO_x and total reactive nitrogen (NO_y) is very sensitive to ambient conditions such as temperature and relative humidity (RH). PAN is an important NO_x reservoir in the troposphere

and has a life time of up to several months in the upper troposphere (Kleindienst, 1994), though it can quickly decompose in the marine boundary layer (MBL; lifetime < 2.5 days (Parrish et al., 1992)). PAN decomposition has been found to be a potential NO_x source, which can lead to ozone production during the transport of pollution plumes (Kotchenruther et al., 2001; Zhang et al., 2008; Fischer et al., 2011)

Meteorological conditions during pollution export and transport are thought to be critical to the deposition of ozone precursors and ozone production tendency. Air masses can be exported from the continental boundary layer (CBL) by lifting into the free troposphere (FT, 3–4 km a.s.l.), where air masses are transported by strong geostrophic winds. Export of air pollution from populated areas can also occur close to the boundary layer ($< 2\text{--}3$ km a.s.l.; e.g., Neuman et al., 2006). The meteorological conditions at various altitudes vary, with the troposphere composed of the warm and humid air near the ground and cold and dry at higher altitudes. Thus, detailed meteorological conditions and transport pathways should be considered during studies of ozone production tendency.

Ozone and ozone precursors exported from the North American boundary layer, especially from the populated Eastern coastal region, are known to impact air quality over the North Atlantic (Parrish et al., 1993) and even over Europe (Auvray and Bey, 2005). Findings from the North Atlantic Regional Experiment (NARE), a multi-year

campaign that began in 1993, suggested anthropogenic emissions contribute significant amounts to the ozone budget in the North Atlantic region (Fehsenfeld et al., 1996). More recently, the International Consortium for Atmospheric Research on Transport and Transformation (ICARTT, Fehsenfeld et al., 2006) study, conducted during July–August 2004, revealed observations indicating high ozone levels (up to 100 ppbv) in North American outflows (Mao et al., 2006). In other measurement periods, only slightly elevated ozone (> 55 ppbv) was observed in the free troposphere near the US East Coast by using retrievals from the Tropospheric Emission Spectrometer (TES; Hegarty et al., 2009). Despite this body of research, ozone production tendency in North American outflow further downwind is incompletely characterized.

In order to study the photochemical evolution of pollutants in the continental outflows from North America, an observatory was established in July 2001 on top of Pico Mountain in the Azores Islands (38.47° N, 28.40° W, 2225 m a.s.l.) which enabled frequent sampling of North American outflows following the prevailing westerly winds at mid-latitudes. Measurements of ozone and CO at the Pico Mountain Observatory (PMO) demonstrated an influence of long-range transported pollution (Honrath et al., 2004). Periods of elevated ozone were linked to anthropogenic emissions (Owen et al., 2006) and boreal forest fires (Lapina et al., 2006), both of which contribute to enhancement in nitrogen oxides in the central North Atlantic (Val Martín et al., 2008b). In this study, we conduct a semi-Lagrangian analysis (Owen and Honrath,

2009) to investigate transformations of chemical species and the associated meteorological conditions during transport. As the first application of this method, we focus on anthropogenic pollution events with relatively simple transport patterns. We present detailed analysis of the chemical evolution of two pollution plumes transported from North America to PMO in summers 2009 and 2010. The analysis enables us to evaluate the validity of the assumption that $d[\text{O}_3]/d[\text{CO}]$ indicates net ozone production/loss during transport.

2.2 Methods

2.2.1 Pico Mountain Observatory and measurements

Summertime measurements of CO, O₃, NO_x, NO_y, non-methane hydrocarbons (NMHC), RH, and black carbon were collected in 2009 and 2010 at Pico Mountain Observatory. The Observatory locates at an altitude of 2225 m a.s.l., which prevents it from being influenced by local upslope flow for over 80% of the time in summer (Kleissl et al., 2007), providing a unique land-based location for the observation of free tropospheric air in the North Atlantic. CO levels were measured using a modified commercial instrument (Thermo Environmental, Inc., Model 48C-TL). Its sensitivity was calibrated daily with a standard gas that was referenced against the calibration

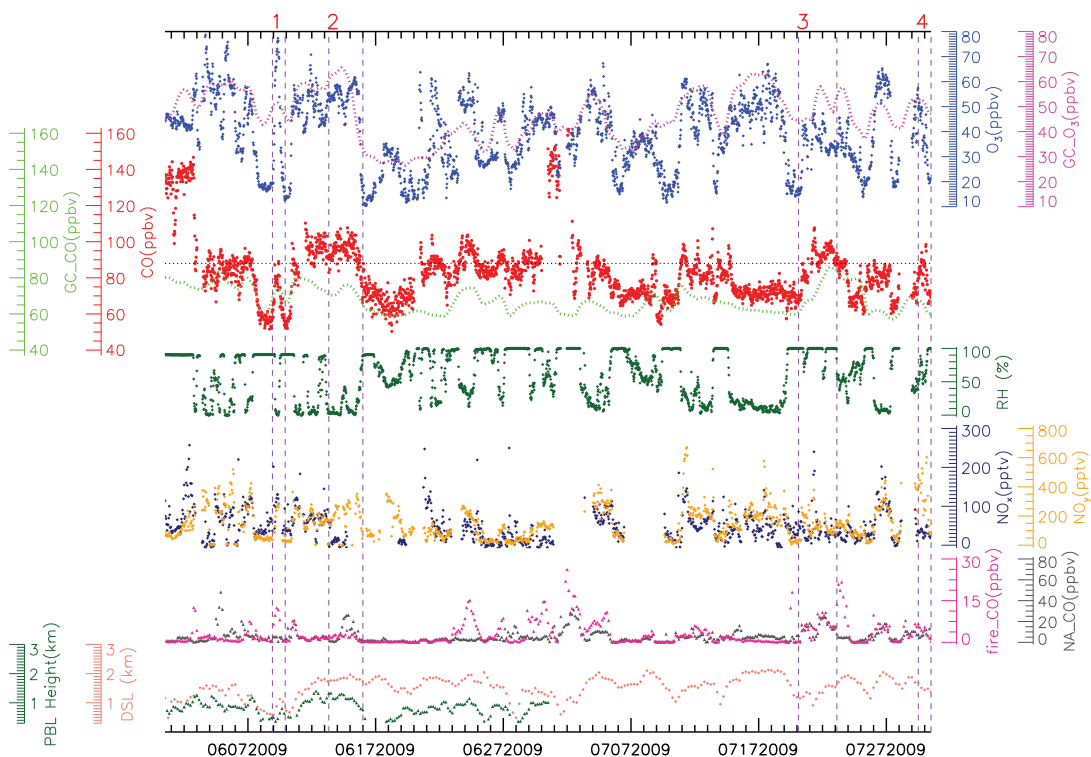


Figure 2.1: Time series of 30 min average of measurements and meteorological conditions, 6 h average contributions from North American anthropogenic emission (NA CO) and biomass burning emissions (FIRE CO) calculated by FLEXPART, and 4 h average GEOS-Chem CO (GC CO) and O₃ (GC O₃) at Pico Mountain Observatory station during summer 2009. Data points are colored with corresponding y-axes. Vertical dashed lines show time windows of each event, which are labeled with red numbers close at the top.

scale of the Global Monitoring Division, NOAA, Boulder, CO. Ozone was measured with two commercial ultraviolet absorption instruments (Thermo Environmental Instruments Inc., Model 49C). Honrath et al. (2004) presented details on these methods for CO and ozone measurement. NO, NO₂ and NO_y were measured using an automated system that was custom-developed at Michigan Technological University. NO

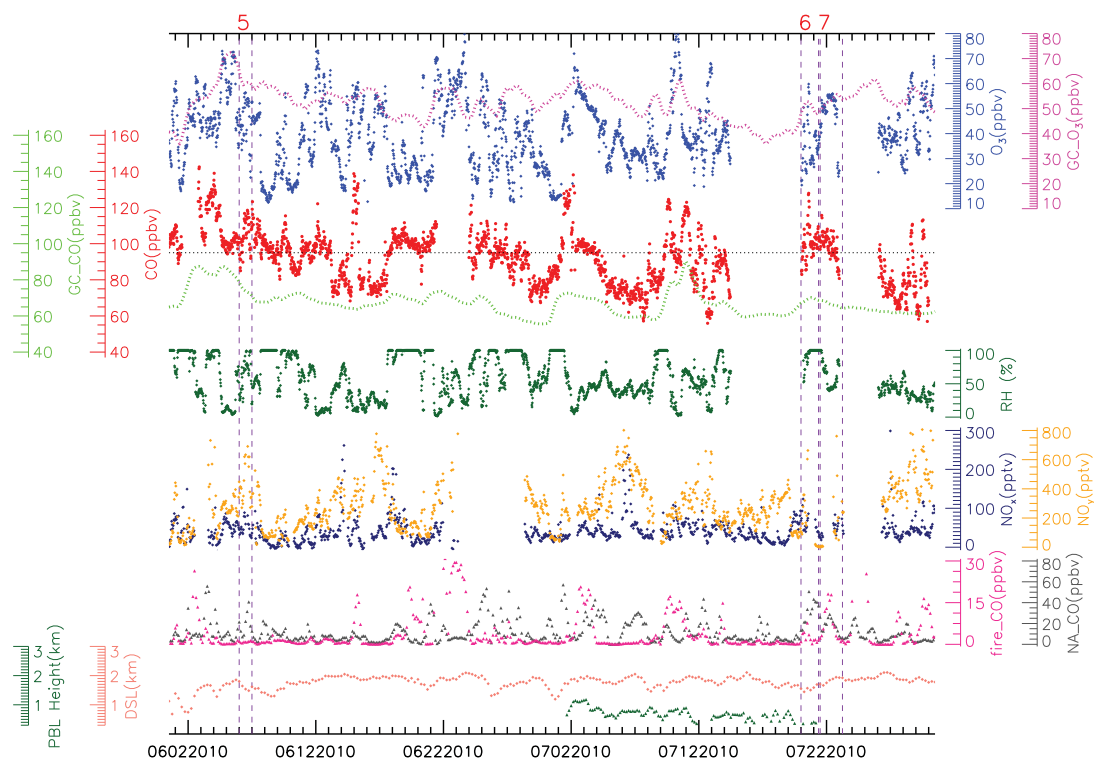


Figure 2.2: Same as Fig. 2.1 but for summer 2010.

was detected by O₃ chemiluminescence, NO₂ by conversion to NO via ultraviolet photo dissociation, and NO_y by Au-catalyzed reduction to NO in the presence of CO (Val Martín et al., 2006). In this work, we present 30 min averaged measurement data of summers 2009 and 2010 for all species in Figs. 2.1 and 2.2.

2.2.2 Application of FLEXPART

The Lagrangian particle dispersion model (LPDM) FLEXPART (version 8.2; Stohl et al., 1998) was used to simulate transport of North American outflows. Both forward and backward modes were implemented to simulate North American outflows and transport trajectories. CO from the Emissions Database for Global Atmospheric Research (EDGAR version 3.2; (Olivier and Berdowski, 2001)) annually averaged anthropogenic emissions and the Global Fire Emissions Database (GFED v3.1, daily averaged fire emissions; Mu et al., 2011) were used in FLEXPART runs. A combination of 6 h meteorological Final Analysis (FNL) data at 00:00, 06:00, 12:00, and 18:00 UTC, and 6 h Global Forecast System (GFS) data at 03:00, 09:00, 15:00, and 21:00 UTC, was used to drive FLEXPART. The dataset had a 3-hourly temporal resolution, with 1 horizontal resolution and 26 vertical levels.

When simulations were conducted in the backward mode, a passive tracer was released from the receptor and advected and dispersed backwards in time, resulting in spatial distribution of the air mass at an upwind time, referred to as a “retroplume”. The retroplumes can be used to calculate a time series of tracer concentrations at the receptor contributed by a certain emission source (e.g., anthropogenic or biomass burning) by multiplying the residence time in the lowest 300 m with the emission inventory (Seibert and Frank, 2004). In this study, backward simulations were set in

two different spatial resolutions. For the purpose of identification of North American transport events, retroplumes were released every 3 h, with 4000 particles released over a one-hour time interval from a $1^\circ \times 1^\circ$ horizontal grid box of altitude from 2000 m a.s.l. to 2500 m a.s.l. centered at PMO. The retroplume output was saved in a grid having a $1^\circ \times 1^\circ$ horizontal resolution in eleven vertical levels from 300 m to 15 000 m a.s.l. A high-resolution retroplume simulation, in which 10 000 particles were released every 3 h, was conducted for higher accuracy in the folded GEOS-Chem and FLEXPART technique (see below). FLEXPART output in this high resolution run was saved in a grid having a 2° (latitude) \times 2.5° (longitude) horizontal resolution in 130 vertical levels from 0 m to 8 km a.s.l.

Forward simulations injected anthropogenic CO emissions into the lowest 300 m over North America. Two forward simulations were conducted, one with EDGAR anthropogenic CO emissions in an output grid matching the retroplume grid used as a component of folded FLEXPART retroplume analysis (see Sect. 2.2.4), and one with emissions from the same inventory used in GEOS-Chem simulations and with the same grid, used to evaluate discrepancies in transport between FLEXPART and GEOS-Chem (see Sect. 2.3.3).

2.2.3 Application of GEOS-Chem

GEOS-Chem is a global three-dimensional model of tropospheric chemistry driven by assimilated meteorological observation fields from the Goddard Earth Observing System (GEOS) of the NASA Global Modeling Assimilation Office (Bey et al., 2001). The model has fully coupled ozone-NO_x-VOC-aerosol chemistry, and can resolve more than 120 species with a Sparse Matrix Vector Gear code chemical solver (Jacobson and Turco, 1994). Anthropogenic emissions in GEOS-Chem follow the EDGAR global inventory (Olivier and Berdowski, 2001) and are updated with regional inventories including the US Environmental Protection Agency National Emissions Inventory (EPA/NEI05 and EPA/NEI99), the Canada Criteria Air Contaminants Inventory, the European Monitoring and Evaluation Program inventory, and the STREETS Emission Inventory in Asia (Streets et al., 2003). The GEOS-Chem model has been extensively evaluated and applied to a wide range of research topics related to atmospheric chemistry and air quality (e.g., Martin et al., 2002; Evans and Jacob, 2005; Duncan et al., 2007; Hudman et al., 2007; Wu et al., 2007; Huang et al., 2013).

The performance of the model in simulating CO and ozone has been comprehensively evaluated (e.g., Bey et al., 2001; Wang et al., 2009; Kumar et al., 2013). Simulation of CO was found to be significantly affected by emission inventories used, but model results generally show reasonable agreement with data from various observational

sites or networks around the world (Duncan et al., 2007). GEOS-Chem has also been applied to simulate outflow events from North America (Liang et al., 1998; Li et al., 2004; Auvray and Bey, 2005; Hudman et al., 2009). Li et al. (2005) used GEOS-Chem to characterize the major outflow pathways from North America to the North Atlantic and the model successfully captured ozone chemistry during convective lifting of pollution plumes. In the work by Millet et al. (2006), GEOS-Chem was used to estimate CO in outflows from the US to Chebogue Point.

This study used GEOS-Chem v9-01-02 driven by GEOS-5 meteorology with a horizontal resolution of $2^\circ \times 2.5^\circ$ and 47 vertical layers. Model simulations for the period of January–July for both 2009 and 2010 are conducted and the results for June 2009 and July 2010 are used in the final analysis. The time steps used for emissions (30 min), chemistry (30 min), transport (15 min) and convection (15 min) are typical of a $2^\circ \times 2.5^\circ$ simulation. A domain extending from 100° to 20° W (longitude) and 24° to 56° N (latitude) was selected, which includes part of North America and the PMO. Instantaneous mixing ratios of relevant tracers (e.g., CO, O₃, nitrogen-containing species such as NO_x and PAN, and NMHC such as ethane, propane and propene) with 2 h resolution and diagnostics for meteorology including RH, temperature, and boundary layer height were archived for this domain. In addition, the daily average production/loss rates of O₃ for June 2009 and July 2010 were saved. These GEOS-Chem simulations are a subset of those used in Kumar et al. (2013), in which the observed CO and ozone trends at PMO were compared with both GEOS-Chem

simulations and satellite data from the Atmospheric Infrared Sounder (AIRS) and TES. They found that GEOS-Chem underestimated CO over the North Atlantic, but successfully captured the seasonal cycles and decreasing trends of CO and ozone at PMO.

A tagged CO simulation in GEOS-Chem was also employed in order to study the transport of CO from the US to PMO. A description of this simulation can be found in Duncan et al. (2007). Two-hourly instantaneous tracer mixing ratios for June 2009 and July 2010 were archived for the above domain.

2.2.4 Folded GEOS-Chem and FLEXPART technique

A LPDM retroplume simulates the displacement and deformation of an air mass in the atmosphere. However, LPDMs typically use an Eulerian grid for saving results, and are thus unable to fully describe source-to-receptor transport. To address this issue, Owen and Honrath (2009) derived a method to track pollution plumes by computing the entry-wise product (also known as Hadamard product R.Johnson (1989)) of the output from the forward and backward simulation, a process that has been described as “folding” the two data fields. The output of this method, which we call a folded retroplume, highlights a transport pathway by overlapping forward simulation, initialized at the source, with backward simulation released from the receptor.

As a result, a folded retroplume exhibits a 4-D (spatial and temporal) field that contains the polluted air plume and in which most of the physical and chemical processing occurs.

To meet differing objectives, retroplumes can be folded with FLEXPART or GEOS-Chem simulations. FLEXPART retroplumes represent a sensitivity, $S_{(j,t,(j',t'))}$, of the air mass in an upwind cell (j) at an earlier time (t) to that of the entire plume released at the receptor (j') at time t' . A collection of these sensitivities $S_{(t,(j',t'))}$ is a 3-D matrix that can be used to estimate the sensitivity of emissions and meteorological conditions from the upwind distribution of the air mass. For time t , the folded retroplume is obtained by multiplying the sensitivity matrix $S_{(t,(j',t'))}$ with a quantity matrix χ_t . In this study, FLEXPART retroplumes were folded with mixing ratios (χ_t) from FLEXPART forward simulations to produce FLEXPART folded retroplumes (hereafter called “folded retroplumes”). FLEXPART retroplumes were also folded with mixing ratios, ozone reaction rates and meteorological fields from GEOS-Chem results (hereafter called “folded results”). The former simulate transport pathways while the latter, as described below, simulate chemical transformation during transport.

The formulation of the folded results can be summarized as follows by using a tracer mixing ratio as an example of the quantity matrix χ_t . The retroplume is folded with the GEOS-Chem mixing ratio matrix field $\chi_{(j,t)}$ of a given species at a specified upwind

time. The product, called the partial folded quantity ($\text{PFQ}_{(j,t,(j',t'))}$) and calculated in Eq. (2.1), represents the contribution from the grid cell (j) to the mixing ratio of the species in the plume, whereas the distribution of the $\text{PFQ}_{(j,t,(j',t'))}$ at time t represents the spatial distribution of contributions from all grid cells in the model domain.

$$\text{PFQ}_{j,t,(j',t')} = S_{j,t,(j',t')} \cdot \chi_{j,t,(j',t')} \quad (2.1)$$

A summation of the PFQs over the model domain (j) at an upwind time (t) measures the mixing ratio of target tracer substance in the entire dispersed plume (Eq. 2.2), called the upwind folded quantity (UFQ):

$$\text{UFQ}_{t,(j',t')} = \sum_j \text{PFQ}_{j,t,(j',t')} \quad (2.2)$$

Variation in UFQ in the target plume changes according to chemical and physical processes simulated by GEOS-Chem. Therefore, chemical transformation in the plume can be simulated by a time series of UFQs and provides a semi-Lagrangian view of plume aging during the transport. This semi-Lagrangian approach uses backward FLEXPART simulation results to sample air masses in an Eulerian GEOS-Chem field. There are three features of this method that prevent it from providing a perfect Lagrangian view. The fundamental aspect is the difference in meteorology fields driving the two models. GEOS-Chem uses the GEOS meteorology fields while FLEXPART is

driven by GFS fields. Although both GEOS and GFS are considered to be valid simulations of meteorology, some degree of discrepancy is expected between them. The second feature is the result of random components in the models, including turbulence and convection mechanics, which were noted when the method was first published (Owen and Honrath, 2009). Finally, inherent numerical diffusion in GEOS-Chem can lead to extra dilution of pollution plumes. This last issue can be reduced by using higher resolution simulations but cannot be entirely avoided. Given the large scale of the particular events that met our criteria (10° lat x 10° lon), the folded results are still able to adequately reflect a Lagrangian view of chemical processing. However, some chemical species in the plume may deviate from mass conservation and the magnitude of deviation may vary for differing conditions, e.g., transport types or properties of species. In regards to the affected results, specific issues are discussed as they arise. In this study, UFQs of mixing ratios such as those of ozone and ozone precursors are of primary interest. UFQs of meteorological conditions such as temperature and RH are also calculated for better characterization of simulated processes.

2.3 Characteristics of North American transport events during summers 2009 and 2010

In this section we describe several criteria that were used to identify the transport events from North America to PMO during the summers of 2009 and 2010. The objective is to identify transport events predominantly affected by emission sources over the North American continent that exhibit direct and rapid transport from source to PMO with no interference from local sources due to mechanically forced upslope flow. We present measurement and modeling results for the time periods in which transport events occurred, and select events that met the criteria. Table 2.1 summarizes a list of qualified events that are impacted by biomass burning emission, anthropogenic emission or both.

2.3.1 Criteria applied for transport event identification

2.3.1.1 Elevated CO

CO is a pollutant that is emitted during incomplete combustion from both anthropogenic and biomass burning sources. Due to its low reactivity in the troposphere

(lifetime from weeks to months), CO has been used widely as a tracer of pollution (Fishman and Seiler, 1983). Periods with an observed CO mixing ratio above 88 ppbv for 2009 and 95 ppbv for 2010 (horizontal dashed lines in CO panels in Figs. 2.1 and 2.2), respectively, were considered to be potential transport events. These cutoff values were defined to be 20 ppbv over the summertime background in each respective year, based on the approach used by Honrath et al. (2004). There were periods of several days (e.g., from 11 to 17 June 2009) as well as short time windows of several hours (e.g., on 9 June 2009) during which measured CO exceeded the cutoff value. All periods identified by this criterion were evaluated against additional criteria that are discussed in detail in Sect. 2.3.2. While CO levels exceeding the cutoff are the primary indicator of the start and end of each event, neighboring time periods having lower CO levels are combined into events based on the assumption that the edge of event plumes contained lower concentration of pollutants due to dilution by background air.

Table 2.1
Summary of analysis used to identify events resulting from anthropogenic outflows from North America.

Event	Period ^a	$d[\text{O}_3]/d[\text{CO}]$	N^b	Avg-CO (ppbv)	$d[\text{O}_3]/d[\text{CO}]$ (GC) ^c	GC-CO ^d	BB ^e	Anth ^f	Origin in US ^g
1	09/06/2009 10–	2.28 ($R^2 = 0.838$)	48	69.2	0.82 ($R^2 = 0.840$)	yes	yes	no	E. Coast
2	10/06/2009 10	1.37 ($R^2 = 0.519$)	126	93.9	3.54 ($R^2 = 0.436$)	yes	no	yes	E. Coast
3	13/06/2009 20–	0.85 ($R^2 = 0.431$)	131	89.0	0.58 ($R^2 = 0.395$)	yes	yes	yes	SE. Coast
4	16/06/2009 12	1.29 ($R^2 = 0.607$)	48	80.5	0.78 ($R^2 = 0.948$)	yes	yes	yes	SE. Coast
5	20/07/2009 15–	0.96 ($R^2 = 0.348$)	48	104.1	0.78 ($R^2 = 0.732$)	yes	no	yes	Florida
6	23/07/2009 15	0.99 ($R^2 = 0.744$)	64	100.8	1.92 ($R^2 = 0.139$)	yes	no	yes	SE. Coast
7	30/07/2009 00–	1.29 ($R^2 = 0.379$)	72	98.6	-1.4 ($R^2 = 0.790$)	yes	yes	yes	E. Coast
	31/07/2009 00								
	06/06/2010 12–								
	07/06/2010 12								
	20/07/2010 12–								
	21/07/2010 21								
	22/07/2010 00–								
	23/07/2010 18								

^a UTC time in DD/MM/YYYY HH, determined by using ozone and CO measurements as described in text

^b number of data collected for each event

^c $d[\text{O}_3]/d[\text{CO}]$ simulated by GEOS-Chem at PMO for event period

^d CO elevation for event period in GEOS-Chem simulations

^e significant impact from biomass burning emission

^f significant impact from North American anthropogenic emission

^g determined by FLEXPART folded retroplumes

2.3.1.2 $d[\text{O}_3]/d[\text{CO}]$

The change in O_3 relative to CO , or $d[\text{O}_3]/d[\text{CO}]$, has been widely used as a measure of ozone enhancement (e.g., Parrish et al., 1993). The $d[\text{O}_3]/d[\text{CO}]$ values cited from other studies and reported in our work are calculated by two-sided regression, which accounts for error in both variables in the regression (Ayers, 2001). Significant correlation between CO and ozone was found over eastern North America. A $d[\text{O}_3]/d[\text{CO}]$ of 0.3 was speculated to represent a uniform characteristic of boundary layer air over eastern North America in summertime (Chin et al., 1994; Cooper et al., 2001a). Various values of this ratio from satellite observation and aircraft campaigns have been reported downwind of North American emission regions. At Nova Scotia, Berkowitz et al. (1996) observed transported pollution plumes that originated from urban areas of North America and $d[\text{O}_3]/d[\text{CO}]$ ranged from 0.19 – 0.30 ($R^2 > 0.5$). During the 1993 summer NARE intensive, a range in $d[\text{O}_3]/d[\text{CO}]$ from 0.25 to 0.28 was observed over eastern North America and the North Atlantic (Parrish et al., 1993; Daum et al., 1996; Fehsenfeld et al., 1996). In a spring study, Prados et al. (1999) reported a $d[\text{O}_3]/d[\text{CO}]$ of 0.21 ($R^2 = 0.19$) during intensive aircraft measurements between the US and Bermuda. Zhang et al. (2006) provided a global distribution of the O_3 - CO correlation in the middle troposphere (618 hPa) for July 2005 from both TES detection and GEOS-Chem simulation. They found a $d[\text{O}_3]/d[\text{CO}]$ value of 0.81 mol/mol ($R^2 = 0.28$) over the Eastern US. The value was shown to be consistent

with an observation of $d[\text{O}_3]/d[\text{CO}] = 0.90$ mol/mol , $R^2 = 0.12$, at 600–650 hPa from the ICARTT aircraft campaign. Hegarty et al. (2009), also using TES data, reported a much smaller springtime $d[\text{O}_3]/d[\text{CO}]$ of 0.13 ($R^2 = 0.048$) extending from North America out over the Atlantic Ocean for 2005 and 2006. Values of $d[\text{O}_3]/d[\text{CO}]$ that have been reported in literature vary from 0.1 to 1, and in most cases, R^2 -values are less than 0.5. The cause of the variation in slope and low correlation may be mixing of differently aged air masses from different sources. Different ozone production tendency during transport can lead to differing values of $d[\text{O}_3]/d[\text{CO}]$ observed at differing times in the same location. Events that qualify for the study presented here were selected based on the condition to have statistically significant correlation between simultaneously observed CO and ozone at the 95% confidence level. Values of $d[\text{O}_3]/d[\text{CO}]$ and R^2 for time periods that met the first criterion (CO mixing ratio > cutoff) and this criterion are included in Table 2.1.

2.3.1.3 Transport pathway

Simulated transport pathways of pollution plumes were obtained from FLEXPART folded retroplumes, computed as summarized in Sect. 2.2.4 in which CO was used as a tracer for anthropogenic pollution. For a given event, PFQs of CO were calculated by folding 3-D CO fields from forward simulation with the 3-D residence time matrix from backward simulation such that the folded retroplume (distribution of PFQs)

highlighted the transport pathway. We selected transport events characterized by an anthropogenic emission originating in the eastern US and direct transport pathway to the PMO by examining the FLEXPART folded retroplumes. Transport events with complex pathways are difficult to assess due to complicated chemistry and increased dilution. Therefore, we did not include events with transport pathways exhibiting multiple branches or long looping times (i.e., more than a week) over the North Atlantic Ocean to further evaluation in this study.

2.3.1.4 Anthropogenic versus fire emission impacts

In order to focus on anthropogenic events, we distinguished events according to source type. Contributions from anthropogenic and wildfire emissions were calculated by folding FLEXPART retroplumes with separate emission inventory categories as described in Sect. 2.2.2. Three-hour averages of CO contributions from each source are presented in Figs. 2.1 and 2.2. Events that received more than 10% of the observed CO mixing ratio at PMO from North American anthropogenic or biomass burning emissions were identified as impacted by the respective emission source and displayed with a “yes” flag in Table 2.1.

2.3.1.5 Upslope flow

Local boundary layer air masses can be carried by upslope flow to PMO and lead to mixing of free tropospheric air with MBL air. Upslope flow occurs through mechanically-forced lifting, in which strong synoptic winds are reflected by the mountain slope, or through buoyant forcing, in which the surface air mass is lifted as a result of solar heating. Kleissl et al. (2007) determined the occurrence of upslope flow to be less than 39% of the days during summers 2004 and 2005. During the days when upslope flow occurred, there was no evidence of significant impacts of uplift on measurement of chemicals interested in this study. For summers of 2009 and 2010, we examined the possibility of upslope flow due to mechanical lifting.

When mechanically-forced lifting occurs, air masses above the dividing streamline (DSL) can be lifted to the top of the mountain, while air masses below the DSL travel around the mountain. The altitude of the DSL (in the bottom panel in Figs. 2.1 and 2.2) is calculated by using the method described by Sheppard (1956) from the wind speed profiles in the meteorological dataset driving FLEXPART (GFS and FNL). During time periods when the height of the DSL was less than the MBL height simulated in GEOS-Chem, PMO may have received MBL air. As shown in Figs. 2.1 and 2.2, there were a few time periods when the calculated DSL was below the MBL. These time periods were excluded from event selection.

2.3.1.6 Capture of events in GEOS-Chem

A requirement for valid folding results from the two models is that the events are predicted to occur in both FLEXPART and GEOS-Chem as indicated by enhanced CO levels at PMO in both simulations. CO and ozone data, shown in Figs. 2.1 and 2.2, were obtained from a $4^\circ \times 5^\circ$ GEOS-Chem simulation in the work of Weise (2011). Four-hour averaged mixing ratios were extracted from the grid cell that was centered at PMO. For all events identified using the other criteria summarized in Table 2.1, GEOS-Chem indicated elevated CO mixing ratio, demonstrating that events identified through measurements at PMO were also captured in GEOS-Chem.

2.3.2 Characteristics of transport plumes and quantified events

The transport conditions that qualified as events as summarized in Table 2.1 exhibit a wide variety of characteristics. A range in $d[\text{O}_3]/d[\text{CO}]$ values (from 0.85 to 2.28) was found for the eight events. Our criteria selected events with significant impacts from anthropogenic or biomass burning emissions. In this study, we looked for events in which $d[\text{O}_3]/d[\text{CO}]$ was close to or greater than 1, a value found previously at PMO in North American outflows (Honrath et al., 2004). The correlation coefficients

reported in Table 2.1 are greater than those reported in the previous studies discussed in Sect. 2.3.1.2, and similar to the values for events in the previous study by Honrath et al. (2004). Higher correlation coefficient values are observed at PMO because the measurement data used in the regressions were extracted for an individual transport event as identified based on the above criteria.

Figures 2.1 and 2.2 show time series measurement data at PMO and model results of CO contributions from North American anthropogenic and biomass burning emissions in summers 2009 and 2010, respectively. We found several events linked to anthropogenic and biomass burning emissions. For instance, plumes for Events 2 and 6 were dominated by North American anthropogenic emissions, as indicated by FLEXPART North American CO (NA-CO) contributions of 35 and 42 ppbv (Figs. 2.1 and 2.2), respectively. Conversely, Event 1 was characterized by fire emission influence, as indicated by the FLEXPART biomass burning CO (FIRE-CO) contribution up to 15 ppbv (Fig. 2.1). There were also periods when both types of emissions contributed significant amounts of CO (e.g., Events 4 and 7). Overall, the frequency and magnitude of contribution from North American anthropogenic emissions was estimated to be greater than those of biomass burning emissions during the summers of 2009 and 2010. In this study, we examined Events 2 and 6 in detail as they meet the criteria described in Sect. 2.3.1.

2.3.3 Simulation of transport for selected events

Prior to detailed analysis of chemical and physical processes for Events 2 and 6, we discuss transport pathways and evaluate the similarity of transport simulation in FLEXPART and GEOS-Chem. The transport characteristics of the two events are discussed in Sect. 2.3.3.1. As a prerequisite for folding calculation, transport similarity in the two models is evaluated in two approaches. Tagged CO simulations are presented in Sect. 2.3.3.2 for evaluation of transport similarity in two models from a forward simulation perspective. The coherence of the transport is also examined by analyzing the NMHC photochemical clock in folded results in Sect. 2.3.3.3.

2.3.3.1 FLEXPART folded retroplumes

Transport pathways of Events 2 and 6 are shown in Fig. 2.3. The plume associated with Event 2 arrived at PMO on 15 June 2009, at 06:00 UTC. At five to four days upwind, the plume was lifted from the planetary boundary layer (PBL) of the northeastern US into the free troposphere (3–4 km a.s.l.) by a warm conveyor belt (WCB) that was identified on NCAR weather maps over the northeastern US (NCAR, 2009). The plume was then transported from the northeastern US to the central North Atlantic free troposphere, and during this time it was isolated from the MBL air.

When approaching PMO, the plume experienced a subsidence from about 4 km to 2 km a.s.l. The plume for Event 6 originated over the southern US and arrived at PMO on 21 July 2010, at 06:00 UTC. The plume was transported in the lower FT (1.5–2.5 km a.s.l.) to the east-northeast to the North Atlantic without much change in transport altitude (2–3 km a.s.l.).

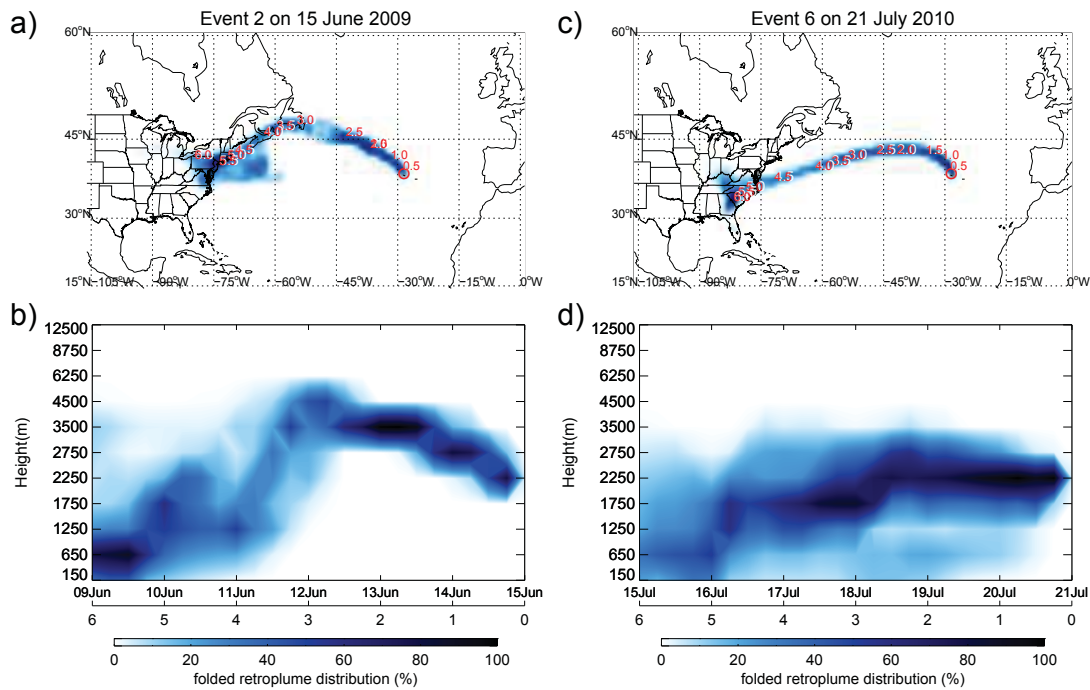


Figure 2.3: FLEXPART folded retroplumes of Event 2 and 6 discussed in text: Panels (a) and (c) are plan views of FLEXPART folded retroplumes with locations at each upwind time labeled by red digital numbers in days; Panels (b) and (d) are vertical distributions of FLEXPART folded retroplumes with dual x-axis labels, showing both date (in UTC) and upwind time. Folded retroplume concentration is shown using a scale normalized to the highest concentration at each upwind time to provide a clearer view of transport pathways.

2.3.3.2 Tagged CO simulations

One potential source of error in the folding process could be the result of differing transport in FLEXPART and GEOS-Chem simulation. In order to evaluate discrepancies in transport between the two models, forward FLEXPART and GEOS-Chem simulations were conducted for the time periods of Events 2 (9–15 June 2009) and 6 (15–21 July 2010) using a tagged CO tracer. The two largest anthropogenic CO emission sources of North America, road transportation and oil production, which comprised approximately 80% of total CO emissions, were extracted from GEOS-Chem and integrated into a FLEXPART forward simulation. GEOS-Chem seasonal and diurnal variations for these emissions were also taken into account in the FLEXPART simulation. Figure 2.4 compares results from the forward FLEXPART simulation with a GEOS-Chem tagged CO simulation for Event 2.

Tagged CO simulations demonstrated close agreement between FLEXPART and GEOS-Chem simulation results. Latitudinal averages of North American CO concentrations in FLEXPART (a, b and c) and GEOS-Chem (d, e and f) are shown in three rows in Fig. 2.4 for three upwind times in which the plume was in the PBL, during lifting, and during transport in the free troposphere, respectively. Similar plumes can be identified in FLEXPART and GEOS-Chem results at all three time steps. Detailed views of CO vertical profiles at the three upwind times (Fig. 2.4g, h and i) show

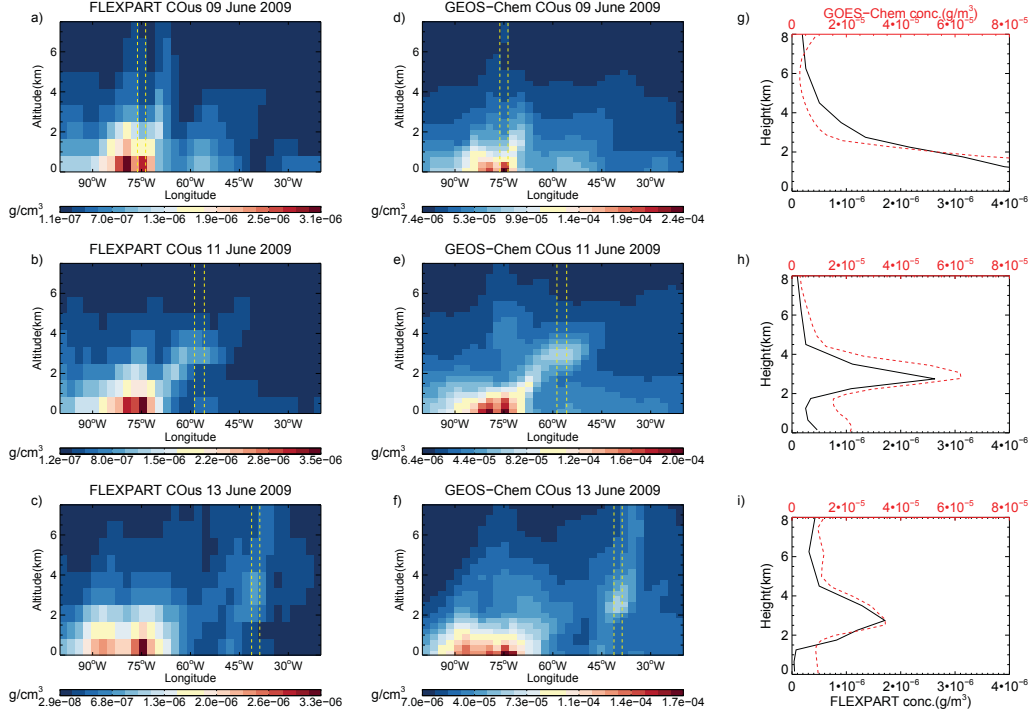


Figure 2.4: Tagged North American CO simulation results for FLEXPART and GEOS-Chem at three upwind times for Event 2: 9 June 2009, 18:00 UTC (upper panel), 11 June 2009, 18:00 UTC (middle panel) and 13 June 2009, 18:00 UTC (lower panel). Concentrations of CO in panels (a–c) for FLEXPART and (d–f) for GEOS-Chem are averaged along the latitudinal region defined by the model domain (see text). Panels (g–i) present tagged CO profiles from FLEXPART (solid black line) and GEOS-Chem (dashed red line) at the three upwind times with locations determined by maximum CO in folded results (UFQs). The plume locations are also marked with two dashed vertical lines in panels (a–f).

that the vertical profiles of CO in FLEXPART and GEOS-Chem agree well at the locations where the plume was predicted. On 9 June, FLEXPART and GEOS-Chem simulations (Fig. 2.4g) indicate that CO was abundant in the lowest 2 km over the US continental region. On 11 and 13 June, similarity is conserved as the pollution plume was lifted and transported over the North Atlantic (Fig. 2.4h and i). It is important to note that the concentration of CO simulated in GEOS-Chem was higher than that

simulated in FLEXPART, which is caused by discrepancies in emission inventories in the two models and accumulation of long-lived CO during the spin-up period of the GEOS-Chem simulation. The same tagged CO simulations were conducted for Event 6, and also exhibit good agreement of transport between the two models (results not shown). The agreement in the two model simulations indicates that the folding technique (Owen and Honrath, 2009) may be used for the analysis.

2.3.3.3 NMHC aging in the folded GEOS-Chem and FLEXPART results

We also evaluated the coherence of the folded results by comparing NMHC aging folded results to theoretical values. Ratios of simultaneously-observed NMHC have been used to study photochemical aging of air masses (McKeen and Liu, 1993; Helmig et al., 2008; Honrath et al., 2008). Correlation analysis of natural logarithms of [n-butane]/[ethane] versus [propane]/[ethane] can be used to determine plume age (Parish et al., 1992). If aging of NMHC in the folded results agrees with the theoretical chemical aging rate predicted by GEOS-Chem, we can conclude that the folded results represent a consistent result with the modeled chemical transformation during the transport.

We examined the NMHC aging rate in the folded results and compared it to aging rate predicted based on theoretical decay, as defined by reaction rates in GEOS-Chem

for Events 2 and 6 (Fig. 2.5). GEOS-Chem combines mixing ratios of all alkanes having carbon number ≥ 4 (ALK4), so ALK4 was used in this analysis of plume aging instead of n-butane. A theoretical decay slope (solid blue line in Fig. 2.5) indicates the decay rate of NMHC against the hydroxyl radical, while a mixing line (dotted black line) indicates the trend if the plume mixes with clean background air. Regressions of NMHC UFQs for both events are significant ($R^2 > 0.9$), which suggests that the folded results simulated transport and aging well. If plumes of different ages had been extracted from GEOS-Chem fields by FLEXPART (indicating discrepancies in transport), folded results of NMHC would deviate from the regression line. Given the similarity in transport observed as discussed in Sect. 2.3.2, the similarity between the theoretical aging slope and folded results of NMHC in both plumes provides additional evidence that the folding technique performed well in extracting Lagrangian information of the transported plumes from the Eulerian model.

The regression slope for the folded results in Event 2 was very close to the theoretical value calculated for reaction with hydroxyl radical only. This may be the result of the transport of a highly compacted plume, as apparent in Fig. 2.3a. The regression line for Event 6 lies between the theoretical decay line and the line for mixing with zero background air, suggesting that the Event 6 plume experienced a higher degree of mixing than that of Event 2. In each panel shown in Fig. 2.5, a measure of decay rate for each day is labeled on the theoretical line (blue labels). Theoretical decay rate was computed by substituting the average folded OH level in each plume into the

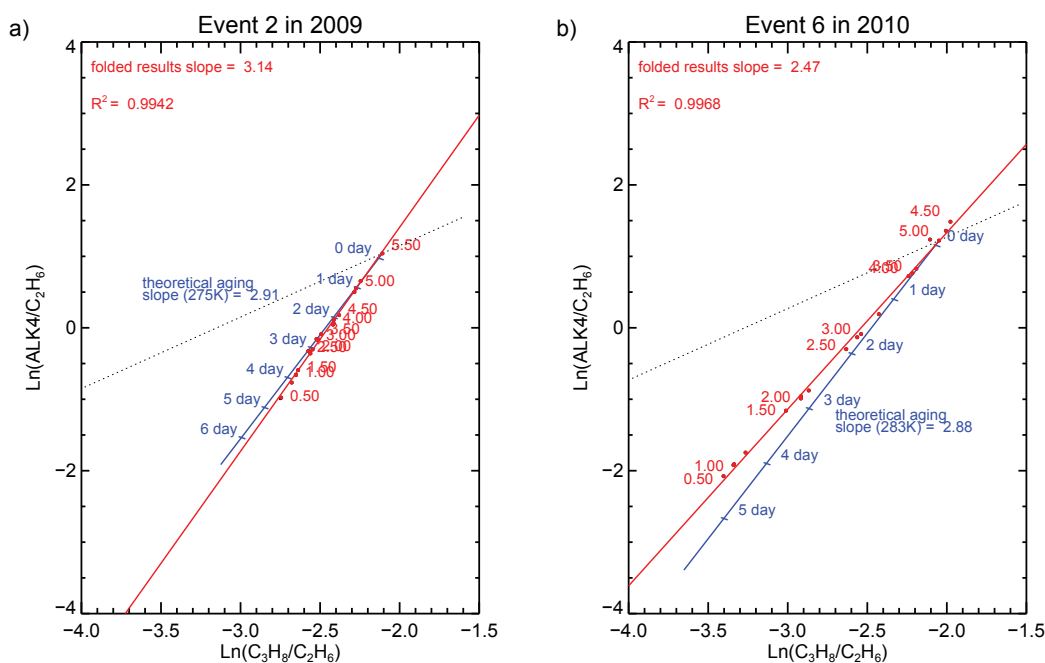


Figure 2.5: Relationship between the natural logarithms of [ALK4]/[ethane] versus [propane]/[ethane] in folded results during transport of Event 2 (a) and Event 6 (b). Folded results (UFQs) are shown in red dots with labels indicate the upwind time at which the simulated data were obtained. Red solid lines indicate the two-sided regressions for folded results, and the slope and R^2 -values of the regressions are given in the top-left corner of each plot. The two lines initiating from the youngest data point represent, respectively, mixing of background air containing negligible concentrations of ALK4 and propane (dotted black line), and theoretical oxidation by OH (solid blue line). Marks on the theoretical decay line provide estimates of decay rate at an average ambient temperature in folded results.

second-order reaction: rate equation of the (lumped) alkanes. The decay rates of the folded NMHC results (red labels) and theoretical results (blue labels) are comparable. Distances between the blue labels are greater for the results in Event 6 than for those in Event 2 because OH levels were higher during transport in Event 6 (as it will be shown in Sect. 2.4), which resulted in relatively faster loss of NMHC. The cause

of the higher OH levels estimated for Event 6 was likely the higher exported ozone concentration in the associated plume.

2.4 Ozone production tendency in North American outflows

In this section we present detailed descriptions of the transport and chemistry that occurred for the two selected events. First, we use the folded GEOS-Chem and FLEXPART retroplume analyses to provide information regarding chemical transformation in the plume during transport (Fig. 2.6). Second, we use GEOS-Chem profiles to focus on vertical distribution of chemical species at several upwind time frames (Figs. 2.7 and 2.8).

2.4.1 Event 2 (9–15 June 2009)

Figure 2.6a–d shows the time series of folded GEOS-Chem and FLEXPART retroplume results (UFQs) for Event 2. These time series include chemistry information during the lifting from the boundary layer, transport in the FT, and start and end of the subsidence phase. The FLEXPART retroplume is also shown within the chemical profiles in order to provide reference as to plume shape and altitude at each time

shown (Fig. 2.6d). In addition, Fig. 2.7 shows profiles of CO, ozone, NO_x , NO_y , OH, specific humidity, as well as production and loss rate of ozone (PO_x/LO_x) from GEOS-Chem simulation results at 4.8, 2.8, 1.8 and 0.8 days upwind. The profiles are shown at the location of the plume, determined to be the horizontal latitude and longitude of the column with the largest UFQs of CO mixing ratios at the selected upwind times.

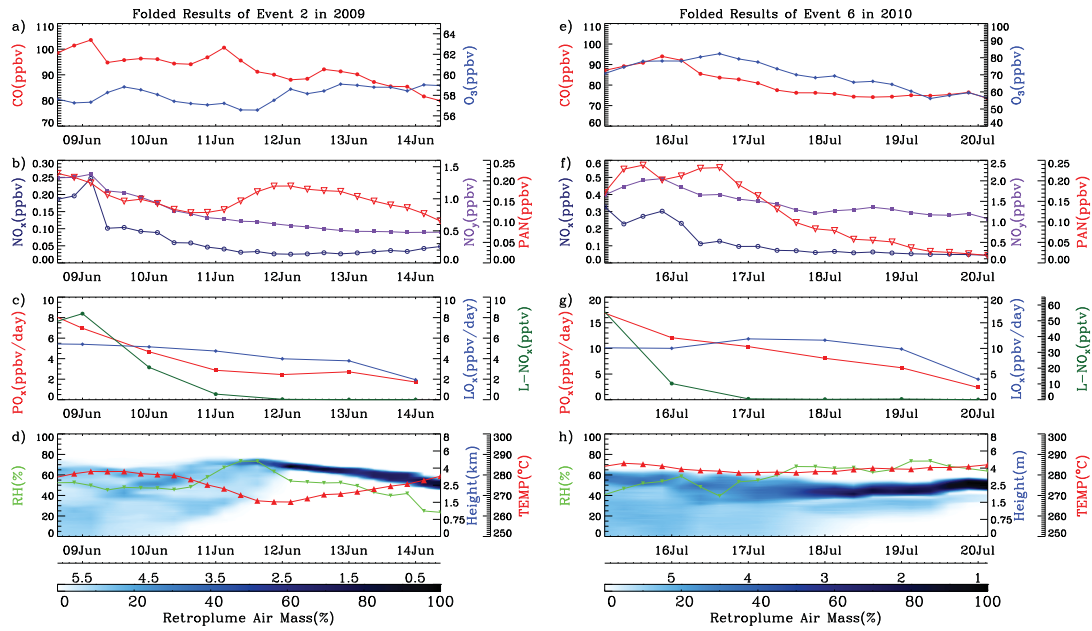


Figure 2.6: Folded results (UFQs) of pollution plumes at each model time step during Event 2 (left column) and Event 6 (right column). Data color corresponds to the respective y-axes. Six-hour averaged UFQs of tracer gases are shown in Panels (a), (b), (e) and (f). Folded daily averaged UFQs of ozone production (PO_x) and loss (LO_x) rates and lightning NO_x ($L\text{-NO}_x$) are shown in Panels (c) and (g). FLEXPART retroplume, temperature and RH in the folded results are shown in Panels (d) and (h), with dual x-axes for date in UTC and upwind time in days.

The vertical distribution of the FLEXPART retroplume (Fig. 2.6d) indicates that

more than half of the retroplume was distributed in the PBL below 1 km at six days upwind. The retroplume contained high levels of primary pollution species such as CO (> 100 ppbv) and NO_x (> 0.2 ppbv), and was in a state of net ozone production (2 ppbv/day; $PO_x = 7.5$ and $LO_x = 5.5$ ppbv/day). This net ozone production value is somewhat lower than typical values reported for mid-latitude polluted areas (approx. 5 ppbv/day; Wang et al., 1998b). However, the lower net production rate is likely due to a lower ozone production rate at higher altitude given that part of the plume extended into the FT.

NO_x from lightning can be an important contributor to O_3 production (DeCaria et al., 2005), however, this is not predicted to be the case in this event. NO_x from lightning (L- NO_x) was estimated to account for a maximum value of 9 pptv of NO_x at this time (Fig. 2.6c), a small fraction (3–5%) in comparison to the total NO_x mixing ratio in the plume (0.18–0.24 ppbv). Thus, lightning NO_x was unlikely to contribute significantly to ozone production during this event.

From five to four days upwind, slightly less than 50% of the retroplume was lifted from the PBL into the FT, and ozone production tendency switched from a state of net production to net destruction (Fig. 2.6c), because of more efficient loss of NO_x than ozone in the pollution plume. In addition, CO mixing ratios dropped slowly as a result of photochemical loss and mixing with background air; levels of oxidized nitrogen species decreased quicker due to relatively shorter photochemical lifetime as

compared to CO in the FT. In Fig. 2.7a, profiles of simulated CO, O₃, NO_x, and PAN, as well as production and loss rate of ozone, show maximum values at about 2 km a.s.l. at 4.8 days upwind. This correlation in species concentrations indicates that the pollution plume was concentrated at 2 km a.s.l. at this stage.

Over 80 % of the simulated plume was lifted up into the FT by three days upwind. During the lifting, temperature dropped from 280 K over the continent to 265 K, while RH increased from ~50 % to 75 % (Fig. 2.6d). Oxidized nitrogen species and ozone decreased slightly, which was due to further dilution and destruction, and ozone production tendency remained in a net destruction status at -2.2 ppbv/day (Fig. 2.6c). At the same time, PAN levels in the plume increased from 0.12 ppbv to 0.18 ppbv (Fig. 2.6b). This accumulation of PAN was likely caused by continuous oxidation of NO_x to PAN combined with the longer lifetime of PAN in the middle of the FT; the lifetime of PAN is 10–100 times longer in the FT than in the PBL (Kleindienst, 1994). The increase in PAN was found to be much higher than the decrease in NO_x during this lifting, which may appear inconsistent if it is assumed PAN is formed primarily from NO_x destruction. When PAN reached its highest mixing ratio at 12:00 on 12 June, due to a slight discrepancy in convection in the two models, the FLEXPART retroplume profile did not entirely match the GEOS-Chem plume profile and only sampled in the upper part of the plume (see Fig. 2.7, Column 1, Panel b). During lifting, the GEOS-Chem plume encountered a potential cloud layer (see RH in Fig. 2.6, Panel d). As a consequence, the FLEXPART

retroplume, which was concentrated above the potential cloud layer, sampled the upper part of the plume where NO_x had already been transformed to PAN or washed out during lifting. The lower part of the plume, where significant NO_x change could be expected, was not sampled by the retroplume because of the disagreement in convective transport in the models. Thus, the change in NO_x in the folded results may have been underestimated. CO and ozone, which are more stable than NO_x , were unaffected by the potential cloud layer on the short timescale, and the retroplume corresponded well to the layers in which CO and ozone were elevated, so the effects on the folded results of CO and ozone were small. After being lifted from the PBL, the plume layer reached an altitude of 3 to 5 km a.s.l., as indicated by the simulated CO profile (Fig. 2.7b). NO_x was almost diluted to the background level, and net loss of ozone was predicted for the entire altitude range of the simulated plume.

Starting from three days upwind, the plume began to decrease in altitude (Fig. 2.6d). The CO mixing ratio in the folded results continued to decrease while ozone mixing ratio increased slightly, with the UFQ of ozone reaching a value of 59 ppbv upon arrival at PMO (Fig. 2.6a). The dilution observed for CO suggests that the increase in ozone is due to production during subsidence. The decrease in PAN mixing ratio suggests that thermal decomposition of PAN occurred in this stage, which resulted in a 50% increase in NO_x and consequent ozone production (Fig. 2.6b), a hypothesis that is confirmed by UFQs of ozone production/loss rate. From three to one

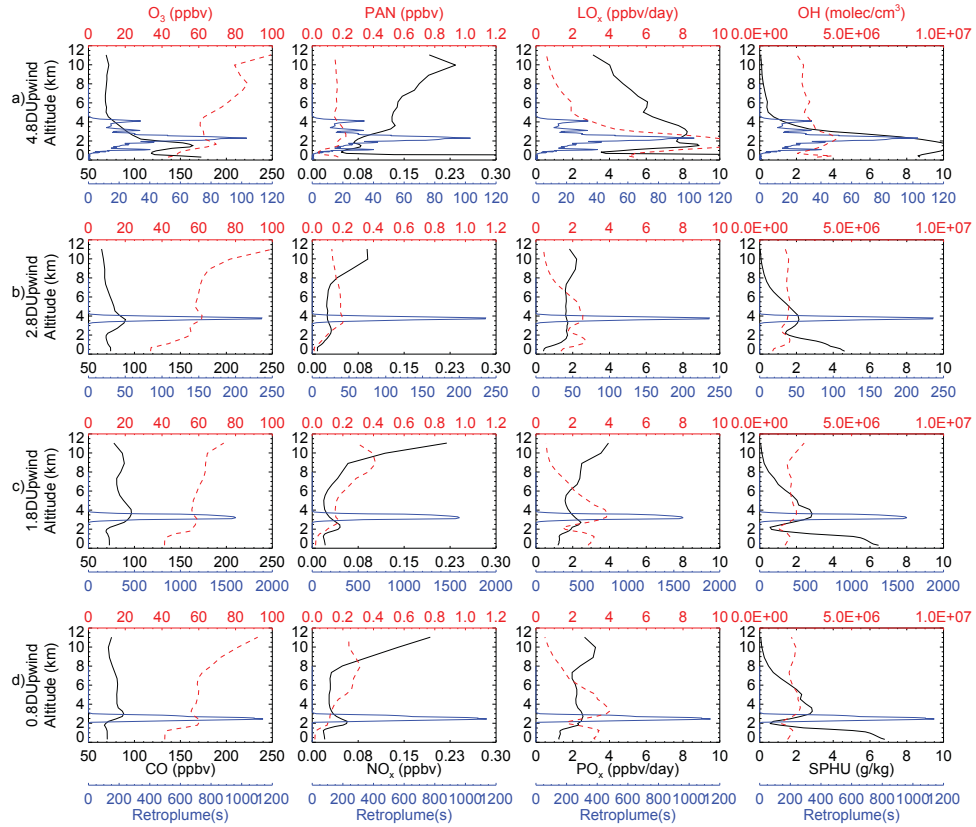


Figure 2.7: GEOS-Chem profiles of tracer gases (CO , O_3 , PAN, etc.), ozone production/loss rates (PO_x , LO_x), OH concentration and specific humidity (SPHU) at four upwind times along the transport pathway for Event 2. The four times were selected to show different stages during the transport. Upwind times are indicated to the left of each row. Plume location and altitude are determined by folded retroplume analysis at the indicated upwind time (Fig. 2.3). Simultaneous retroplumes (in blue) are shown in units of residence time (second), which can be viewed as vertical dispersions of plume air masses over altitude in the column containing the highest folded retroplume concentration such that the retroplume profiles in each row are identical. Each plot shows two GEOS-Chem profiles, the colors of which correspond to the colors of the upper and lower x-axes.

days upwind, due to a slight increase in ozone production rate in the plume and continued decrease of ozone destruction rate, the net ozone destruction decreased from -2.2 ppbv/day to -1 ppbv/day (Fig. 2.6c), and by a half day upwind, the loss rate

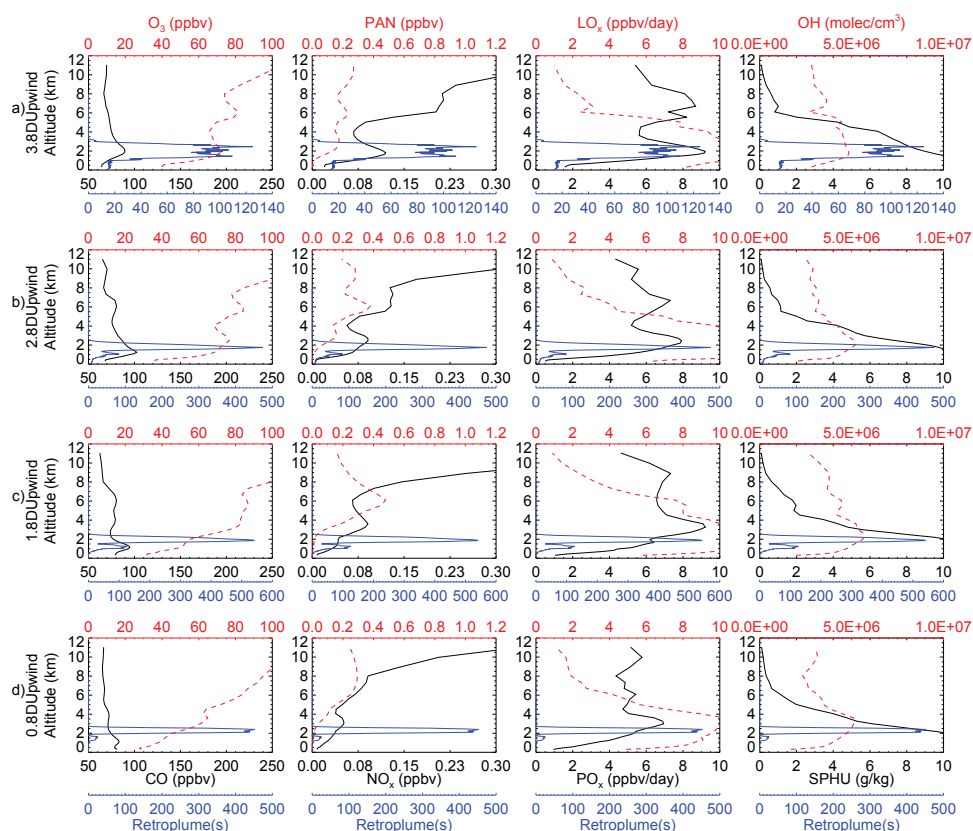


Figure 2.8: Same format as in Fig. 2.7, but for Event 6 in 2010.

of ozone was nearly balanced by the production rate. GEOS-Chem profiles for the arrival dates (Fig. 2.7c and d) indicate that a net ozone production layer (rate of approx. 1 ppbv/day with enhanced NO_x was present at an altitude of ca. 2 km a.s.l. at 1.8 and 0.8 days upwind, which suggests that a net ozone production layer may have covered a broad upwind area over the central North Atlantic. The concentrated CO layer was actually predicted to be higher in altitude than the layers in which NO_x and ozone production rates were elevated, which suggests that net ozone production occurred more efficiently in the lower portion of the pollution plume where

PAN decomposed as a result of higher temperature.

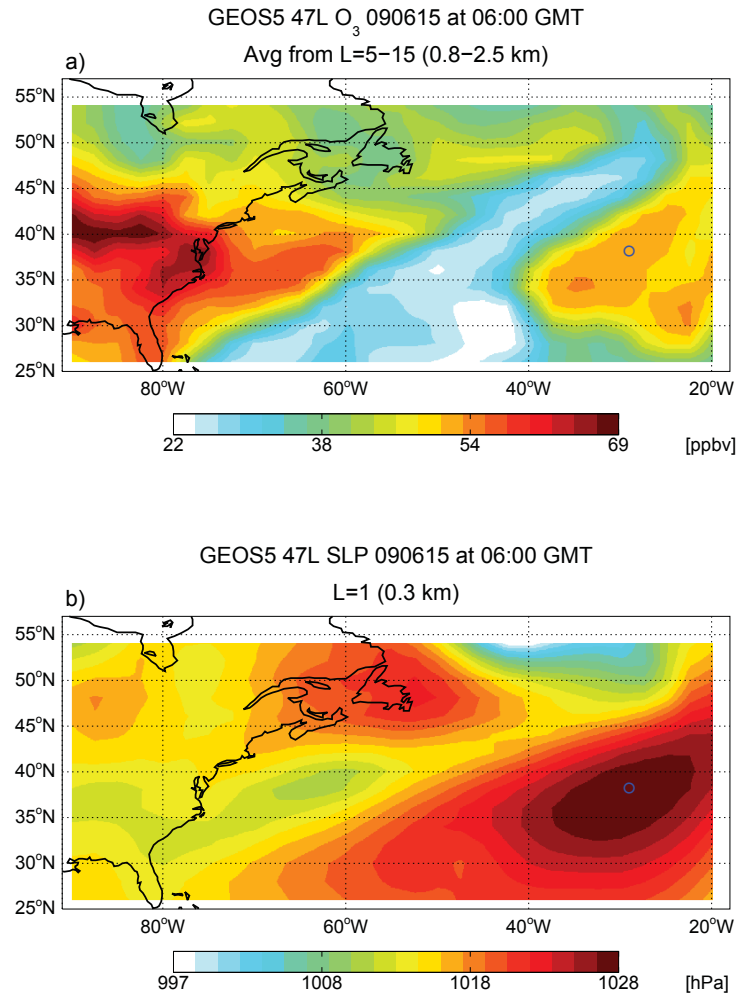


Figure 2.9: GEOS-Chem-simulated ozone mixing ratio averaged from 0.8 to 2.5 km altitude (a) and surface pressure (b) at the arrival time of Event 2 (15 June 2009, 06:00 UTC). The location of Pico Mountain Observatory is indicated with a blue circle.

To demonstrate the link between plume subsidence and the Azores-Bermuda High (ABH), we show a plan view of averaged O₃ in the lower FT (0.8–2.5 km) and surface pressure over the North Atlantic at the time when the plume arrived at PMO

(Fig. 2.9). This GEOS-Chem simulation result indicates that ozone was abundant over the US and southern Canada due to large anthropogenic emissions, and in the region impacted by direct transport from the continent, extending several hundred kilometers to the North Atlantic. An ozone-rich region was also present over the Azores region, isolated from the other regions of enhanced ozone, similar to findings presented by Creilson et al. (2003). We conclude that the region of elevated ozone was a result of subsidence, discussed above. Indeed, the position and shape of the ABH correlates well with the ozone-rich region over the Azores, providing an explanation for air mass subsidence (ABH System) and associated PAN decomposition.

2.4.2 Event 6 (16–21 July 2010)

A similar analysis was carried out for Event 6. The UFQs for Event 6 are shown in Fig. 2.6e–h, and profiles at four upwind times are presented in Fig. 2.8. The plume associated with Event 6 was characterized by low-altitude transport, as described in Sect. 2.3.2. Six to five days upwind, the plume was located in the PBL over the mid-eastern US (Fig. 2.3c). The plume contained high levels of CO and ozone (98 ppbv and 70 ppbv, respectively), and an O₃ production rate of 3–6 ppbv/day ($PO_x = 13–17$ and $LO_x = 10–11$ ppbv/day prior to export. This O₃ production rate is larger than that observed for Event 2 (2.5 ppbv/day. In contrast to Event 2, stable weather conditions were observed at this time over the eastern US. Air masses with fresh pollution

emissions were well mixed, and stagnant atmospheric conditions were favorable for ozone production (Jacob et al., 1993). Simulated NO_x from lightning also showed a maximum prior to plume export. The predicted amount of NO_x produced was less than 10% of the total NO_x UFQs in the simulated plume. This amount was not significant enough to contribute to the simulated ozone production.

From five to four days upwind, the plume was exported to the North Atlantic and travelled mainly at 1–3 km (Fig. 2.6h), presumably above the MBL, which was predicted to be confined to a layer less than 500 m thick by GEOS-Chem (Fig. 2.2). UFQs of temperature in the plume were fairly stable and ranged from 280 to 286 K. RH was higher in Event 6 (60–80%) than in Event 2 (40–60%), which indicates a greater part of the Event 6 plume may have interacted with a cloud layer during transport and thus was not lifted above the boundary layer. Compared to Event 2, these meteorological conditions in the boundary layer may have enhanced destruction of ozone and removal of ozone precursors. Both CO and ozone exhibited a smooth and quick decrease after the simulated plume was exported to the North Atlantic (Fig. 2.6e). The rate of loss in simulated CO and ozone decreased after three days of transport in the North Atlantic, when concentrations approached background levels. UFQs of nitrogen species in the plume for Event 6 also showed similar decreasing trends. In contrast to the PAN accumulation observed in Event 2, PAN mixing ratios in this plume decreased following export from the PBL, which implies that the plume lost most of its potential for ozone production. The plume switched from a net ozone

production to a net ozone destruction state at four days upwind, and stayed in a net destruction state during the rest of the transport period (Fig. 2.6g). Net production of ozone decreased during the entire transport and it decreased much quicker than net ozone loss rate. When the plume arrived at PMO, the plume was in a net ozone destruction state of -2 ppbv/day. Similar transport in the lower FT was found in a Trans-Pacific transport study (Kotchenruther et al., 2001), and in another North American outflow study simulated using WRF-Chem (Lee et al., 2011).

2.5 Potential causes for enhancement in $d[O_3]/d[CO]$ at PMO

In this section, we analyze observations of $d[O_3]/d[CO]$ enhancement at PMO and investigate chemical transformation in plumes based on the above findings. We estimate $d[O_3]/d[CO]$ in the plumes at upwind times for Events 2 and 6 by applying estimates of photochemical loss and gain of CO and ozone during transport. We lack in-situ measurements of trace gases in the plumes when they were exported from North America. In order to evaluate the values of upwind $d[O_3]/d[CO]$, we compare the values to upwind slopes simulated by GEOS-Chem and observational data from the Measurements of OZone, water vapour, carbon monoxide and nitrogen oxides by in-service Airbus aircraft (MOZAIC) Program. The objective of this analysis is to

elucidate factors driving variation in $d[O_3]/d[CO]$ during transport.

2.5.1 $d[O_3]/d[CO]$ evolution during transport of Event 2

For the purpose of this analysis, we assume that the $d[O_3]/d[CO]$ value obtained by regression of the measurement data is the result of mixing between a so-called “pollution plume point” and background air in the central North Atlantic. Therefore, for Event 2, a substitute slope is derived by connecting higher CO and O₃ values in the plume and lower background O₃ and CO values. The plume point for Event 2 (red triangle in Fig. 2.10a) at PMO is determined by averaging the top 10% of O₃ and CO mixing ratios from measurements associated with this event. The background point is estimated from observed O₃ and CO mixing ratios at PMO during specific periods determined to be representative of the North Atlantic regional background. This determination is made by selecting periods with FLEXPART retroplumes having more than 50% of their residence time over the North Atlantic region (defined by latitude from 30° to 48°, longitude from -60° to -15°) and more than 80% of their residence time under a vertical height of 5 km at ten days upwind from PMO. Given a typical transport time from North America to PMO is approximately 6-7 days (Honrath et al., 2004), this choice of upwind time insures that the CO and ozone mixing ratios selected were aged mid-latitude North Atlantic air. The average CO and O₃ mixing ratios for qualified periods were used as the background point (green

circle in Fig. 2.10a). By connecting the plume point (104 ppbv of CO and 60 ppbv of ozone) and the background point (78 ppbv of CO and 30 ppbv of ozone), a substitute slope (value of 1.15, L_1 in Fig. 2.10a) for the regression line of observations (value of 1.37, L_0 in Fig. 2.10a) is obtained. The associated substitute slope can be viewed as a generic $d[O_3]/d[CO]$ value for Event 2 at the central North Atlantic. According to FLEXPART simulation results, transport from tropic regions occurred immediately after this event, so a few observations of clean air (Fig. 2.10a) were included in the event period.

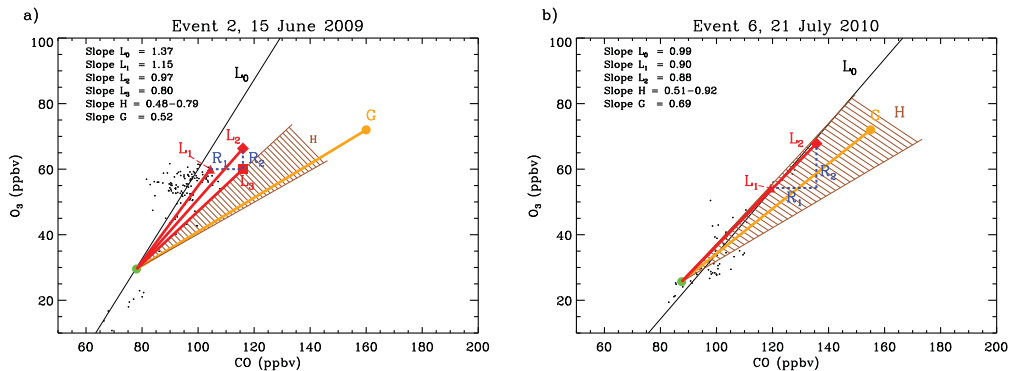


Figure 2.10: Calculations of $d[O_3]/d[CO]$ for the two selected events (a) Event 2; (b) Event 6. Background levels for the central North Atlantic (green circles), and simulated upwind pollution plume data points (red symbols) are defined in the text. Solid black lines (L_0) indicate two-sided regression results of observation data (black dots) at PMO. The brown shaded area indicates the dO_3/dCO range in upwind derived using MOZAIC flight measurements. Line G has an upwind slope that is derived from the GEOS-Chem captured plume. Adjusted lines (L_1-L_3) for each event demonstrate the variation in dO_3/dCO according to chemical transformation pathways (R_1-R_2) during transport.

To derive the upwind slope values of the plume for Event 2, we estimate CO and O_3 mixing ratios in the plume at five days upwind (near the coast) based on folded

results from Sect. 2.4. As previously discussed, transport of Event 2 is characterized by initial lifting from PBL into the free troposphere and subsequent subsidence near PMO. Since CO transformation is less affected by transport height and temperature, we begin by estimating the upwind CO mixing ratio in the plume by calculating CO production and CO loss over the transport time. By knowing the production/loss rate of CO in the folded results, we calculate the percent production/loss relative to CO mixing ratio in the folded results for each day. For example, if the CO net destruction rate were -1.16 ppbv/day ($PCO = 1.25$ and $LCO = 2.41$ ppbv/day), we compute a 1.4% loss relative to an average CO mixing ratio of 85 ppbv during the last day of transport. By doing this computation iteratively for each day, we obtain a total loss of 10% of CO during five days of transport. To compare this net CO loss with values found by Honrath et al. (2004), we can compute the CO loss based on reaction with OH, and CO production based on oxidation of hydrocarbons. By applying an average OH concentration of 2.8×10^6 molecules/cm³, Honrath et al. (2004) estimated a 23–27% CO loss due to reaction with OH during 5–6 days of transport from the US East Coast to PMO. The average OH concentration estimated in our folded results was 3.0×10^6 molecules/cm³, which gives a 25% loss of CO by reaction with OH in the five days of transport. Considering that in the folded results, the predicted CO production rate from the oxidation of hydrocarbons is about half of the CO destruction rate, a net loss of CO of 13% is expected, consistent with the estimation of CO loss calculated iteratively of 10%. According to an estimated 10%

loss of CO, we expect the plume point (red triangle in Fig. 2.10a) to move to the right to a CO level of 116 ppbv at five days upwind following process R_1 . By using the same iterative calculation of relative ozone production/loss for each day, we compute an 11 % loss in ozone for the transport period, moving the plume point (following R_2 in Fig. 2.10a) up to an ozone level of 66 ppbv (red diamond in Fig. 2.10a). The slope of the line (L_2 in Fig. 2.10a) connecting this upwind plume point and the background point, which is presumably unchanged, is 0.97. Comparing L_1 and L_2 , we conclude that both CO and ozone transformation can affect the slope. Net ozone loss has negative contribution to the slope while net CO loss has positive contribution to the slope. It is also important to note that although the averaged net ozone production rate during the 5 day transport period was negative, the slope increases from L_2 to L_1 as a result of significant CO loss. This finding contradicts the intention of use of $d[\text{O}_3]/d[\text{CO}]$ as an indicator of net ozone production. To our knowledge, prior to this study, CO loss has been pointed out as a potential explanation for enhancement in $d[\text{O}_3]/d[\text{CO}]$ only in the study by Real et al. (2008).

In order to evaluate the upwind slope L_2 , we compare it with other estimations of slope values derived from near-coast pollution plumes inferred from our GEOS-Chem simulations. At the time of export from North America (9 June), GEOS-Chem profiles (not shown) indicated that the plume associated with Event 2 contained 160 ppbv of CO and 72 ppbv of ozone. If this plume (orange circle in Fig. 2.10a) were mixed with the background (green circle) the derived upwind slope would be 0.52 (Line G).

We also investigated upwind pollution plumes by using flight measurements obtained from the MOZAIC Airborne Program. To estimate the composition of the Event 2 plume when it was exported from eastern North America, we chose the CO and ozone profiles from Philadelphia, the closest MOZAIC airport to the location of the event origin (see Fig. 2.3) from 2008–2010. The 2008 data were included because there were only a few profiles collected in summertime 2010. CO and ozone mixing ratios measured from altitude 2 km to 3 km were considered to represent lower free troposphere air. The top 10% of CO mixing ratios at this level were treated as highly polluted air and were used to determine the potential range of the initial plume conditions for Event 2. By connecting these CO and ozone mixing ratios in the plume with the North Atlantic background, we obtained a range in upwind $d[\text{O}_3]/d[\text{CO}]$ from 0.48 to 0.79 (H-range in Fig. 2.10a). This range is a little larger than those of recent satellite observations downwind of eastern North America (0.4–0.6; Voulgarakis et al. (2011)), but consistent with values measured near coastal areas observed during the ICARTT Campaign (0.81 and 0.72; Zhang et al. (2006)).

Compared to the slope range of the G- and H-lines, the upwind slope for Event 2 based on the folded results (1.15 for L_2) is greater than the upper end of the slope range of G- and H-lines and is probably overestimated. We speculate that our calculation of ozone transformation during transport in Event 2 underestimated net ozone production during plume subsidence, which is likely caused by numerical diffusion in GEOS-Chem. Due to retention of NO_x in the PAN chemical reservoir during

rapid lifting from the PBL and subsequent transport at high altitude (> 3 km), the plume had a potential for ozone production during subsidence in the last two days of transport as PAN decomposed to NO_x . This sequence of events, including net ozone production during plume subsidence, occurred in a limited space. However, the NO_x generated was immediately diluted in GEOS-Chem grid cells as a result of numerical diffusion, and as a result, net ozone production within the plume would be underestimated in GEOS-Chem simulations and associated folding calculations. As discussed in Sect. 2.3, the pollution plume for Event 2 was compact during transport, as such was vulnerable to numerical diffusion, which may have amplified the underestimation of NO_x and net ozone production in the plume. This artifact can be minimized by using higher resolution chemical models, which reduces the magnitude of artificial mixing with the ambient air. If we assume a hypothetical, averaged, net ozone production rate of 2.1 ppbv/day (7.2% net ozone production) during the last two days of transport instead of the simulated, averaged, net ozone destruction rate of -0.6 ppbv/day (3.7% net ozone loss averaged from the folded result values on upwind days 2 and 1; Fig. 2.6c), there would be no accumulated ozone change (0% net ozone production) for the 5 day transport period because the net ozone loss in the first three days would be compensated for by this hypothetical higher net ozone production rate. In this case, the upwind plume point for Event 2 would remain at an ozone level of 60 ppbv (red square in Fig. 2.10a), producing an upwind slope of 0.80 as show in Fig. 2.10a for L_3 , instead of ozone being increased at five days upwind to

account for ozone destruction predicted in the folded result (R_2 ; slope of $L_2 = 0.97$). Compared with L_2 , the slope of L_3 shows better agreement with the upwind slopes of Lines G and H, which means that the net ozone production was likely closer to the assumed value (2.1 ppbv/day) in the final two days of transport. In the remote North Atlantic, this ozone production rate is possible because of the considerably higher ozone production efficiency resulting from fresh NO_x production. Based on aircraft measurement of NO_x in the FT, Reeves et al. (2002) calculated a pollution plume having a net ozone production rate of 9.6 ppbv/day with a simultaneously measured $\text{NO} > 60$ pptv. When the plume was lifted, GEOS-Chem and the folded results could similarly underestimate PAN accumulation due to numerical diffusion, which would also result in underestimation of net ozone production during subsequent subsidence. Correction for this underestimation could move the slope of L_3 even lower and closer to the G- and H-lines.

If the explanation that GEOS-Chem underestimates instantaneous ozone production is correct, enhancement of $d[\text{O}_3]/d[\text{CO}]$ in Event 2 (from L_3 to L_1 in Fig. 2.10a) was the result of a combination of ozone production and CO loss during transport. Compared to upwind CO and ozone mixing ratios in the upwind plume simulated in GEOS-Chem (orange circle), the upwind CO and ozone mixing ratios calculated above (red square on L_3) are much lower. This discrepancy is a result of our calculation based on diluted pollution plumes observed at PMO. However, the dilution effect, i.e. mixing, does not change the slope values because mixing of the pollution plume with

background air would only move the plume point along the derived slope line (L_3) in a direction opposite to the background point.

2.5.2 $d[O_3]/d[CO]$ evolution during transport of Event 6

The evolution of $d[O_3]/d[CO]$ in Event 6 can be studied using a similar approach (Fig. 2.10b). Averaging the top 10% of CO and ozone mixing ratios for the data observed for Event 6 produces a computed plume point of 119 ppbv CO and 54 ppbv ozone at the arrival time (red triangle in Fig. 2.10b). Similarly, the North Atlantic background CO and ozone for summertime 2010 were found to be 88 ppbv and 26 ppbv, respectively (green circle in Fig. 2.10b). The derived line connecting these two points exhibits a slope of 0.90 (L_1 in Fig. 2.10b) as a substitute for the regression slope for Event 6 (0.99; L_0).

According to the folded results, both CO and ozone concentration decreased during transport, and no net ozone production was found, so we expect the plume point for Event 6 to move to the upper right in Fig. 2.10b when tracing back five days upwind. By using the same approach for Event 2, we estimate 12% CO loss during transport for Event 6, more loss than in Event 2 due to higher OH levels in the plume (4.5×10^6 molecules/cm³ daily average value from GEOS-Chem), which may be a result of more efficient ozone production and export at lower altitude. This

CO loss moves the plume point horizontally to the right in Fig. 2.10b (following R_1). Similarly, we estimate 20% ozone loss during the entire five days transport. By adjusting for loss of CO (R_1 in Fig. 2.10b) and of ozone (R_2), the plume point is moved to 136 ppbv CO and 68 ppbv ozone for five days earlier (red diamond in Fig. 2.10b), which, when connected to the background point, produces an upwind slope of 0.88 (L_2). Similarly, we estimate upwind slopes by using GEOS-Chem simulation and plumes observed during previous aircraft campaigns. An upwind plume associated with Event 6, having 155 ppbv of CO and 72 ppbv of O_3 , was captured by GEOS-Chem five days upwind. Thus, a value of 0.69 is computed as the upwind slope based on the GEOS-Chem simulation (Line G). We also estimated the CO and ozone composition for Event 6 plume when it was exported from North America by using the same approach as done for Event 2. Profiles from Atlanta were used because it was the closest MOZAIC airport to the location of export in Event 6. By connecting the estimated CO and ozone composition and the background point, we obtained a range of upwind $d[O_3]/d[CO]$ from 0.51 to 0.92 (H-range in Fig. 2.10b).

The derived upwind slope of Line L_2 (0.88) is very close to the slope of L_1 (0.90). Far away from continental pollution sources, the plume for Event 6 lost most NO_x and PAN for net ozone production after export. As a result, significant ozone loss occurred in transport to PMO, which resulted in a negative contribution to $d[O_3]/d[CO]$. However, this negative contribution was partially compensated by significant CO loss during transport. Therefore, the downwind slope (of L_1) has a similar value to the

slope of L_2 . Both L_1 and L_2 slopes fall in the range of the estimated upwind slopes (slopes of G- and H-lines ranging from 0.51–0.92), which suggests a low variation in $d[\text{O}_3]/d[\text{CO}]$ during transport for Event 6. Different from Event 2, for Event 6, numerical diffusion in GEOS-Chem had a minor effect on estimated CO, ozone production/loss because chemical transformation was more continuous, and intensive and abrupt chemical processes, such as net ozone production during subsidence, were absent. The over-dilution caused by numerical diffusion has less significant effect in Event 6 than in Event 2 because the plume for Event 6 experienced more efficient mixing during transport. This type of mixing is better approximated as numerical diffusion in GEOS-Chem as compared to the mixing during transport associated with Event 2 discussed above. As a result, better agreement between the estimated upwind event plume point (red diamond, Fig. 2.10b) and the adjusted simulated and previously-observed plume points (upper end of G- and H-lines) is observed.

Usually, net ozone production is believed to be the reason for $d[\text{O}_3]/d[\text{CO}]$ enhancement in remote regions (Parrish et al., 1993). Here we observed that variation in $d[\text{O}_3]/d[\text{CO}]$ is not sufficiently explained by net ozone production/loss alone, as previously suggested by Voulgarakis et al. (2011). Instead, significant CO loss during the two transport events was found to contribute to increases in $d[\text{O}_3]/d[\text{CO}]$. As a result of sufficient ozone export in the two event plumes, high OH concentrations were found in our simulation results (3.0×10^6 molecules/cm³ for Event 2; 4.5×10^6 molecules/cm³

for Event 6 as diurnal average during the transport period) in comparison with typical background OH levels of approximately 1.0×10^6 molecules/cm³. Elevation in OH level, caused by high ozone concentration in the plumes, in turn accelerates CO oxidation, which suggests that use of CO as an inert gas tracer of pollution events in the analysis of $d[\text{O}_3]/d[\text{CO}]$ in pollution plumes is biased by a contribution from significant loss of CO.

2.6 Conclusions

We used measurements of atmospheric tracer gases at PMO, the transport model FLEXPART, and the chemical transport model GEOS-Chem to identify transport events that were mainly impacted by North American anthropogenic emissions in summers of 2009 and 2010. Both FLEXPART and GEOS-Chem were able to simulate the transport processes of the two selected events, and the agreement between the two model simulations of plume transport dynamics allowed us to examine the aging and chemical transformations occurring in the plume with a semi-Lagrangian framework.

CO enhancement observed at PMO was used as a primary indicator of the impact of pollution plumes. Correlation coefficients of $d[\text{O}_3]/d[\text{CO}]$ for selected events show significant enhancement in pollution-impacted measurements, and regression analyses

of $d[\text{O}_3]/d[\text{CO}]$ in selected plumes exhibit high correlation ($R^2 > 0.5$). We successfully identified two North American anthropogenic pollution plumes by examining CO sources, trajectory analyses, and excluding influence of mechanically forced upslope flow to the Observatory. The folded GEOS-Chem and FLEXPART technique was applied to study chemical evolution in the two selected events. Lagrangian information including plume dispersion and transport in FLEXPART were used to extract chemical transformation information in GEOS-Chem Eulerian fields. Although the accuracy of the folded results is likely limited by numerical diffusion in GEOS-Chem and transport discrepancy between the models, these results indicate that meteorological conditions and transport pathways largely determined the chemical transformation in the pollution plumes. Based on these analyses, two parameters, transport height and concentration of hydroxyl radical, are important determinants of production and loss of air pollutants during transport over the North Atlantic. For example, our results lead us to conclude that NO_x was converted into PAN during quick lifting into the middle free troposphere in the beginning of Event 2, while most of the reactive nitrogen species were lost to deposition at low altitude in Event 6. Exported plumes are usually transported directly from the northeastern US, followed by looping south to intercept PMO. During Event 2 in 2009, the plume experienced pronounced subsidence caused by the ABH when approaching the Observatory. NO_x released through thermal decomposition of PAN created a net ozone production layer at 2 km a.s.l. in the Azores. For Event 6, the potential for ozone production was low due to active

mixing at low altitude, and ozone was primarily destroyed during transport. The enhancement in $d[\text{O}_3]/d[\text{CO}]$ for Event 6 was instead the result of efficient CO loss during transport. High ozone and OH levels in the pollution plumes accelerated CO loss, which brings into question the validity of assuming CO to be a conserved passive tracer of pollution plumes. We conclude that enhanced $d[\text{O}_3]/d[\text{CO}]$ values, which have been frequently used as indicators of ozone production in transport plumes, may not reflect ozone chemistry only. CO destruction in the plume can also explain the higher $d[\text{O}_3]/d[\text{CO}]$ observed for Event 2, when both CO loss and ozone production were identified.

Chapter 3

Ten-year chemical signatures

associated with long range

transport observed in the free

troposphere over the central North

Atlantic¹

¹This chapter is based based on material that is intended for publication as Zhang et al., Ten-year chemical signatures associated with long range transport observed in the free troposphere over the central North Atlantic

3.1 Introduction

The persistent westerly winds in the mid-latitude regions powers transpacific transport (e.g., Heald et al., 2006; Dunlea et al., 2009) and transatlantic transport (e.g., Huntrieser et al., 2005; Fehsenfeld et al., 2006). These studies documented the impacts of long-range transport on air quality in downwind regions. Specific attention has been given to study the links between the observed chemical concentrations and properties and transport patterns (e.g., transport sources, distance, height, etc.). For example, Cooper et al. (2001c) classified and studied major air mass types at a ground site in northern Michigan. They found that transport from the south brought polluted air from the populated regions, while transport from the north mainly delivered clean air from Canadian regions. Liang et al. (2004) used GEOS-Chem to simulate CO enhancement caused by long-range transport from Asia at Cheeka Peak Observatory, Washington (U.S.). They classified several transport types observed between June 2001 and May 2002 and found that the CO enhancement varied from 33 to 65 ppbv for different export heights and weather systems in the Asian boundary layer. Fischer et al. (2011) found high levels of PAN associated with colder air transport to Mount Bachelor, a free troposphere site in central Oregon (U.S.). Cain et al. (2012), using a trajectory ensemble to simulate ozone production for long-range transport, found ozone photochemical loss (-5 ppbv/day) in transports at low altitudes (<2 km) and also ozone production in a wildfire plume at higher altitude (4-5 km). The studies

revealed how the composition of imported air pollution could vary in differing circumstances, and thus helped with understanding of pollution transport and air quality issues.

Chemical transformation during transport can be inferred by examining relationships of observed chemical concentrations after long-range transport. The reduced major axis (RMA) slope takes into account variability in both x- and y-coordinates (Ayers, 2001), so it is a proper tool for correlation analysis of observed trace gases. For example, $d[\text{O}_3]/d[\text{CO}]$ has been used as a measure of ozone enhancement in North America and regions downwind (e.g., Parrish et al., 1993). Variations in the slope observed in previous studies reflect differences in air composition and differing ozone chemistry. A $d[\text{O}_3]/d[\text{CO}]$ value of 0.3 was found to be a signature value for rural sites in eastern North America, and was concluded to be a result of mixing of fresh pollution emissions and aged air mass [Chin et al., 1994; Cooper et al., 2001]. Honrath et al. (2004) found a higher summertime $d[\text{O}_3]/d[\text{CO}]$ (~ 1.0) in the free troposphere over the central North Atlantic and suggested the slope was the result of potential ozone production during transport from North America. Cooper et al. (2001a) investigated $d[\text{O}_3]/d[\text{CO}]$ in different airstreams associated with mid-latitude cyclones, and suggested that the slope could be different depending on air composition and photochemistry in the airstreams. These variations are expected to be better understood by studying $d[\text{O}_3]/d[\text{CO}]$ for different transport patterns.

Non-methane hydrocarbons (NMHC) undergo reactions with OH radicals and atmospheric deposition during long-range transport. Their decay rates in reactions with OH are determined by the size and structure of the NMHC molecule. Lighter NMHC (C₂-C₅) decay slower than bigger organic species and their concentrations are measurable after long-range transport. The differences in their decay rates produce observable patterns in their mixing ratios. Ratios of NMHC in the atmosphere have been used to reflect photochemical ages of air masses (McKeen and Liu, 1993). The natural logarithms of [n-butane]/[ethane] versus [propane]/[ethane] has been used as a photochemical clock of air masses (Parrish et al., 1992). Ratios of NMHC isomers are usually constant in transport, but can be changed due to oxidation reactions with other chemicals. Increased [i-butane]/[n-butane] was found in the polar marine boundary layer, which was due to faster n-isomer oxidation by chlorine atoms emitted from the ocean (Hopkins et al., 2002). NMHC ratios have proven to be useful tools for studying air mass ages and to study chemical transformation during long-range transport (McKeen and Liu, 1993).

Long-term observations of trace gas concentrations in the free troposphere have been conducted at a remote and elevated site, Pico Mountain Observatory (PMO), in the central North Atlantic. The ten-year record of observations allows us to study potential chemical and physical processes responsible for chemical variations in atmospheric composition after long-range transport. The observatory is far from large emission sources, which makes it a perfect site for studying the chemical and physical processes

during long-range transport. The Objectives of this work are to provide a categorization of major transport patterns that result from different pollution sources and environmental conditions, and to understand the chemical signatures associated with the transport patterns. We focus on ozone, ozone precursors and other chemical signatures in spring (April-May), summer (June-August) and fall (September-October) during periods when the Observatory was operated.

3.2 Method

3.2.1 PMO introduction and measurements

PMO was established in summer 2001 on top of the Pico Mountain (38.47°N, 28.40°W, 2,225 m a.s.l.) in the Azores Islands. The elevation of PMO above the remote North Atlantic ocean makes it a great remote site for conducting research to understand transported gaseous and particle species in the free troposphere. Since the founding of PMO, a series of studies based on observations of airborne species was published, including studies on enhancement of ozone and ozone precursors (Honrath et al., 2004; Owen et al., 2006), anthropogenic and boreal fire emission impacts (Lapina et al., 2006; Val Martín et al., 2008a), seasonal cycles of hydrocarbons (Helmig et al., 2008), as well as aerosol properties (Dzepina et al., 2014) and composition (China et al., 2015).

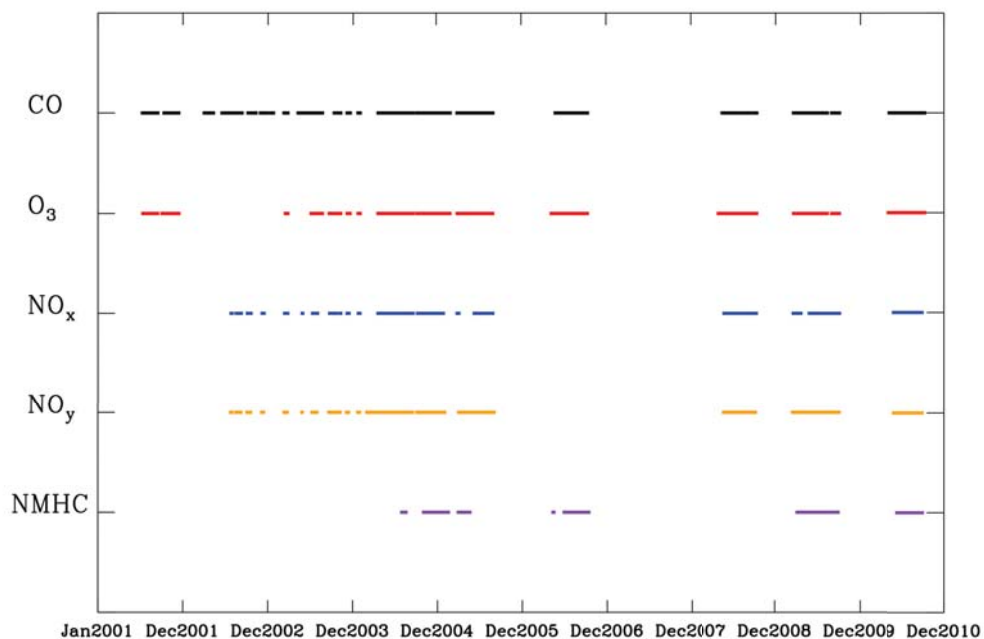


Figure 3.1: Coverage of the trace gas observations used in this study. Data of CO, ozone and NO_{xy} are 30-min averages. Data of NMHC are hourly averages.

The work here uses available measurements of carbon monoxide (CO), ozone (O_3), mono-nitrogen oxides ($NO_x=NO+NO_2$), total reactive nitrogen (NO_y), non-methane hydrocarbons (NMHC) through years 2001-2011 (data coverage is given in Figure 3.1) to look for chemical signatures of different air masses.

3.2.2 Transport and pollution tracer simulations

The Lagrangian particle dispersion model FLEXPART (version 8.2; Stohl et al. (1998)) was used to simulate air mass transport to PMO. The backward mode was applied in this study to build a ten-year archive of transport trajectories initialized from PMO. Backward simulations were launched every three hours from PMO. Three-hour meteorology fields of Global Forecast System (GFS) and its Final Analysis (FNL), featured with 1°horizontal resolution and 26 vertical levels, were used to drive FLEXPART for the years 2005-2011. Three-hour meteorological fields from the European Center for Medium range Weather Forecasting (ECMWF) were used in simulations for 2001-2004. The output was saved in a grid with a horizontal resolution of 1°latitude by 1°longitude and eleven vertical levels from the surface to 15,000 m a.s.l.

In the backward mode of FLEXPART, a passive tracer consisting of tens of thousands of air parcels is released from the receptor (PMO) and advected and dispersed backwards in time, resulting in a spatial distribution of residence time (RT) at every upwind step, referred to as a retroplume. Given this spatial distribution, we can calculate the ratio of the plume (portion of the air parcels) distributed in the spatial domains of interest to the entire dispersed plume, which can be used to categorize transport in concerned regions and heights. In FLEXPART, retroplumes can also be converted to a distribution of sensitivity factors (rather than RT) that qualify the

source-receptor relationship (Owen and Honrath, 2009). By folding (i.e., multiplying) the sensitivity factor with emission inventories, we are able to calculate tracer concentrations at the receptor contributed by a certain emission source (Seibert and Frank, 2004). In this study, evaluation of the influence from pollution emissions was obtained by multiplying retroplumes with CO emission inventories from the Emissions Database for Global Atmospheric Research (EDGAR version 3.2; Olivier and Berdowski (2001)) and the Global Fire Emissions Database (GFED v3.1, daily averaged fire emissions; Mu et al. (2011)), and is hereafter called FLEXPART CO.

3.2.3 Classification of transport patterns

In this section, we list the constraints used to determine transport patterns. The constraints were selected based on our knowledge and the feasibility of the analyses. By analyzing FLEXPART products and meteorological data, we identified several major transport patterns in the 10-year record of trace gas observations. The constraints are also summarized in Table 3.1.

Table 3.1
 Constraints to define transport patterns, abbreviations of the transport patterns and the estimated occurrence frequencies in spring, summer and fall.

Transport Patterns	Abbrev.	Constraint*	Occurrence Frequency ** %		
			Spring	Summer	Fall
North American flow	NA	1. RT over North America in 0-5km a.s.l. greater than 50% for at least 1 day.	40.0	30.0	32.0
NA affected by anthropogenic emissions	NA-anthro	1. North America anthropogenic CO contribution greater than 15 ppbv, fire <15 ppbv	16.3	15.1	13.1
NA-anthro lifted during transport	NA-anthro-lifted	1. Same as NA-anthro 1. 2. RT in a vertical range 0-2.5km reduced 30% within 24hour during 0-15 days upwind	4.0	2.7	2.5
NA-anthro within or close to MBL	NA-anthro-low	1. Same as NA-anthro 1. 2. RT within 0-2.5km greater than 40% from 0-5days upwind	3.1	1.7	<1.0
NA-anthro quick transport	NA-anthro-young	1. Same as NA-anthro 1. 2. CO age from anthropogenic emissions less than 8 days	6.7	4.3	4.0
NA-anthro aged transport	NA-anthro-aged	1. Same as NA-anthro 1. 2. CO age from anthropogenic emissions greater than 10 days	6.2	5.3	4.5
Wildfire affected	Fire	1. Wildfire CO contribution greater than 15 ppbv, Anthropogenic <15 ppbv	<1.0	7.3	2.6
Fire quick transport	Fire-young	1. Same as Fire 1. 2. CO age from anthropogenic emissions less than 8 days	<1.0	2.5	1.0
Fire slow transport	Fire-aged	1. Same as Fire 1. 2. CO age from anthropogenic emissions greater than 10 days	<1.0	3.0	1.3

* RT = residence time of FLEXPART retrorplumes

** Spring = April-May; Summer = June-August; Fall = September- October

Table 3.1 Continued.

Transport Patterns	Abbrev.	Constraint*	Occurrence Frequency ** %	
			Spring	Summer
European flow	EU	1. RT over Europe greater than 50% for at least 1 day	1.8	<1.0
African flow	AF	1. RT over Africa greater than 50% for at least 1 day	<1.0	2.6
North Atlantic free troposphere background	NATL	1. RT over North Atlantic in 0-5km a.s.l. greater than 70% through 0-10 days upwind	16.7	19.3
Subsidence from above free troposphere	Upper	1. RT less than 40% in 0-5km through 2-12 days upwind	2.1	2.3
Upslope flow	Upslope	1. PBL height greater than altitude of Pico OR DSL less than PBL height	8.2	3.5
				6.7

* RT = residence time of FLEXPART retroplumes

** Spring = April-May; Summer = June-August; Fall = September-October

3.2.3.1 Air mass origin

The primary factor considered for categorizing the transport is where the transport to PMO originates. Transport origin was determined based on distributions of upwind RT over the North Atlantic Ocean and the surrounding continents. Figure 3.2a shows the vertical distribution of upwind residence time averaged for the retroplumes in an entire year (2011). These results indicate that the retroplumes distribute mainly over the North Atlantic for 0-3 days upwind. The North American RT contribution starts to appear ~ 3 days upwind, indicating the shortest transport time from North America to PMO. The North American RT reaches its maxima about 7-8 days upwind with a maximal RT ratio of 0.22. We use a RT ratio greater than this average value to determine the transport from a targeted continent. In this study, retroplumes that have greater than 50% RT distributed in the low-middle troposphere (0-5 km a.s.l.) over North America for a period longer than one day were defined as North American outflows, and were assigned the abbreviation “NA”. The altitude limitation is applied for targeting terrestrial sources because the air composition from the upper troposphere has a different chemical signature. European and African transport were defined similarly and were assigned abbreviations of “EU” and “AF”, respectively. The North Atlantic free troposphere background, “NATL”, is defined by a higher percentage (70%) of RT and a longer time limit (10 days) over the North Atlantic in order to reduce the probability of overlapping with air masses originating over the

continent.

3.2.3.2 Impact of pollution emissions and air mass age

FLEXPART CO is used in this study to determine periods that were affected by pollution emissions. FLEXPART CO estimates the CO enhancement caused by pollution emissions. We use a FLEXPART CO mixing ratio of 15 ppbv (compared to 80-100 ppbv as a typical background CO at PMO) as the cutoff in the determination of impacts of pollution emissions. The 15 ppbv used here equals the standard deviation of the bulk CO measurement for the ten-year period. We determined the time periods of different air mass types by examining FLEXPART CO from anthropogenic or wildfire emissions. This method successfully predicted transport of pollution emissions in previous studies focusing on aerosol composition (Dzepina et al., 2014) and particle morphology at PMO (China et al., 2015). Although the emissions of CO and reactive nitrogen oxides over the North America have decreased in recent decades, we used the same anthropogenic emission inventory here in order to keep a consistent FLEXPART CO threshold for identification of affected periods in different years. The simulated FLEXPART CO shows a wide range from 3 ppbv (small emission influence) to more than 150 ppbv (large emission influence). An example of FLEXPART CO resulting from anthropogenic and wildfire emissions originating from different continents is given in Figure 3.3a.

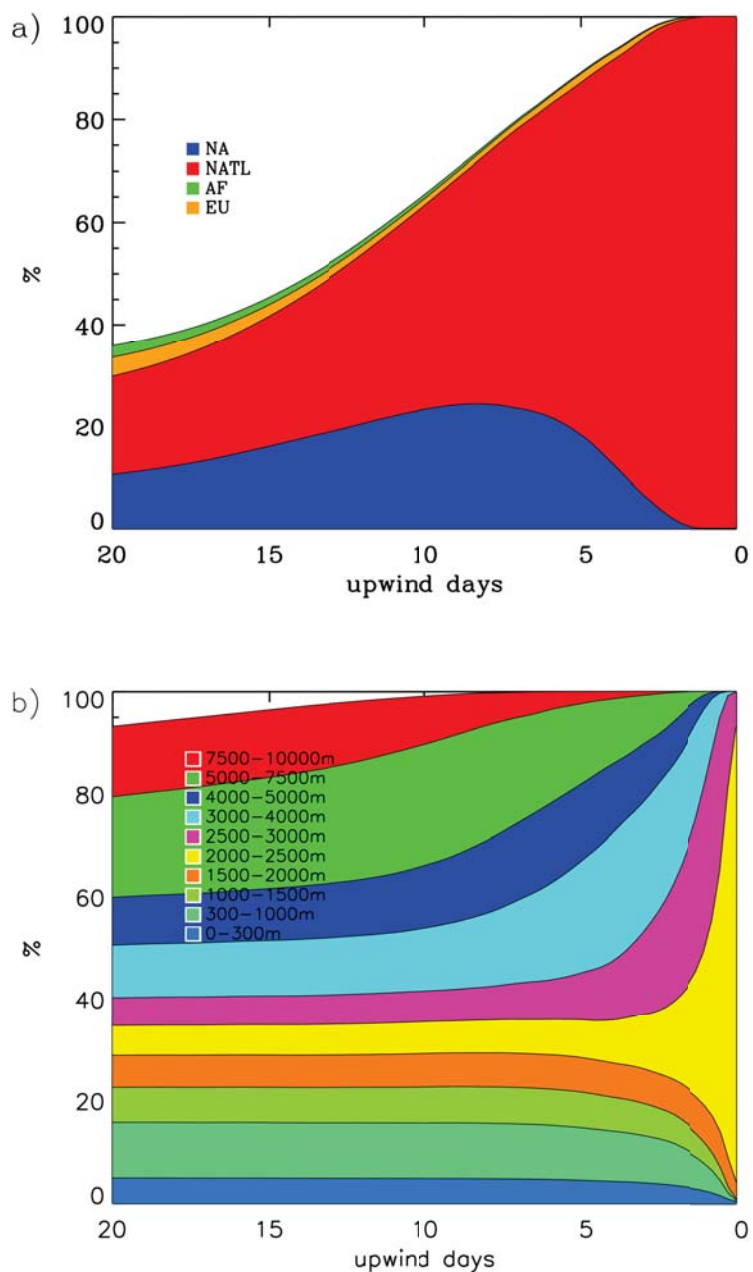


Figure 3.2: Averaged upwind residence time distribution over different geographical regions (a) and different vertical levels (%) (b) for all retroplumes simulated by FLEXPART 2010. Note that not all transport sources and heights are covered in the results, and therefore percentages total less than 100% in the upwind days.

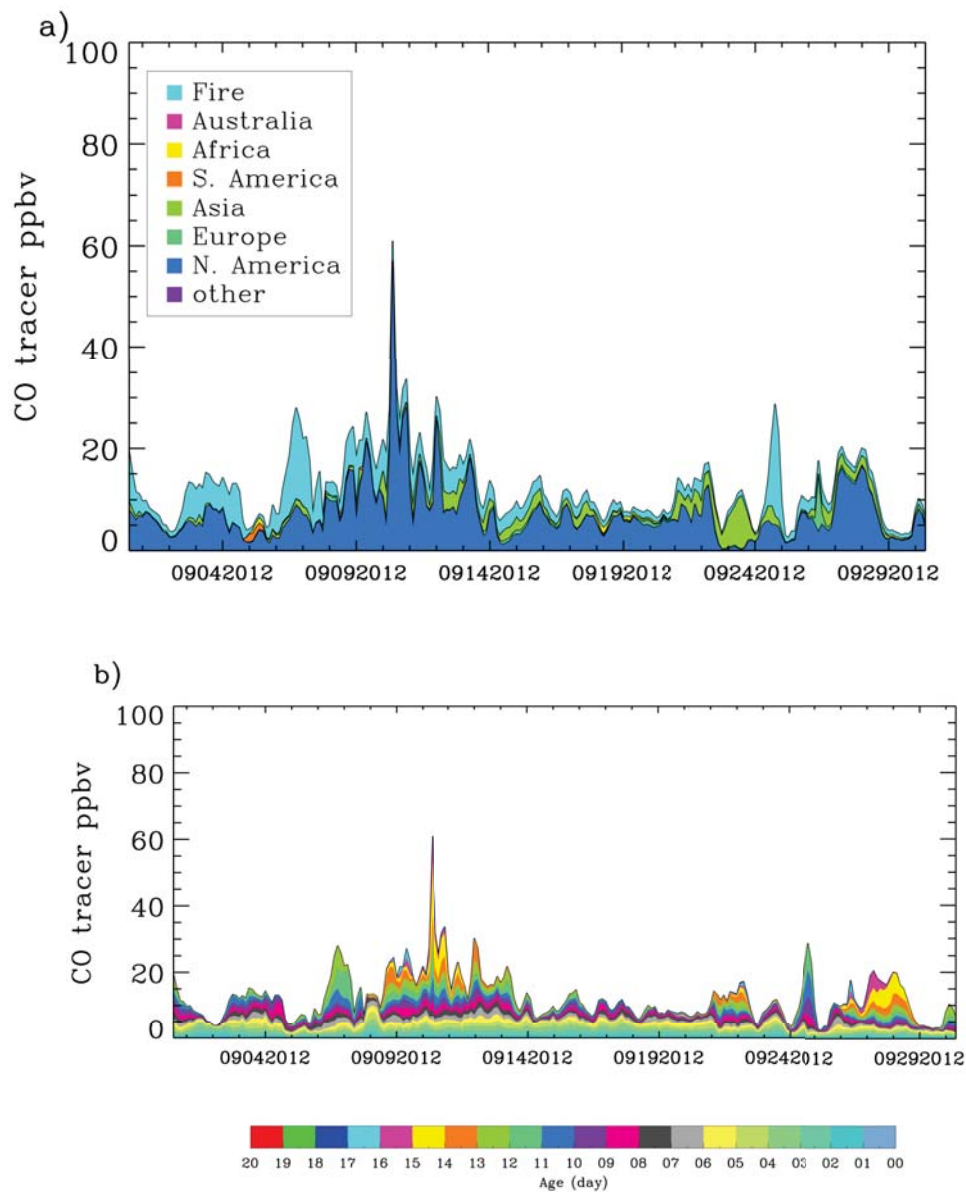


Figure 3.3: FLEXPART CO contributions from different sources (a) and FLEXPART CO ages (b) obtained by folding FLEXPART retroplumes with emission inventories. These are examples for a randomly selected month (September 2012). CO mixing ratios from different sources and age classes are added upon each other in the figure to give the total FLEXPART CO. The total FLEXPART CO is the same in the two types of analyses at a given time.

The total transport time of pollution in the atmosphere can also affect chemical composition. We calculated the air plume age by averaging the time elapsed between CO emission and arrival at PMO in the model. The estimated transport time of North American emissions to PMO was determined to be from 5-7 days (Honrath et al., 2004), so we defined the transport retroplumes that had average FLEXPART CO age less than 7 days as young transport and that were older than 10 days as aged transport. An example of the FLEXPART CO age spectra is given in Figure 3.3b.

3.2.3.3 Transport height

We considered a few scenarios of transport at different heights and changes in height during transport by quantifying the vertical RT distribution throughout the entire period for each transport (ten-year FLEXPART retroplumes). For a height reference, we extracted the depth of the marine boundary layer (MBL) from Data Assimilation System (GDAS) meteorology data over the North Atlantic for the past decade (GDAS, 2014). The MBL height in GDAS mainly ranges from 500 m – 2000 m a.s.l over the North Atlantic. Thus, we defined a “low” scenario, which has over 40% of RT within 0-2.5 km a.s.l. during transport. The constraint was applied to both the North American and the North Atlantic background transport. In order to capture the transport scenario in which air mass is lifted by deep convection or by warm conveyor belts, we defined the “lifted” transport as RT reduced by 30% in the 0-2.5 level

within 24 hours. The RT change during lifting used here refers to the findings in a 15-year climatology study of warm conveyor belts (Eckhardt et al., 2004). The last transport height scenario is “subsidence flow” or “Upper”, which brings air from upper troposphere (> 5km) or stratosphere where air compositions are different from low-middle troposphere. Retroplumes with less than 40% of its RT within 0-5 km a.s.l. between 2-12 upwind days were defined as subsidence flows having the abbreviation “Upper”. The first two days were not considered because nearly 100% of the RT was assumed to be in the 2-2.5 km level when retroplumes were close to PMO (2 225 m a.s.l.).

3.2.3.4 Potential upslope flow

Local emissions from human activities and vegetation can be carried by upslope flow to PMO, which may lead to different chemical signatures relative to free troposphere air. Upslope flow occurs through mechanically-forced lifting, in which strong synoptic winds blowing against the mountain are deflected upwards by the mountain slope where they may reach the top of Pico Mountain. Upslope flow also occurs through buoyant forcing, in which the surface air mass is lifted as a result of solar heating. Although the frequency of upslope flow was found to be less than 20% from May to September by a micrometeorological study conducted during summertime in 2004 and 2005 (Kleissl et al., 2007), we reexamined the possibilities in this study for

the ten-year period. For mechanically lifted upslope flow, the height of a dividing streamline (DSL) for the flow traveling upwards to PMO was calculated by using the method described in Sheppard (1956) and the wind speed profiles in the GFS/FNL meteorological datasets (see Appendix B). The method considers the occurrence of water vapor condensation during lifting and the following buoyant lifting caused by released latent heat. DSL heights indicate the lowest level of air that can reach the top of Pico Mountain after consumption of the mechanical energy and the latent heat (if any). If the height of DSL is below PBL height, upslope flow to PMO was considered as having occurred. We also considered strong solar heating caused by deep convection over the Island. We obtained PBL heights at PMO from GDAS, (1° Latitude 1° Longitude resolution) for the ten-year period and compared it with the height of PMO.

3.3 Transport patterns and chemical signatures

The estimated occurrence frequencies of all transport patterns are summarized in Table 1. These results are discussed together with observations of trace gas mixing ratios observations below. We only focus on the patterns with occurrence frequencies greater than 1%. The chemical signatures of trace gases determined for each transport pattern are summarized in Table 3.2. For any comparisons of the means in the following discussions, the Welch's t-test ($\alpha=0.05$) was used to determine if the

observations are significantly different from each other.

Table 3.2

Statistics of carbon monoxide (CO), ozone (O_3), nitrogen oxides (NO_x and NO_y) and NMHCs (ethane, n-propane, and n-butane) for the determined transport patterns in summer (June, July and August). The statistics are given in the form of mean \pm standard deviation (number of observations). The highest values in each row (all transport patterns) are shown in bold. Results of transport patterns, EU and AF, are not given, because they occur at a low frequency (see Fig. 3.1) and have less contributions (see Fig. 3.2)

Species	Season	NA	NATL	NA-anthro	NA-anthro-aged	NA-anthro-young	NA-anthro-lifted
CO (ppbv)	Spring	123 \pm 17(4351)	113 \pm 14(2160)	128 \pm 17(782)	121 \pm 12(630)	131\pm 17(753)	128 \pm 19(580)
	Summer	96 \pm 20(7913)	83 \pm 15(5284)	97 \pm 18(4077)	92 \pm 19(1580)	100 \pm 19(1042)	101 \pm 18(841)
	Fall	104 \pm 17(3568)	82 \pm 15(1002)	105 \pm 15(1659)	100 \pm 15(554)	111\pm 14(590)	108 \pm 14(446)
O_3 (ppbv)	Spring	48 \pm 11(4537)	39 \pm 11(2533)	49 \pm 10(2323)	47 \pm 10(996)	50 \pm 10(762)	49 \pm 10(672)
	Summer	42 \pm 13(8844)	31 \pm 11(6359)	41 \pm 12(4565)	40 \pm 14(1818)	41 \pm 12(1149)	42 \pm 12(925)
NO_x (pptv)	Spring	43 \pm 7(4253)	33 \pm 8(1201)	42 \pm 8(1928)	41 \pm 8(690)	45 \pm 7(640)	44 \pm 7(466)
	Summer	52 \pm 40(537)	22 \pm 15(299)	48 \pm 39(206)	40 \pm 41(70)	52 \pm 36(79)	50 \pm 36(64)
NO_y (pptv)	Spring	56 \pm 56(2370)	51 \pm 51(1584)	52 \pm 43(1232)	51 \pm 38(465)	56 \pm 54(297)	52 \pm 37(210)
	Fall	45 \pm 36(746)	36 \pm 30(269)	39 \pm 23(324)	33 \pm 13(160)	N.A.	40 \pm 20(90)
Ethane (pptv)	Spring	320 \pm 301(1030)	132 \pm 121(621)	344 \pm 343(470)	276 \pm 176(167)	394 \pm 381(187)	401\pm463(142)
	Summer	313 \pm 279(2439)	201 \pm 157(1651)	158 \pm 169(397)	264 \pm 172(488)	277 \pm 334(301)	314\pm296(236)
	Fall	220 \pm 142(849)	111 \pm 109(275)	205 \pm 127(352)	182 \pm 123(161)	219 \pm 137(62)	218 \pm 90(101)
n-Propane (pptv)	Spring	924 \pm 608(160)	974 \pm 368(66)	1137\pm 666(72)	1256 \pm 465(14)	966 \pm 686(31)	1040 \pm 738(24)
	Summer	657 \pm 349(359)	505 \pm 266(317)	594 \pm 324(212)	577 \pm 272(98)	516 \pm 406(41)	569 \pm 416(28)
n-Butane (pptv)	Spring	846 \pm 253(169)	681 \pm 368(74)	868 \pm 261(101)	821 \pm 253(54)	994 \pm 282(24)	899\pm 320(31)
	Summer	155 \pm 123(157)	94 \pm 57(69)	185\pm 140(71)	158 \pm 106(14)	156 \pm 115(28)	179 \pm 137(24)
n-Butane (pptv)	Spring	60 \pm 46(424)	24 \pm 28(376)	51 \pm 43(238)	42 \pm 33(109)	64 \pm 65(50)	204\pm 405(36)
	Fall	146 \pm 188(195)	90 \pm 251(98)	156 \pm 227(132)	141 \pm 292(71)	219 \pm 129(30)	38 \pm 45(23)
n-Butane (pptv)	Spring	33 \pm 36(155)	19 \pm 15(60)	44\pm 46(67)	35 \pm 23(11)	33 \pm 35(28)	9 \pm 15(18)
	Summer	60 \pm 46(424)	8 \pm 14(198)	9 \pm 9(144)	10 \pm 13(65)	8 \pm 6(26)	35 \pm 57(28)
n-Butane (pptv)	Spring	25 \pm 32(155)	20 \pm 42(49)	28 \pm 39(84)	20 \pm 42(46)	52\pm 41(20)	
	Fall						

N.A.: Not Available

Table 3.2 Continued.

Species	Season	NA-anthro-low	Fire	Fire-aged	Fire-young	Upper	Upslope
CO (ppbv)	Spring	127± 13(271)	N.A.	N.A.	N.A.	123± 11(206)	129± 13(978)
	Summer	100± 17(454)	108± 25(2296)	107± 20(885)	108± 32(538)	92± 16(655)	101± 21(793)
	Fall	N.A.	N.A.	N.A.	N.A.	96± 18(607)	96± 19(318)
O ₃ (ppbv)	Spring	44± 9(311)	N.A.	N.A.	N.A.	58± 9(329)	45± 8(1309)
	Summer	34± 17(543)	47± 13(2769)	45± 11(968)	48± 15(833)	54± 11(565)	34± 12(900)
	Fall	N.A.	42± 12(63)	N.A.	N.A.	49± 8(635)	37± 8(604)
NO _x (pptv)	Spring	N.A.	N.A.	N.A.	N.A.	63± 47(82)	47± 58(238)
	Summer	50± 36(147)	59± 35(542)	55± 30(218)	60± 44(137)	66± 65(129)	N.A.
	Fall	N.A.	N.A.	N.A.	N.A.	53± 26(112)	N.A.
NO _y (pptv)	Spring	153±180(56)	N.A.	N.A.	N.A.	271± 91(52)	137±107(261)
	Summer	157±127(147)	303±188(631)	265±152(259)	339±208(153)	234± 69(127)	84± 74(242)
	Fall	N.A.	N.A.	N.A.	N.A.	229± 85(113)	N.A.
Ethane (pptv)	Spring	N.A.	N.A.	N.A.	N.A.	930± 424(11)	1102± 453(72)
	Summer	584± 327(23)	782± 322(90)	594± 224(18)	995± 297(31)	624± 358(21)	445± 247(33)
	Fall	N.A.	N.A.	N.A.	N.A.	842± 118(54)	876± 212(59)
n-Propane (pptv)	Spring	N.A.	N.A.	N.A.	N.A.	120± 62(13)	142± 91(73)
	Summer	48± 31(34)	85± 115(141)	139± 232(30)	88± 49(40)	52± 32(30)	48± 54(36)
	Fall	N.A.	N.A.	N.A.	N.A.	120± 50(84)	144± 83(76)
n-Butane (pptv)	Spring	N.A.	N.A.	N.A.	N.A.	21± 12(11)	31± 30(71)
	Summer	11± 15(18)	14± 18(106)	16± 30(17)	16± 14(33)	6± 3(11)	44± 43(33)
	Fall	N.A.	N.A.	N.A.	N.A.	21± 15(51)	35± 27(46)

3.3.1 North Atlantic free troposphere background

Figure 3.4a shows the superimposed residence times of all the retroplumes classified as NATL for the ten-year period. The residence time of NATL in Figure 3.4a concentrates over the North Atlantic and is mostly isolated from continental emissions due to the constraints discussed in Section 2. The occurrence frequencies of NATL are 16.7%, 19.3% and 8.3% in spring, summer and fall, respectively. The highest frequency season (summer) is likely due to the strengthened Azores-Bermuda anticyclone over the North Atlantic, which restrains air convergence near the surface in the Azores regions.

We consider NATL to consist of aged air mass that has been removed from continental sources for a long time so that the chemical signatures should represent the background trace gas mixing ratios at PMO. The average observed CO during NATL periods from the ten-year record were 113, 83 and 82 ppbv for spring, summer and fall, respectively (see Table 3.2). More fossil fuel combustion during cold seasons causes increased CO in winter, which is followed by rapid decline due to accelerated oxidation by OH in spring and summer (Logan et al., 1981b). Such maxima of CO in winter and spring have been found at other remote sites (e.g., Macdonald et al. (2011)) and for the Northern Hemisphere in general (Worden et al., 2013). The average ozone was 39, 31 and 33 ppbv for spring, summer and fall, respectively. These

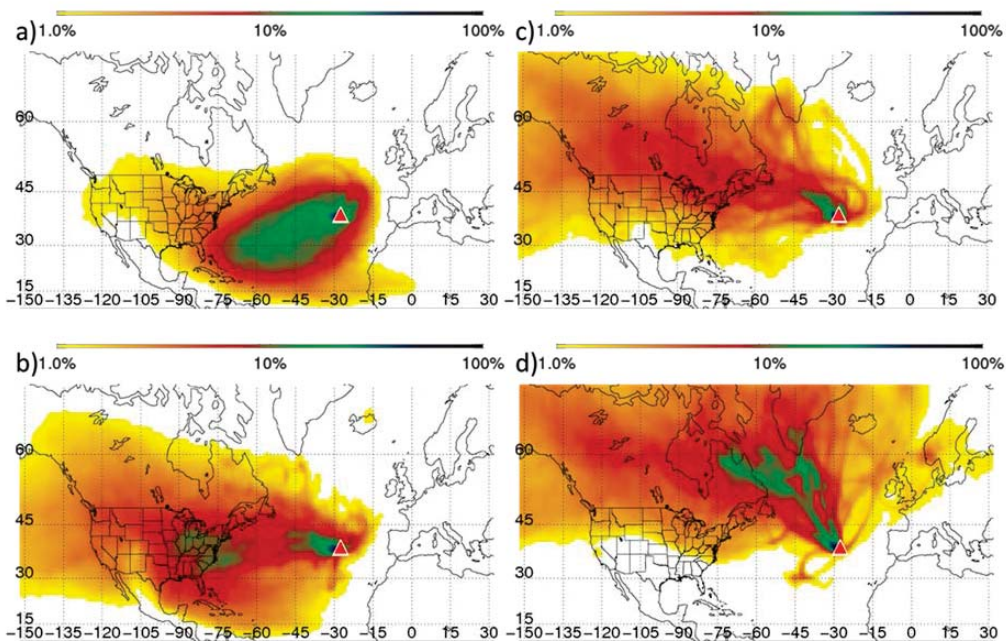


Figure 3.4: FLEXPART simulated summertime column integrated residence time for determined transport patterns for the eleven-year record (2001-2011) for a) NATL, b) NA-anthro, c) Fire and d) Upper. The color coding shows the relative abundance of relative amount of residence time. Abbreviations of transport patterns are given in Table 1.

values are similar to the previously reported ozone background at Bermuda (30-40 ppbv; Li et al. (2002a)), but lower than Eastern U.S. mean ozone in spring (47 ppbv) and summer (46 ppbv) (Cooper et al., 2012). Ozone peaks were observed at several ground sites in spring and summer (Parrish et al., 2010; Jaffe, 2010), but we did not observe summer maxima at PMO. Strong solar radiation can prompt not only ozone production but also ozone destruction. For the background ozone at PMO, stronger photochemical reactions in summer destroy ozone, however no supply of ozone precursor exists for the NATL periods because of the way we defined the NATL transport pattern. The absence of summer maxima in ozone was attributed to the

same reason in a study at Bermuda (Li et al., 2002a).

In contrast to CO and ozone, NO_x and NO_y for the NATL transport type show maxima in summer at PMO. There are two possible causes for the summertime maxima. First, deep convection is frequent in summer, which could cause lightning and NO_x production over the ocean. Second, the Azores-Bermuda anticyclone is strengthened during summer. Over the regions that are controlled by the anticyclone, downward transport could bring air masses with higher NO_x and NO_y from higher altitude. The anticyclone usually covers thousands of miles, so it may change the background NO_x and NO_y over the North Atlantic. Further analysis and modeling work needs to be done to figure out exactly how significant are the two processes in determining background NO_x and NO_y . The impact of downward transport for NATL will be discussed further related to Section 3.4.1.

3.3.2 Transport affected by North America anthropogenic emissions

The North American anthropogenic emission affected transport (“NA-anthro”) has an occurrence frequency ranging from 13.1-16.3%. The integrated RT plot for NA-anthro (Figure 3.4b) shows a clear contribution from the Boston-NY regions and a northwards curved transport pathway, which has been found in previous North

American transport events (Owen et al., 2006). In the NA-anthro subsets, lifted transport (NA-anthro-lifted) ranges from 2.5-4.0%, while the low altitude transport (NA-anthro-low) is extremely rare (1.0-3.1%), indicating long-range transport of pollution is more frequent in the free troposphere. In terms of pollution age, transport longer than 10 days (NA-anthro-aged) occurs 4.3-6.2% of the time, while transport shorter than 7 days (NA-anthro-young) ranges 4.0-6.7%.

As a primary indicator of air pollution, CO enhancement reflects the extent of pollution influence. North American anthropogenic emissions add 15 ppbv (13%), 14 ppbv (17%), and 23 ppbv (28%) of CO over the background (NATL) in spring, summer and fall, respectively (see Table 3.2). The larger enhancements in summer and fall were partly due to the low background (NATL) of CO in the two seasons. The seasonal variation in CO also corroborates the observed peaks in CO in strong radiation seasons observed in other studies (Parrish et al., 2010; Jaffe, 2010). In the NA-anthro sub-categories, CO for NA-anthro-low is statistically lower than the other three: NA-anthro-lifted, NA-anthro-young and NA-anthro-aged; however there is no significant difference among the latter three. The characteristic of NA-anthro-low is that efficient mixing occurs in the MBL. This characteristic suggests that observed CO mixing ratios are diluted by mixing with clean marine air at low altitude. Ozone enhancements for the NA-anthro transport are 10 ppbv (25%), 10 ppbv (32%) and 10 ppbv (30%) in spring, summer and fall. The seasonality of enhancement percentiles may result from the same cause, that background levels are low in summer and fall,

respectively.

Mean ozone mixing ratios in the NA-anthro sub-categories are all significantly different from each other, suggesting ozone levels are sensitive to ambient environmental conditions. Mean ozone for NA-anthro-low transport is significantly lower than NA-anthro-lifted. This implies that quick chemical consumption and deposition of ozone precursors near the surface during NA-anthro-low and potential ozone production by PAN decomposition during subsidence in NA-anthro-lifted may occur (Hudman et al., 2004; Zhang et al., 2014). This ozone production in the free troposphere has been found in other studies (Wild et al., 1996; Price et al., 2004).

Mixing ratios of NO_x and NO_y at PMO were found to be driven by transport of pollution emissions (Val Martín et al., 2008a). Summertime peaks of NO_y were linked to efficient transport of boreal wildfire emissions and pollution from eastern North America. In this study, we observed that the enhancements in NO_x and NO_y mixing ratios caused by anthropogenic emissions (NA-anthro minus NATL) actually show maxima in spring. We believe this is a result of long chemical lifetimes and stronger zonal transport during spring in the mid-latitude, as found in Macdonald et al. (2011). Among all the transport patterns, NA-anthro-lifted has the highest NO_y , potentially due to slower decomposition of PAN at higher altitude where temperature is lower. This transformation of NO_y has been studied in detail for a couple of transport events (Zhang et al., 2014). During NA-anthro-low transport, NO_y is lower than the other

transport patterns, reflecting efficient removal of NO_y in humid marine boundary layer air. The most abundant NO_y species, PAN and HNO_3 , have longer photochemical lifetimes than NO_x in the troposphere (\sim weeks), so they are formed and accumulated during transport of pollution emissions.

After the Environmental Protection Agency amended the Clean Air Act in 1990, air pollution emissions from the U.S. decreased. In order to understand the impacts of North American anthropogenic emissions in the light of the emission regulations, we provide the annual variability in trace gas enhancement (NA-anthro minus NATL) in Figure 3.5. Seasonality is not provided for this analysis because when the observations are broken into individual years, data are not adequate (data only covers 48 hours or less). Figure 3.5 shows a decrease of enhancement in CO (-0.67 ± 0.60 ppbv/yr (mean \pm 1-sigma error), p-value = 0.15) and no clear change of enhancement in ozone (-0.04 ± 0.44 ppbv/yr, p-value = 0.47). CO and ozone trends in the regions downwind of North America have been examined in many previous studies. CO decreases generally at a rate of 1%/yr globally from 2001 to 2011 according to observations of several satellites (Worden et al., 2013). Baseline trends of ozone in northern mid-latitudes were found to change from increase to decrease around the year 2000 (Parrish et al., 2012). In the eastern U.S. in spring, ozone was found to decrease at rates of -0.03 and -0.45 ppbv/year in summer (Cooper et al., 2012). Kumar et al. (2013) reported that both anthropogenic CO and NO_x emissions over the U.S. have decreased significantly since the beginning of the twenty-first century. The same study also applied a harmonic

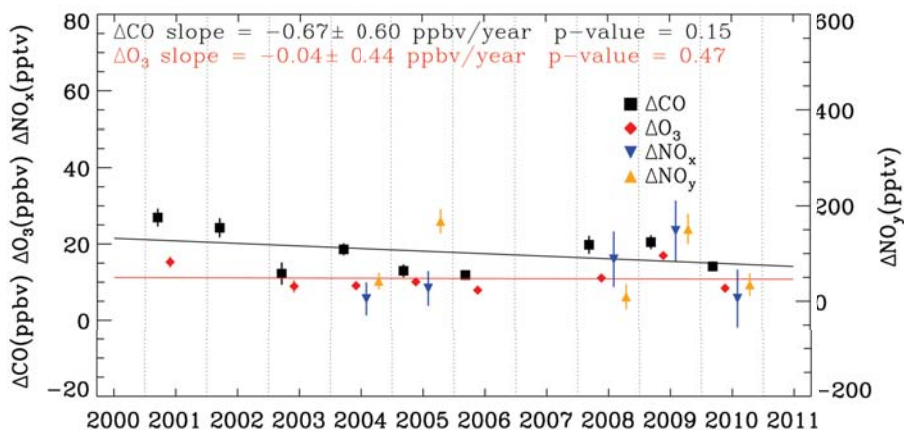


Figure 3.5: Annual variation of trace gas enhancements due to transported North American anthropogenic emission (NA-anthro minus NATL). The symbols represent the means of enhancement with vertical bars showing the 95% confidence intervals for each mean. The slopes show linear regression results for CO (black) and ozone (red) enhancements. Slope ranges and p values are also given in the figure.

regression on CO and ozone observations at PMO, which indicated decreases in CO (-0.31 ppbv/year) and ozone (-0.21 ppbv/year). They also used tagged CO tracers in GEOS-Chem to verify the influence of decline in emissions over North America. NO_x and NO_y data were missing for several of the years during the ten-year record, so the regressions for those species were not conducted.

Maxima for NMHC were found during NA-anthro transport and its subcategories in spring and fall. During young and lifted transport, NMHC were higher than for aged and low transport suggesting NMHC loss during transport due to a combination of mixing with the background and oxidation reactions.

3.3.3 Transport affected by wildfires

Wildfire emissions affected transport (Fire) occurs most frequently during the summer when there is increased wildfire activity. The frequency of Fire is 7.3% in summer, which is about half of the frequency of NA-anthro. The frequent Fire transport suggests that fire emissions may act as a competing air pollution source to anthropogenic emissions, and it usually causes drastic changes in pollution levels at PMO. Because wildfires occur more often in the boreal regions, the integrated RT (Figure 3.4c) shows pathways from Canada and the northern U.S. that clearly differ from NA-anthro (Figure 3.4b).

Boreal wildfires have been found to emit more CO due to intensive combustion and to suppression of ozone production in early stages following emission of heavy loading aerosols (Parrington et al., 2013). As shown in Table 3.2, the Fire transport pattern shows an averaged CO mixing ratio of 108 ppbv, which adds 25 ppbv (30%) to the background (83 ppbv for NATL). The average CO for wildfire impacted transport was the 139 ppbv reported by Val Martín et al. (2006), in which a higher CO cutoff value (110 ppbv) was used for determining fire events in 2004. In a later study, Val Martín et al. (2008a) found mean CO of 124 ppbv and 105 ppbv, respectively, for fire affected periods in 2004 and 2005 at PMO using 75th percentiles of the FLEXPART CO from fire as the cutoff. These differences in mean CO for fire events noted by Val Martín

et al. (2006), Val Martín et al. (2008a) and this study are likely due to different choices of CO cutoffs used for event identification. In this study, we compared the standard deviation of observed CO to FLEXPART CO from fire (as in Section 3.3.2), which is more appropriate for quantification of fire impacts in a climatology study like this. Having different cutoffs in each year may be more accurate for identification of events in individual years. The enhancement of ozone due to Fire (16 ppbv, 50%) is also stronger than that caused by NA-anthro (10 ppbv, 32%).

Although wildfires were found to be less efficient for NO_x production than fossil fuel combustion due to lower flame temperature (Jaffe and Wigder, 2012), the vegetation fuel nitrogen can also lead to high NO_x mixing ratios in fire plumes. The mixing ratios of NO_x and NO_y for Fire are higher than the marine background, NATL, by 9 pptv and 138 pptv respectively, and these enhancements are in agreement with the values (9-30 pptv for NO_x and 117-175 pptv for NO_y) in a study focusing on boreal wildfire impacts (Val Martín et al., 2008a). Alvarado et al. (2010) observed that 40% of the initial NO_x emissions were converted to PAN in a few hours in boreal biomass burning through aircraft measurements, which could promote long-range transport of NO_y .

3.3.4 Transport from the upper troposphere and stratosphere

Subsidence flow from upper free troposphere and stratosphere (“Upper”) has frequencies of 2.1- 4.1%, with the highest frequency in fall. The fall maxima is likely caused by stratosphere-troposphere-exchange (STE) in the regions between polar and middle latitude, which shifts southward in winter (Holton et al., 1995). The “Upper” pattern mainly originates in the north and extends to the polar regions, as shown in Figure 3.4d.

The Upper transport pattern has mean CO mixing ratios of 123, 93 and 96 ppbv for spring, summer and fall, respectively (see Table 3.2), which are ~ 10 ppbv higher than CO mixing ratios during NATL. Usually, CO has no large sources at high altitude and has been found to be trapped at the lower troposphere (Liang et al., 2011). However, two potential reasons may lead to CO enhancement during this transport pattern. When comparing the air mass origins of the two transport patterns, Upper and NATL, in Figure 3.4a and 3.4d, the superimposed residence time of Upper shows air mass origins over the Arctic regions, while NATL is mainly from middle and low latitude regions. Due to the long lifetime of CO in the high latitude regions, air masses from the north contain higher CO than NATL. In addition, the superimposed residence time of Upper (Figure 3.4d) covers the whole boreal North American region, so the

Upper can also receive some CO from wildfires from that area (but not enough to be classified as Fire). Despite the potential sources, CO mixing ratios observed during Upper are a few ppbv lower than NA-anthro and Fire.

The Upper transport has mean ozone mixing ratios of 58, 54, and 49 ppbv, which are the highest ozone observed for spring, summer and fall, respectively. Mean ozone mixing ratios are ~ 20 ppbv higher than NATL in all seasons, because of the naturally high ozone in the upper troposphere and stratosphere. Ozone enhancement caused by downward transport has been widely found in other studies (e.g., Logan, 1999; Neuman et al., 2012). At Mount Washington, New Hampshire, U.S., downward transport has been found to contribute 5% of ozone events, which was associated with atmospheric anticyclones (Fischer et al., 2004). The debate on stratospheric influence versus tropospheric production as the major source of tropospheric ozone has existed for years (Li et al., 2002b). In this study, we found that downward transport caused the highest ozone in the observation record at PMO, but this may not necessarily suggest the total ozone contribution from high altitude is greater than the contributions from pollution emissions on a long-term basis. The occurrence frequencies of Upper (2.1%, 2.3% and 4.1%) are much lower than NA-anthro (16.3%, 15.1% and 13.1%).

Upper has the highest NO_x mixing ratios in all seasons. The mean NO_x mixing ratios are 63, 66 and 53 pptv in spring, summer and fall, respectively, which are about

15-41 pptv higher than NATL. NO_x are produced in the stratosphere and upper troposphere due to intense photochemical oxidation of N_2O , which is emitted globally from soil. The observed high NO_x during Upper aligns with the findings during STE (stratosphere-troposphere-exchange; Liang et al. (2011)), in which NO_x mixing ratios were found to be 50-85 pptv higher than the background Arctic troposphere. The mean NO_y mixing ratios are 271, 234 and 229 pptv in spring, summer and fall, respectively, which are all higher than NO_y during NATL. The elevated NO_y during downward transport has been attributed to accelerated ethane degradation followed by formation of PAN in stratosphere-troposphere air mass exchange (Liang et al., 2011).

3.3.5 Transport affected by upslope flow

Upslope flow occurred 3.5-8.2% of the time, with lowest frequency in summer. This seasonality is in agreement with the previous meteorological study at PMO but with lower frequencies than the estimated upslope flow during 2004-2005 (4.2-37 %; Kleissl et al. (2007)). Upslope mainly shows signatures of local emissions. Upslope CO and ozone are statistically higher than NATL. This indicates upslope transport of local anthropogenic emissions to PMO. Upslope has the lowest NO_y , which may be due to efficient wet removal of the NO_y by cloud condensation during lifting, which was

predicted to take place for 30% of the entire upslope flow. The mixing ratio of n-butane is found to be about four times higher than the ocean background, which might be anticipated because of the local usage of butane as a primary fuel on the island.

3.4 Relationships among observed trace gases

Trace gases undergo photolysis and oxidation reactions with OH in the troposphere. Due to the differences in chemistry mechanisms and reaction rates in the atmosphere, concentrations of trace gases change differently with time in long-range transport, which leads to variations in correlations of simultaneously observed trace gases at PMO. The observed correlations reflect the historical behaviors of the trace gases during long-range transport. For example, CO is mainly oxidized by OH and decays slowly (lifetime of a few months) in the troposphere, while ozone has a lifetime of a few weeks. In the time frame of transport from North America to PMO (5-7 days), CO can be considered as chemically inert and the observed correlation of ozone with CO reflects the ozone production tendency (Parrish et al., 1993). Light NMHC (C₂-C₅) also mainly undergo OH oxidation and mixing with clean background air in the troposphere. Due to the size and structure differences, NMHC decay at different rates. By examining the ratios between NMHC and comparing with the initial ratios, the photochemical age of the air mass can be estimated (McKeen and Liu, 1993).

In the presence of chlorine atoms (Cl) in the atmosphere, oxidation with Cl is a potential decay pathway for NMHC which has been found to be faster for n-isomers as compared to iso-isomers. For example, butane isomer ratios were found to be affected by oxidation by chlorine atoms (Hopkins et al., 2002). Oceanic chlorine atom has been found to affect NMHC observations at Mt Wilson in the Los Angeles Basin during the time periods when wind blows from the Pacific. In the following section, we examine correlations of tracer gases to study photochemical processes for differing transport patterns.

3.4.1 $d[O_3]/d[CO]$

The value $d[O_3]/d[CO]$ has been found to be different in the downwind regions (over oceans) of emissions compared to observations at continental sites. The value $d[O_3]/d[CO]$ has been reported to be fairly consistent (0.20-0.37) in the rural sites of eastern U.S., which reflects a combination of aging processes of air pollutants and mixing with remote clean air mass during transport (Chin et al., 1994; Parrish et al., 1998; Mao and Talbot, 2004). However, the slope can vary in different scenarios. Hegarty et al. (2009), using Tropospheric Emission Spectrometer retrievals, reported a spring slope value of 0.13 in the free troposphere over the mid latitude regions extending from North America to the North Atlantic. Interestingly, further into the North Atlantic ocean, (Cooper et al., 2001b) higher slopes (close to 1.0) were found

at PMO (Honrath et al., 2004) and Mountain Izana, Canary Islands (Cuevas et al., 2013). The high ratios in regions downwind of emissions potentially indicates photochemical evolution of pollution in such regions. Negative slopes were found during winter at ground sites (Parrish et al., 1998; Macdonald et al., 2011), which was attributed to titration of ozone by NO in emissions. A negative slope was also found in cases of strong vertical mixing, which brought air mass from the upper troposphere (Fishman and Seiler, 1983).

In Figures 3.6-3.8, we present the observations $d[\text{O}_3]/d[\text{CO}]$ grouped for the three main transport patterns, NATL, Fire and NA-anthro, in spring, summer and fall, respectively. In the figures, we include only continuously observed events with duration periods longer than 12 hours. The distribution of observed data in different transport patterns show the same pattern in all seasons (from lower left to upper right), reflecting the increases in pollution levels from NATL to NA-anthro, and to Fire. $d[\text{O}_3]/d[\text{CO}]$ values for NA-anthro found in all seasons (spring 0.59, summer 0.71 and fall 0.45, see Figures 3.6-3.8) are lower than the values found in specific events with slopes around 1.0 (Honrath et al., 2004; Zhang et al., 2014). The lower slopes for NA-anthro probably occur because the data used in the regressions do not isolate direct and fast transport events from North America, so the ozone enhancement should be less intensive than in the previous case studies.

Photochemical sinks of ozone cause a decrease of the slope, while mixing with

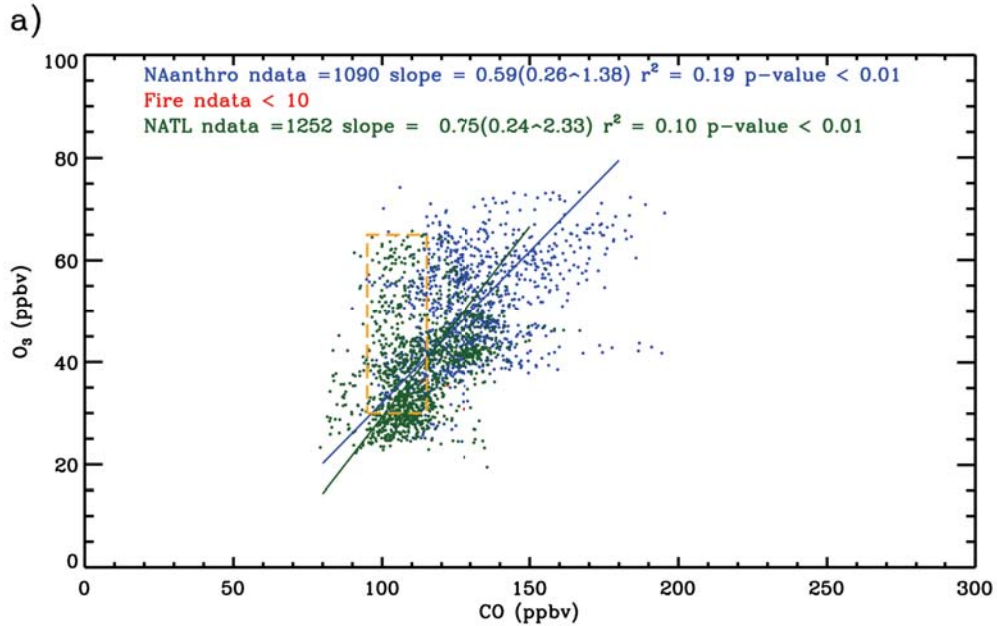


Figure 3.6: RMA regression results of observed ozone and CO relationship for transport patterns NA-anthro, Fire and NATL in spring. Continuous observations longer than 12 hour were used. For the Fire transport pattern in fall, all observations were used. The gold dotted boxes show the wide ozone ranges at the lower end of CO for the NATL transport pattern, which is responsible for increasing $d[O_3]/d[CO]$.

background air from different sources reduces the correlation coefficient, r . Low $d[O_3]/d[CO]$ values were found for “Fire” (slopes of 0.31 for summer and 0.12 for fall), because of the large amount of CO produced in biomass burning and lower NO_x/CO emission ratios in boreal fires compared to anthropogenic sources (McKeen et al., 2002; Lapina et al., 2006). Production of O_3 and NO_2 has been found to be suppressed in fire plumes due to reduction of sunlight transmission by aerosols (Real et al., 2007; Verma et al., 2009; Parrington et al., 2013). This variation in $d[O_3]/d[CO]$ in fire affected patterns is consistent with a previous MOZART study for observations

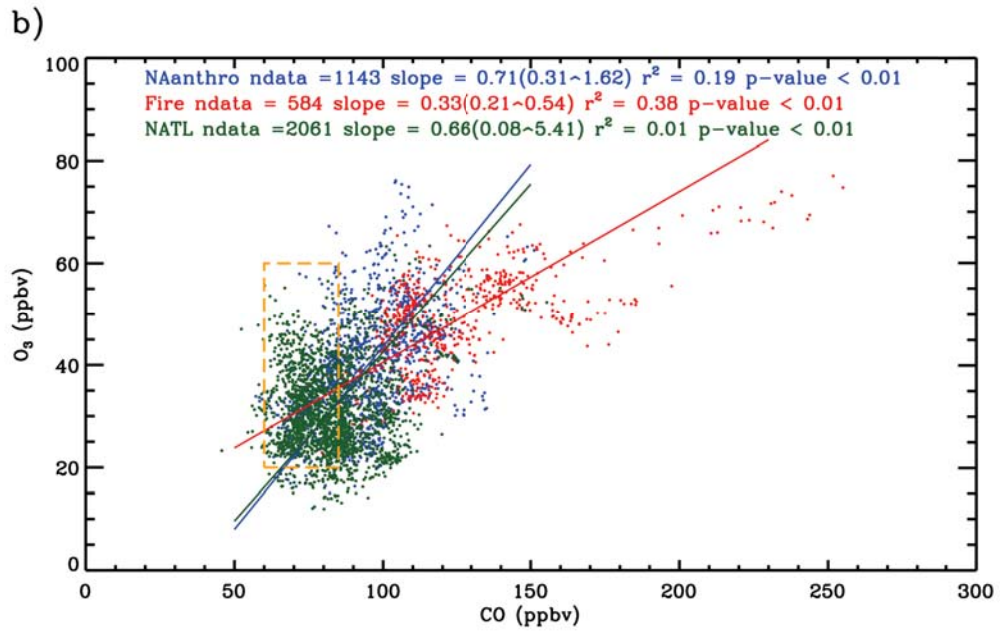


Figure 3.7: Same as Figure 3.6, but for summer.

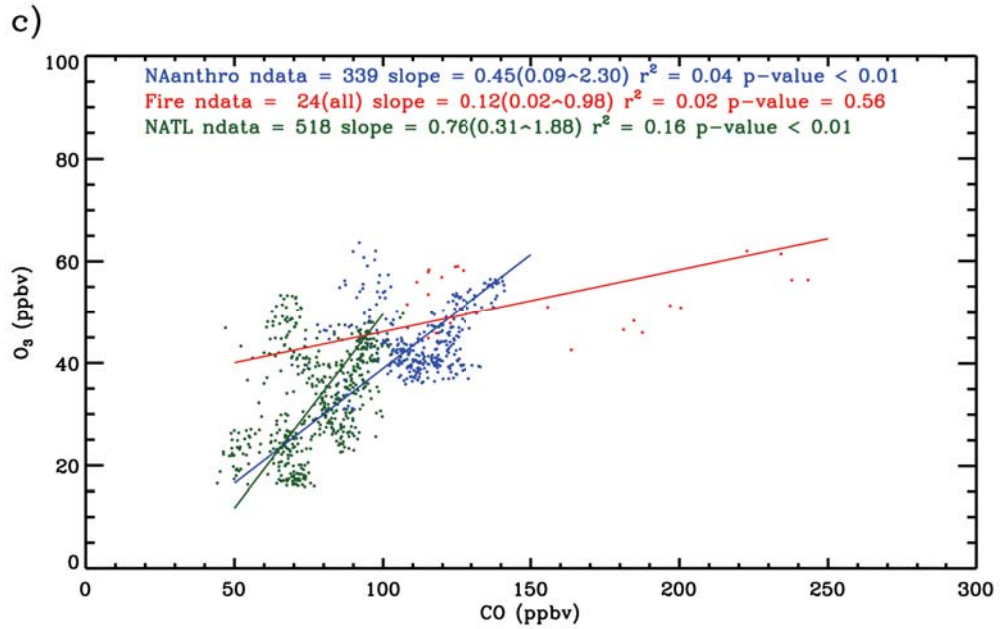


Figure 3.8: Same as Figure 3.6, but for fall.

at PMO (Pfister et al., 2006) in which lower values $d[\text{O}_3]/d[\text{CO}]$ were found in cases with higher relative contribution of fire tracer.

Interestingly, the slopes for NATL are higher than NA-anthro in spring and fall. In both seasons, high ozone mixing ratios (greater than 50 ppbv) were observed for NATL. For all NATL transport cases, we found the average RT ratio from high altitude ($>5\text{km}$) was $\sim 9\%$. The downward mixing of ozone-rich air masses from higher altitude is likely be responsible for the occasionally high ozone during the periods when NATL was observed. The data circled by gold dotted lines in Figure 3a) and 3b) show wide ozone distributions in a narrow CO window. These data deviate from the slope and potentially have a greater effect on the slope. Positive $d[\text{O}_3]/d[\text{CO}]$ in stratospheric intrusion was observed by Kim et al. (2013), in which they used GEOS-Chem to interpret global satellite observations of $d[\text{O}_3]/d[\text{CO}]$.

3.4.2 Oxidation of butane isomers

Figures 3.9-3.11 show the observed ratio of $[\text{i-butane}]/[\text{n-butane}]$ as a function of $[\text{n-butane}]$ in spring, summer and fall respectively. In each panel, all data are shown in small black dots with observations for specific transport patterns in each season indicated with different colors. The average values (center of the cross) and standard deviations (bars) are also given for each transport pattern. Mixing ratios of

n-butane are given in a logarithmic axis to better display the wide range in mixing ratios. In spring and fall, most observed n-butane mixing ratios are above 10 pptv. The [i-butane]/[n-butane] values towards the left show a more scattered distribution because of low precision of measurement towards the detection limit. The average [i-butane]/[n-butane] values range from 0.5-1.0, suggesting faster aging of i-butane due to its being more easily attacked by OH than n-butane. Oceanic Cl atom has been found to cause faster oxidation of n-isomers in Arctic marine air (Hopkins et al., 2002). However, similar values of [i-butane]/[n-butane] were found in lifted and low transport, suggesting that potential oceanic Cl atom does not influence NMHC during transport to PMO. These results are in agreement with those of Helmig et al. (2008), who observed that i-butane and n-butane in 2004 and 2005 were closely correlated, suggesting butane isomers have similar aging processes during transport to PMO.

3.4.3 NMHC photochemical clock

The relationship between logarithmic hydrocarbon pairs can be used to identify pollution plume aging and mixing processes (Parrish et al., 2007), because the ratio of logarithmic hydrocarbon pairs (i.e., $(\ln [\text{n-butane}]/[\text{ethane}]) / (\ln [\text{propane}]/[\text{ethane}])$) is a function of the kinetic reaction rates against OH only. If only mixing has an effect, the ratio would be aged to a background value (Helmig et al., 2008). This ratio is particularly useful for studying NMHC aging during long range transport in

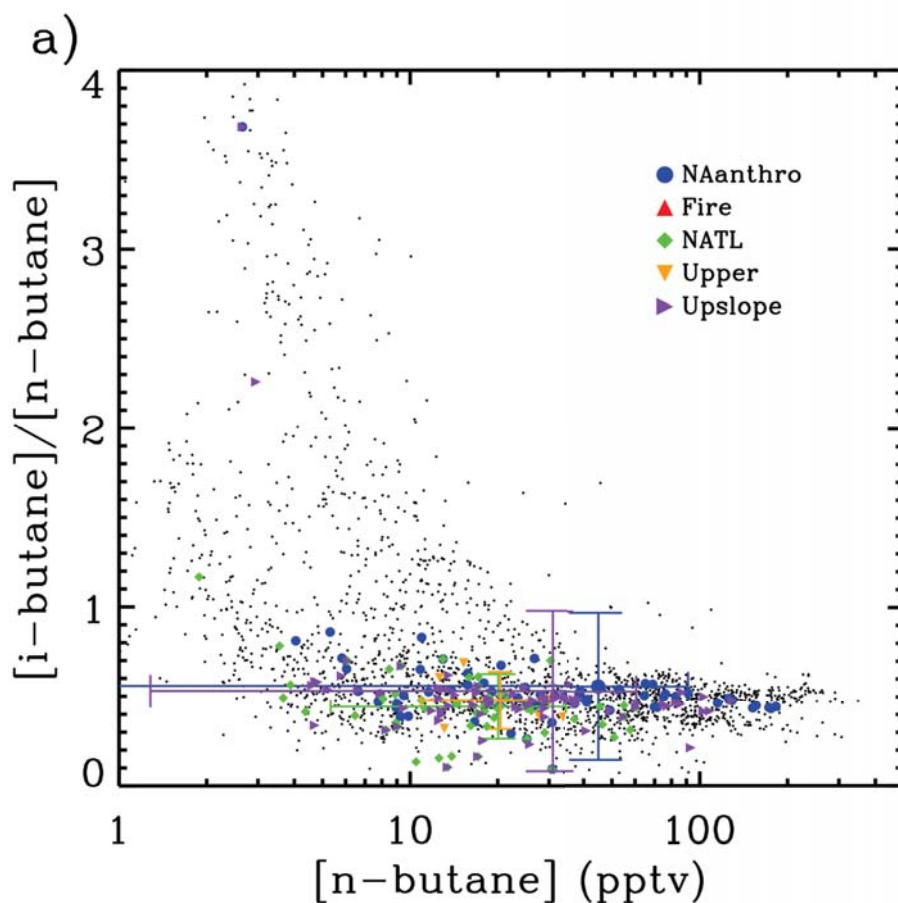


Figure 3.9: Butane isomers observed for frequent transport patterns in spring. The black dots show the data for all available measurement, including all seasons, all defined transport patterns and also data that do not belong to any defined transport patterns. Observations for different transport patterns are color coded. Intersecting lines indicate the standard deviations for the mean of each transport pattern.

which there is no significant source of NMHC during transport (McKeen and Liu, 1993).

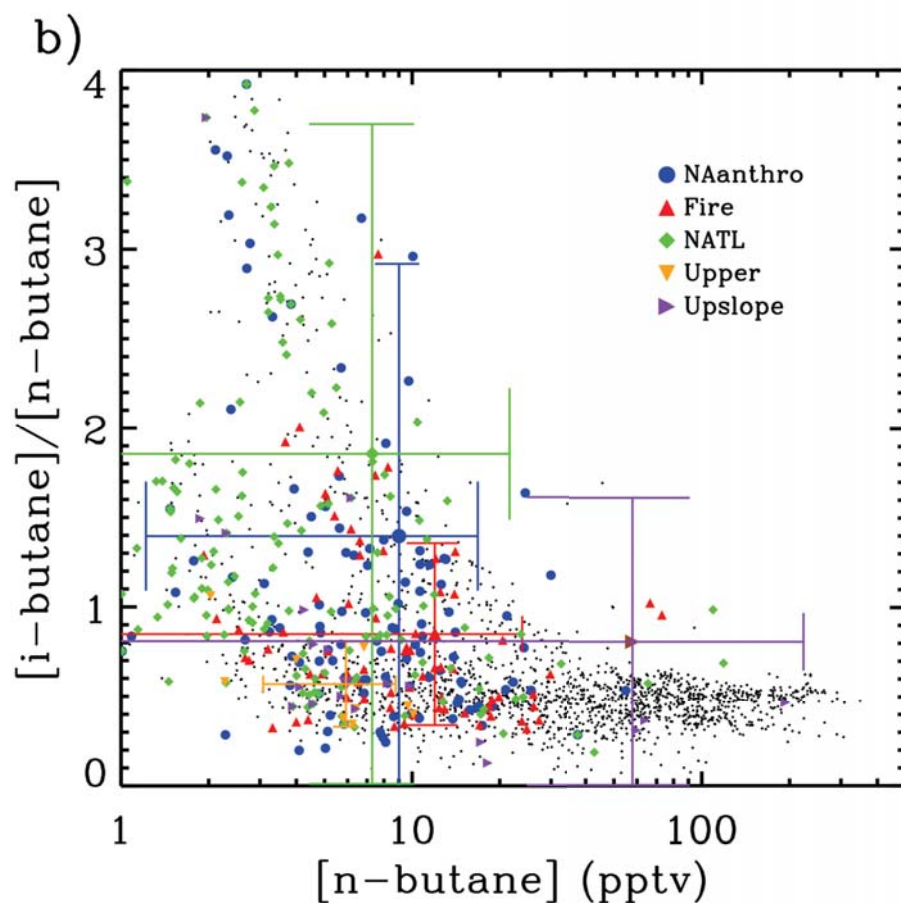


Figure 3.10: Same as Figure 3.9, but for summer.

The $\ln[n\text{-butane}]/[\text{ethane}]$ vs. $\ln[\text{propane}]/[\text{ethane}]$ ratios for different transport patterns are shown in Figures 3.12-3.14. The kinetic scenario is displayed by a solid line, and the slope and aging scale are calculated by using the same kinetic reactions rates as in Helmig et al. (2008) and an assumed constant $[\text{OH}]$ of $1.0 \times 10^6 \text{ molecule}/\text{cm}^3$. The same aging scale is used in all seasons in order to observe seasonal variations.

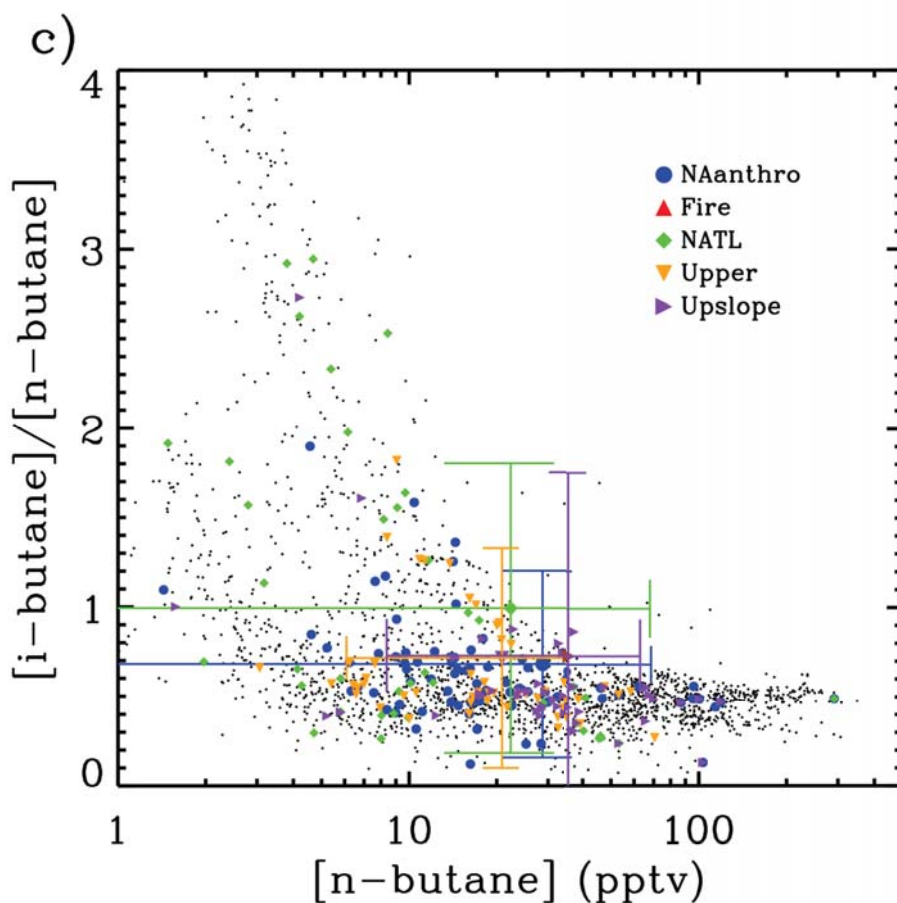


Figure 3.11: Same as Figure 3.9, but for fall.

It was found that the OH concentration in the troposphere of North mid-latitude is higher in spring than in summer and fall (Spivakovsky et al., 1990); therefore the actual photochemical ages can be expected to be longer than shown in Figure 3.12. The initial point is the same for the kinetic and mixing lines, and it is defined by the NMHC ratios in continental emissions derived in Helmig et al. (2008). Data for

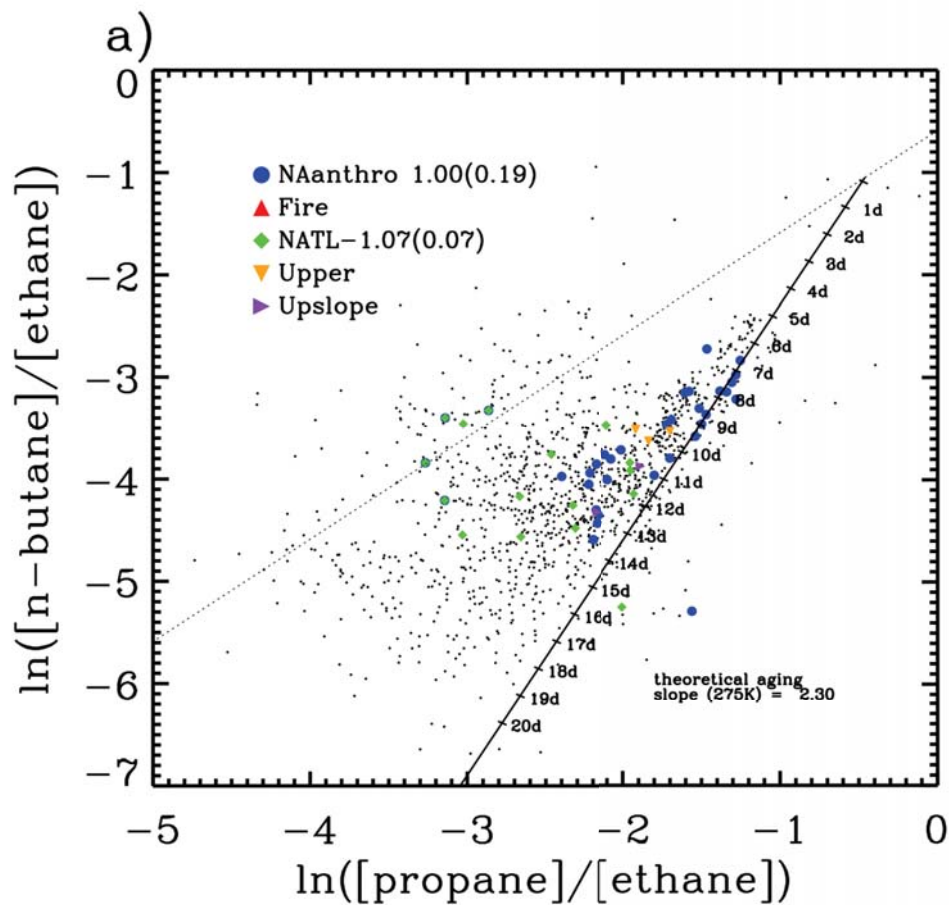


Figure 3.12: Relationships between $\ln([n\text{-butane}]/[\text{ethane}])$ and $\ln([propane]/[\text{ethane}])$ for the frequent transport patterns in spring. The dotted line shows the mixing-only trend initiated from an assumed origin based on NMHC ratios in emission. The solid line shows the photochemical decay slope from the same origin for a fixed $[OH]$. The black dots show the data for all available measurement, including all seasons, all defined transport patterns and also data that do not belong to any defined transport patterns. The method to compute the slopes are discussed in the text. The legends provide linear regression slopes, and, in parentheses, 1-sigma errors for the transport patterns.

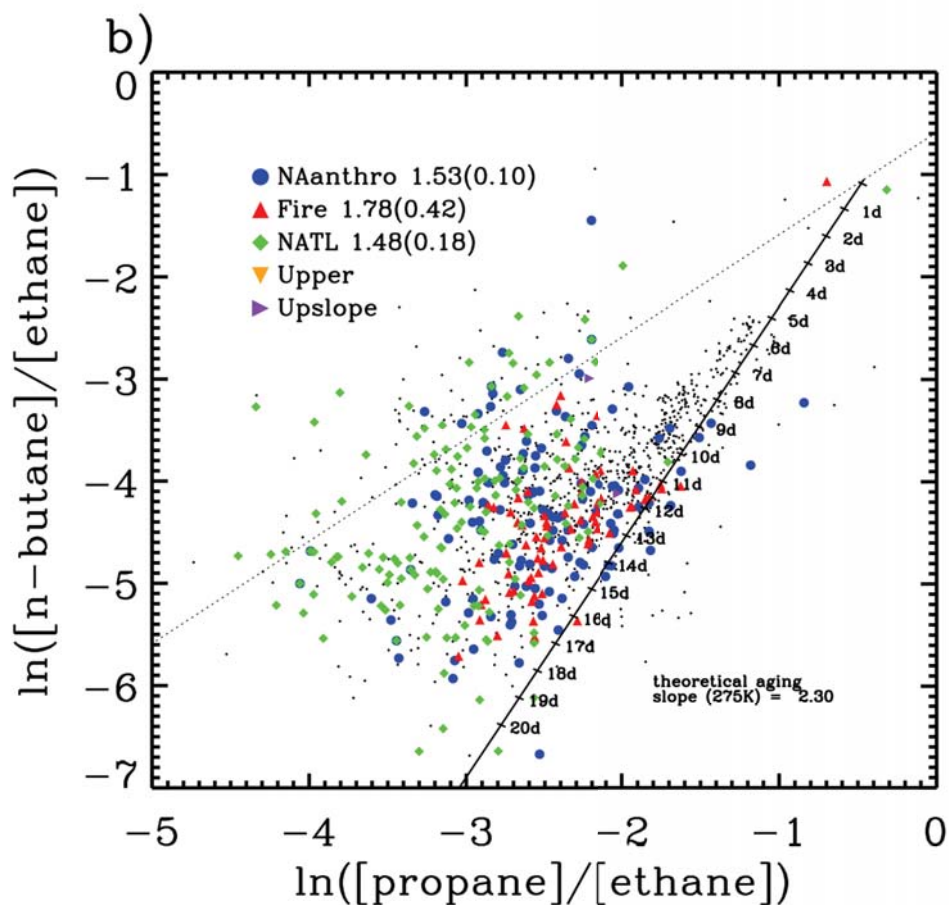


Figure 3.13: Same as Figure 3.12, but for summer.

the defined transport patterns are indicated in different colors. Comparing the data distribution in the three seasons, the data observed in summer are farther down the kinetic line indicating more oxidation. Because of the difference in mixing extent, the data for NA-anthro are closer to the kinetic line (less mixing) in spring and fall,

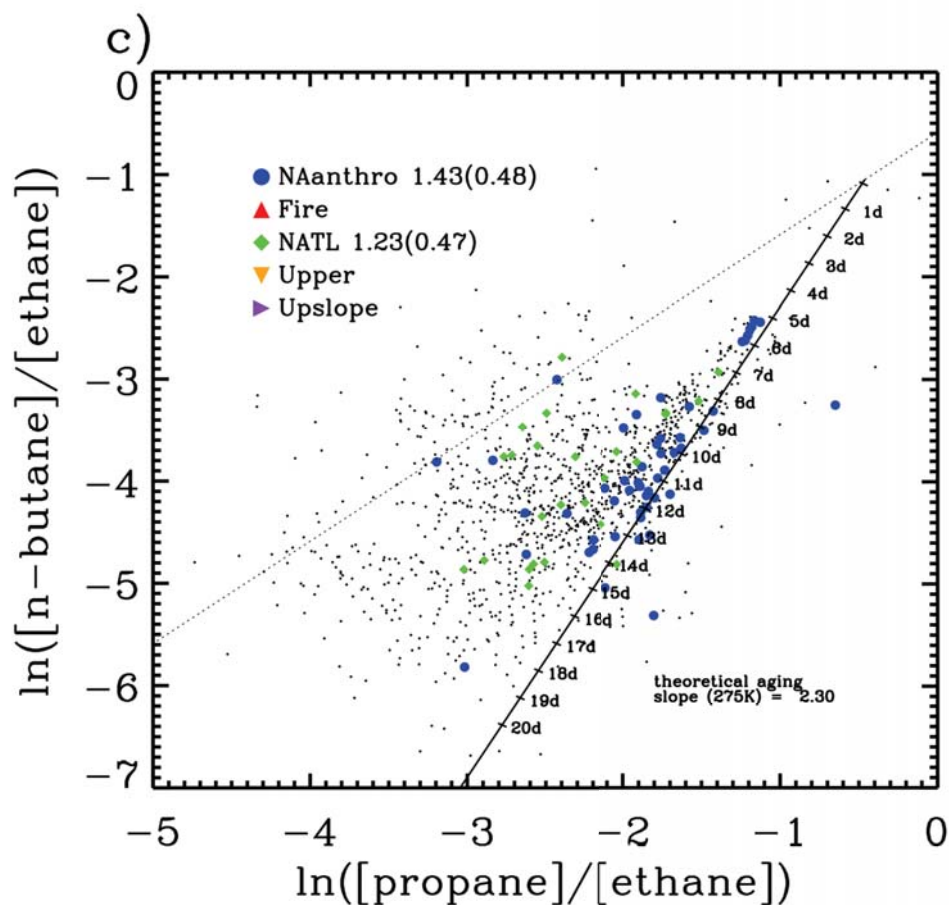


Figure 3.14: Same as Figure 3.12, but for fall.

whereas NATL data are spread and close the mixing line. According to the theoretical decay in oxidation reactions with OH, the air mass ages at PMO ranges from 7 to more than 20 days (with a mean of 17 day and a standard deviation of 5 days). This estimated age range is greater than that found in previous studies at PMO of 5-7 days using FLEXPART modeling (Honrath et al., 2004; Zhang et al., 2014). These

previous studies focused on direct transport events rather than all kinds of transport in general. The seasonality of OH would change the estimated photochemical ages. RMA regression slopes and R^2 are also shown in the Figure 3.12–3.14. Except for the negative slope obtained for NATL as a result of very few observations, the regression slopes range from 1.00 to 1.81, which are consistent with observations in previous studies (Parrish et al., 2007; Helmig et al., 2008).

3.5 Conclusions

We used FLEXPART simulations, CO emission inventories and meteorological conditions to categorize the most frequent transport patterns for 2001 to 2010. In the classification of transport patterns, the factors that may change air mass compositions were considered including emission sources, atmospheric RT, transport height and upslope flow.

Trace gas concentrations at PMO were found to be driven by both pollution emissions and natural sources. CO mixing ratios, which are frequently used as a pollution tracer, are driven mainly by continental emissions. Transport time and the emission sources are the main factors controlling CO, and differences in environmental conditions do not affect CO concentrations during transport. Anthropogenic emissions contribute

an additional 14–23 ppbv (13%-28%) CO and \sim 10 ppbv (25%-30%) ozone to background levels at PMO. Summertime wildfires cause even more pollution (25 ppbv (30%) CO and 16 ppbv (45%) of ozone). Transport from the upper troposphere has substantial impacts on CO, ozone and nitrogen oxides levels. The ozone enhancement caused by downward mixing was about two times the enhancement caused by North American anthropogenic emissions. The “Upper” transport pattern also causes CO enhancement at PMO, which was likely due to potential sources from wildfire emissions and transport from high latitude. Besides air mass origin, transport height can also change PMO air composition. NO_x can be converted to stable PAN during lifting of air pollution plumes, which leads to ozone production thousands of miles away from the source regions. Nitrogen oxides show strong evidence of impacts from continental pollution emissions, but they are more vulnerable to deposition processes and show varying concentrations for different transport heights and meteorological conditions.

The ratio $d[\text{O}_3]/d[\text{CO}]$ has been used as an indicator of ozone production tendency, but this slope may not reflect ozone chemistry only. For example, the values of $d[\text{O}_3]/d[\text{CO}]$ (0.12-0.33) for Fire were lower than those for NA-anthro and NATL, which could be due to a much larger magnitude of CO emission from wildfires. Furthermore, the high $d[\text{O}_3]/d[\text{CO}]$ values for the NATL transport pattern (0.66-0.75) could be a distinct characteristic of the free troposphere over the central North Atlantic. The NATL was found to be mixed with air masses from altitude above 5

km due to the persistent Azores-Bermuda anticyclone. The mixing of ozone-rich air masses may create variable ozone within a narrow CO range, which leads to the high ratios of $d[\text{O}_3]/d[\text{CO}]$.

Mixing ratios of the light NMHC at PMO are driven mainly driven by pollution sources. The ratios of butane isomers in transport close to the surface are not significantly different among transport patterns, so NMHC during transport to PMO is not likely affected by Cl atom emitted from the ocean. We also observed high butane during periods when upslope flow occurred. This is because butane is widely used as a fuel on the Island. The photochemical ages indicated by the NMHC photochemical clock (7-20 days) are generally in agreement with the understanding of transport time from North America to PMO.

Chapter 4

Ages and sources of aerosol ^{210}Po collected in the free troposphere over the central North Atlantic¹

¹This chapter is based based on material that is intended for publication as Zhang et al., Ages and sources of aerosol ^{210}Po collected in the free troposphere over the central North Atlantic

4.1 Introduction

Atmospheric radionuclides can be used as indicators of aerosol ages (e.i., how long the collected aerosol has been in the atmosphere), because radionuclides attach to aerosol particles and undergo radioactive decay. ^{222}Rn is an inert noble gas that is emitted constantly from the Earth's crust in the decay chain of ^{238}U (Turekian et al., 1977). ^{222}Rn has a radioactive half-life of 3.8 days, and it is not removed by atmospheric physical and chemical processes. ^{222}Rn daughters have been used indicators of aerosol sources and deposition in the atmosphere (Liu et al., 2001). The first generation daughter, ^{218}Po , attaches to fine aerosols particles in a time range of 40 s – 3 min mainly in the atmosphere over continental regions (Whittlestone, 1990). The progenies of the next generations are produced on the aerosols and have different radioactive half-lives. They are removed from the atmosphere via dry and wet deposition along with the carrier aerosol. ^{210}Pb ($t_{1/2} = 22.1$ years) and ^{210}Po ($t_{1/2} = 138$ days) are the only two long-lived daughters of ^{222}Rn (Fig. 4.1), so they are more easily to be quantified than the other progenies. After being produced on carrier aerosols, the activity ratio of the two radionuclides has been found to follow a function of time as shown by Eq. 4.1 (Nevissi, 1991).

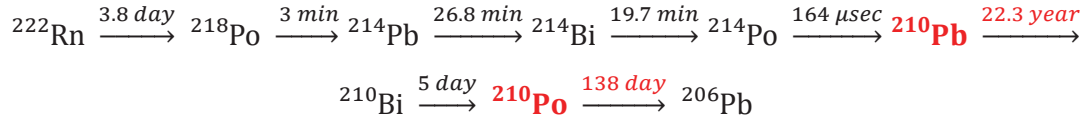


Figure 4.1: Decay chain of ^{222}Rn and radioactive half-lives of its progeny

$$\frac{A_{^{210}\text{Po}}}{A_{^{210}\text{Pb}}} = 1 + 0.0374e^{(-0.139t)} - 1.037e^{(-0.005t)}, \quad (4.1)$$

where $A_{^{210}\text{Po}}$ and $A_{^{210}\text{Pb}}$ are activities of ^{210}Po and ^{210}Pb , and t is the estimated aerosol age. The disequilibrium equation is only applicable for ^{210}Po and ^{210}Pb produced in the decay chain of ^{222}Rn in the atmosphere (i.e., no parent isotopes of ^{222}Rn are present in the aerosol and no secular equilibrium exists between such ancestors and either ^{210}Pb or ^{210}Po). Re-suspended aerosol particles that are rich in aged ^{210}Pb or ^{210}Po exhibit secular equilibrium among this isotope's progeny. If the re-suspended ^{210}Pb and ^{210}Po attach to aerosols in the atmosphere, the estimated age would be biased by the aged terrigenous ^{210}Pb and ^{210}Po . If there are no terrigenous radionuclides on the aerosols, the decay in Eq. 4.1 can be used to estimate aerosol age.

The activity ratio of ^{210}Po and ^{210}Pb has been widely used to estimate aerosol age in different scenarios. McNeary and Baskaran (2007) measured $^{210}\text{Po}/^{210}\text{Pb}$ in bulk

precipitation, dry fallout and aerosol samples, and the associated ages were observed to be 15, 75 and 24 days. Using the same method, Długosz et al. (2010) reported that aerosol ages ranged from 7 to 120 days at Lodz, Poland during winter and spring 2008-2009. The ratio of $^{210}\text{Po}/^{210}\text{Pb}$ in volcanic eruptions was found to be large (Lambert et al., 1985), and it was estimated to be in secular equilibrium (~ 1 ; Baskaran (2011)). Atmospheric ages estimated by this ratio vary over a large range for aerosols collected at different locations.

^{210}Po and ^{210}Pb on aerosols that are not produced in the atmosphere (i.e., soil-derived rather than atmospherically produced) are called *supported* or *excess*. Excess ^{210}Po and ^{210}Pb have been identified in several different aerosol studies, and cause inaccurate estimation of aerosol age. Kim et al. (2005) found positive correlations between non-sea-salt sulfates and excess ^{210}Po in precipitation, and also suggested that there is a component of anthropogenic ^{210}Po that is contributed from aerosol formed in coal combustion in urban atmosphere. ^{210}Pb and ^{210}Po in the soil can be taken up by plants and accumulated in plant tissues, which can then be released into the atmosphere during biomass burning events. Biomass burning emissions were found to contribute ^{210}Po in urban aerosols and to cause pronounced seasonal variability of ^{210}Pb (Ram and Sarin, 2012). ^{210}Po emissions were also identified as a result of crustal movements, i.e., volcanic eruptions and earthquakes (Lambert et al., 1985). In a review of sources of atmospheric ^{210}Po (Baskaran, 2011), volcanic activity and ^{222}Rn emanation from ground were identified as the two largest sources, which are about 63% and 28% of

the total annual emission of ^{210}Po . In coastal regions, bio-volatilization could be a source of excess ^{210}Po (Kim et al., 2000). ^{222}Rn emanation from oceans, rivers and lakes is negligible compared to continental sources (Whittlestone, 1990).

In this study, we measured ^{210}Po activities on aerosols collected in the free troposphere in the central North Atlantic, determined aerosol age using ^{210}Po activities and decay rate and investigated the aerosol sources using an transport model. We estimated the activity ratio of $^{210}\text{Po}/^{210}\text{Pb}$ for all the samples and calculated age of aerosols by in the samples that were not affected by sources of excess isotope. The results are compared with other studies of atmospheric ^{210}Po activity and aerosol ages.

4.2 Methods

4.2.1 Aerosol sampling at PMO

Pico Mountain Observatory (PMO, 38.47°N, 28.40°W, 2,225 m a.s.l.), in the Azores Islands, was established for studying long-range transport of air masses from neighboring continents to the central North Atlantic. Long-range transport of air masses from North America is the most frequently observed transport pattern due to predominantly westerly winds in the mid-latitude regions, while transport from Europe and Africa is observed occasionally (Honrath et al., 2004). Aerosol filter sampling started

in 2012 and thereafter was conducted every summer at PMO. Daily filter samples were collected by high-volume samplers from May to September in 2013 except when extreme weather conditions prevented continuous operation of the station. The filters (Whatman, 8×10 inch Quartz Microfibre Filters, CAT No. 1851-865) used were for the purpose of PM_{2.5} (aerodynamic diameter less than 2.5 μm) collection. ^{210}Po activities in a total of 73 samples (days) were measured.

4.2.2 ^{210}Po Alpha spectrometry

After field sampling, the filter samples were delivered to Michigan Technological University for preparation. A circle (diameter of 47 mm) cut from each filter was used for ^{210}Po Alpha spectrometry. The samples usually arrived after a time period of a few days to three weeks after field sampling. Extraction and Alpha counting started immediately after arrival, because separation of ^{210}Pb and ^{210}Po is crucial and prevents ongoing production of ^{210}Po . The extraction procedure was modified from a method used for Po measurement in sediment samples from Eakins and Morrison (1978) as described below.

The initial sample cut from the filters was weighed and cut into small pieces. The pieces were then transferred to a test tube, with addition of a known spike of internal standard (^{209}Po , half-life = 125.2 years) and a few drops of concentrated hydrochloric

acid (HCl). The sample was mixed and stirred with a glass rod. De-ionized water was added if the filter pieces were not immersed. Then, a batch of four samples were placed on an electric hotplate in the fume hood with temperature set at 200-250°C. The samples were heated for 48 hours to dissolve the Po on the filter. The test tubes were put into a tube furnace at 800 ± 50 °C for 30 min. A piece of damp glass wool was placed in the open end of the test tube while burning to collect evaporated *Po*. After burning, the glass wool was transferred into a heated HCl solution and boiled for 30 min. Then, the solution was poured into a plastic bottle with a silver planchet placed at the bottom. The bottles were heated in an oven for 48 hours at 95°C. The *Po* in solution was transferred onto the surface of the planchet. Eventually, the planchets were placed into detection chambers of an Octet alpha-spectrometer and counted for three days to obtain enough counts.

The total recovery efficiency of ^{210}Po in the lab procedures was calculated using the following steps. During the transport of filter samples from PMO to Michigan Tech, both production of ^{210}Po by continuous decay of ^{210}Pb and decay of ^{210}Po occurred. A correction was applied to the measured ^{210}Po according to the time periods between the sampling date and plating date. Lab-prepared samples of ^{209}Po standards were used to examine recovery efficiencies of extraction procedures and detector efficiencies. The extraction efficiency of this method varied each time due to difficulties in controlling the final solution volume during the heating procedure. The recovery efficiency for the lab procedures ranged from 35-65%.

The final ^{210}Po activity in the air sample was calculated using the equation below followed by declarations of the variables:

$$A_{210\text{Po}} = C_{210\text{Po}} \div \frac{C_{209\text{Po}}}{C_{209\text{Po}-t}} \div E_c \div (3600 \times t_c) \div e^{(-\frac{\ln(2)}{138} \times \Delta t_1)} \div \frac{\text{Area}_{\text{cut}}}{\text{Area}_{\text{filter}}} \div (F \times t_f) \quad (4.2)$$

$A_{210\text{Po}}$: activity of Po in sampled air, in unit of $\text{Bq}/(\text{m}^3 \text{ air})$.

$C_{210\text{Po}}$: counts of ^{210}Po in unit of 1.

$C_{209\text{Po}}$: counts of ^{209}Po , internal standard, in unit of 1.

$C_{209\text{Po}-t}$: theoretical counts of ^{209}Po calculated by the known amount and activity of the standard solution injected, in unit of 1.

$\frac{C_{209\text{Po}}}{C_{209\text{Po}-t}}$: recovery ratio of ^{209}Po .

E_c : counting efficiency determined by detectors and chambers.

t_c : counting time in hour.

Δt_1 : days between counting date and plating date, normally is 2 days.

F : airflow rate of high volume sampler at PMO, in m^3/hour .

t_f : sampling time, in hour.

4.2.3 Measured particle mass concentration

A very rough calculation of particle mass concentration was carried out by multiplying a universally assigned aerosol density (1.50 g/cm^3 , reported and employed in Petroff and Zhang (2010)) with the measured particle diameters (MetOne Particle Counter, model: GT-521). Particle numbers were counted in a nine-channel mode ($0.3\text{-}0.4 \mu\text{m}$, $0.4\text{-}0.5 \mu\text{m}$, $0.4\text{-}0.5 \mu\text{m}$, $0.5\text{-}0.6 \mu\text{m}$, $0.6\text{-}0.7 \mu\text{m}$, $0.7\text{-}0.8 \mu\text{m}$, $0.9\text{-}1.0 \mu\text{m}$, $1.0\text{-}2.0 \mu\text{m}$ and $2.0\text{-}4.0 \mu\text{m}$) from May to early August and in a two-channel ($0.3\text{-}0.4 \mu\text{m}$ and $0.4\text{-}4.0 \mu\text{m}$) mode mid-August to September. Particle counts in the nine-channel mode were re-grouped and fitted into the two-channel mode distribution. The estimated aerosol mass concentrations estimated through this method were extremely high and might not accurate. The particle mass concentrations were only used to determine the time periods when aerosol loads were relatively heavier.

4.2.4 Transport trajectory simulation and estimation of pollution sources

The Lagrangian particle dispersion model (LPDM) FLEXPART (version 8.2; Stohl et al. (1998)) was used to simulate transport to PMO. The Global Forecast System Final Analysis data from the National Center of Environment Protection was used to

drive FLEXPART. The backward simulation product is an upwind distribution of the simulated air parcels in the atmosphere (also called retroplumes). The relative abundance of residence times over different geographical locations represents the relative amount of air mass from there.

Retroplumes can be used to calculate a time series of tracer concentrations at the receptor contributed by a certain emission source (e.g., anthropogenic or biomass burning) by multiplying the simulated retroplume residence time with emission inventories (Seibert and Frank, 2004). In order to study the impacts from anthropogenic and wildfire emissions, the Emissions Database for Global Atmospheric Research (Olivier and Berdowski, 2001) and Global Fire Assimilation System (Kaiser et al., 2012) CO emission inventories were combined with retroplumes to predict impacts of the two types of emissions on the PMO aerosol samples. The CO contributions from different continents were also used to assess potential relationships between the air mass origins and ^{210}Po activities.

4.3 Results and discussions

4.3.1 Time series results

We were able to measure the entire ^{210}Po alpha spectrometry procedures for 73 samples. Unmeasured samples included contaminated or destroyed ones during sampling and lab experiments and later samples that were aged long enough to be close to equilibrium. The time series of ^{210}Po activity, the estimated atmospheric residence times and FLEXPART simulated transport residence time ratios (RT) for the aerosol samples are shown in Fig. 4.2. Particle mass concentrations and FLEXPART simulated retroplume residence time ratios over North America and Africa are also provided in the figure. ^{210}Po activities in the air at PMO ranged from below detection limit (BDL) to $2.71 \times 10^{-5} \text{ Bq/m}^3$ during May to September, 2013. High ^{210}Po activities ($> 1.0 \times 10^{-5} \text{ Bq/m}^3$) were seen in early July and mid-August (periods are highlighted in the Fig. 4.2). During these periods, high particle mass concentrations were also observed. These high concentrations were likely from the contribution of African dust as suggested by African residence time ratios for the associated FLEXPART retroplumes (Fig. 4.2). The values of the African residence time ratios were up to 5% during the two periods, which are less than the ratios for North American (up to 20%). However, such ratios do not occur frequently in the central North Atlantic,

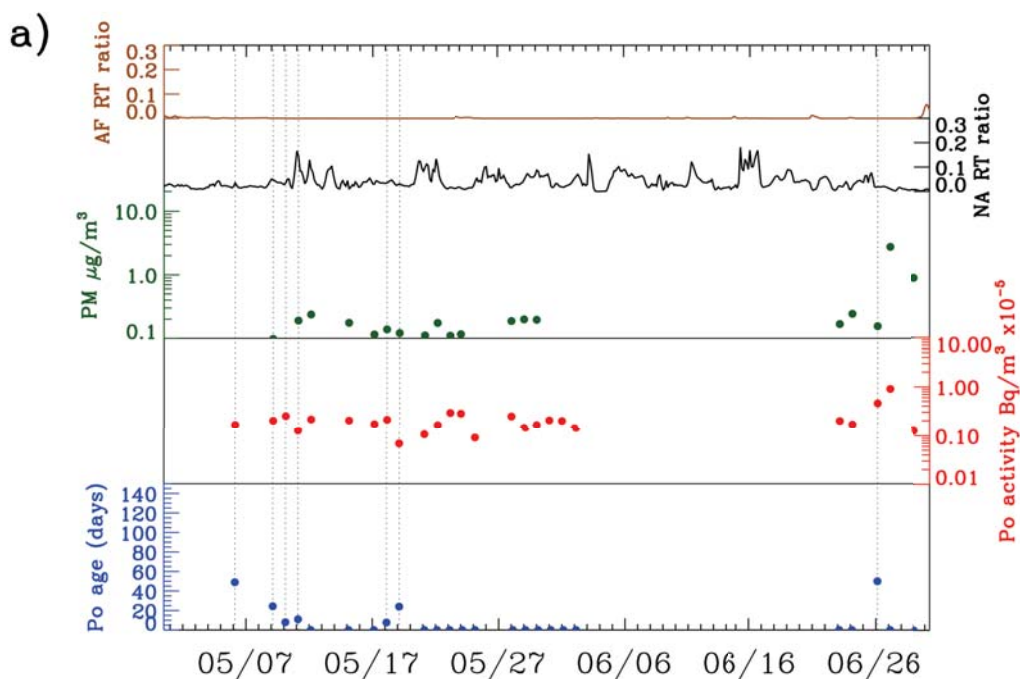


Figure 4.2: Time series results (for May and June of 2013 (a)) of ^{210}Po activity (red), particle mass concentration (green), FLEXPART retroplume residence time distribution ratios in the lower troposphere (0-2500 m) over North America (NA, in black) and Africa (AF, in brown) and aerosol atmospheric residence times calculated by decay of ^{210}Po (solid blue). Aerosol ages ranges from -23 days to over 900 days. The negative values are considered as a result of ^{210}Po activities BDL and are displayed as zeros. Values over 100 days are displayed as 80 days for inclusion in the same screen. The time windows highlighted on the upper x-axis indicate the periods that are affected by transport from Africa as suggested by FLEXPART RT ratios. Dashed vertical lines indicated the qualified samples for the calculation of aerosol ages.

which strongly suggests transport event from Africa.

The results show two types of abnormal aerosol ages. One type of sample has negative aerosol ages (about 33% of total samples, and the lowest estimated age was -23 days).

These samples were categorized as Below Detection Limit (BDL). Mathematically, the

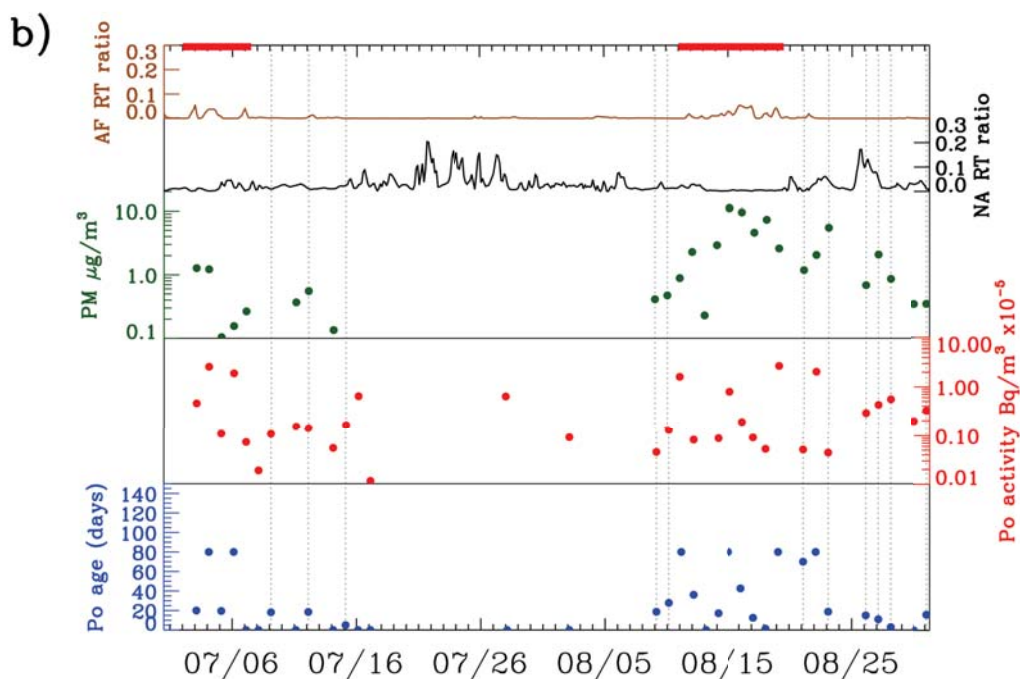


Figure 4.3: Same as Figure 4.2, but for July and August of 2013 (b).

negative values were caused by low ^{210}Po activities that resulted, in some cases, from long sample holding/storage times prior to isotope extraction. Subtracting the days between the time of aerosol sampling at PMO and of ^{210}Po plating could result in negative values of aerosol ages. For keeping a reasonable range in the figure, all negative values were brought up to zero days in Fig. 4.2. Conversely, a few estimated aerosol ages were extremely high (500-900 days). These high ages are displayed as 80 days in the figure to facilitate viewing all values. Interestingly, the high aerosol age also coincided with the potential African dust samples, which is discussed in more detail below.

4.3.2 African dust impacts

To investigate the contribution from pollution emissions to ^{210}Po activities at PMO and also to further examine the potential African dust impacts on aerosol age, we examined relationships between FLEXPART-derived CO mixing ratios from different sources and the observed ^{210}Po activities. The time series of FLEXPART CO from different sources are shown in Fig. 4.4 for July and August of 2013, the two months when high ^{210}Po activities were observed. FLEXPART CO consists of CO from anthropogenic and wildfire emissions, and each type of source contributes differently due to varying transport routes and emission location and intensity. The FLEXPART CO results suggest PMO received up to 10 ppbv of CO from Africa during the two periods July 2-6 and August 11-19 (highest on July 3rd). These periods coincided with the time when high ^{210}Po activities were observed. The African CO contribution was small compared to that from North America or wildfire emission in the remaining days of July and August, but it still suggests transport of ^{210}Po from Africa, because CO emissions are low in the African desert regions (Residence time analysis related to July 2-6 and August 11-19 are given later). The results of reduced major axis regression are given in Fig. 4.5. showing the relationships between ^{210}Po activities on different days and the FLEXPART simulated CO contribution. The correlation coefficients (R) for the global, North American and wildfire emissions were close to zero suggesting no correlations between these pollution sources and ^{210}Po activities.

As found in the literature, wildfire has been found to volatilize ^{210}Po from vegetation and to re-suspend ^{210}Po (Ram and Sarin, 2012), but we find that ^{210}Po at PMO was not clearly affected by wildfire emissions. The correlation between ^{210}Po activities and African CO was also low but has a higher correlation coefficient ($R = 0.34$, $p - \text{value} = 0.13$) than other sources, which suggests higher possibility of African sources.

To verify the sources of the aerosol samples related to the two periods, FLEXPART retrorplumes for two events during the periods of interest are shown in Fig. 4.6, which clearly indicate potential transport from Africa. Evidence of African dust in the aerosol samples was also provided by Aethalometer measurements. A difference in the equivalent black carbon mass concentrations (Fig. 4.7) obtained by measuring light intensities at different wavelengths with the aethalometer indicate the presence of aerosol compositions that absorb with a different Ångström exponent from the black carbon (typically assumed to be close to 1; Fialho et al. (2005)). In this case, these were likely associated with iron-oxides-containing particles reaching PMO from the African continent. Enriched ^{210}Po and ^{210}Pb have been found before in long-range transported Saharan dust samples (Nho et al., 1996). ^{210}Po in the re-suspended dust may represent “excess” sources rather than ^{210}Po from ^{222}Rn decay in the atmosphere. The isotope accumulated in such dust samples could result from both the in situ decay and from atmospheric deposition, so it does not correctly reflect the aerosol age in the atmosphere (Baskaran, 2011).

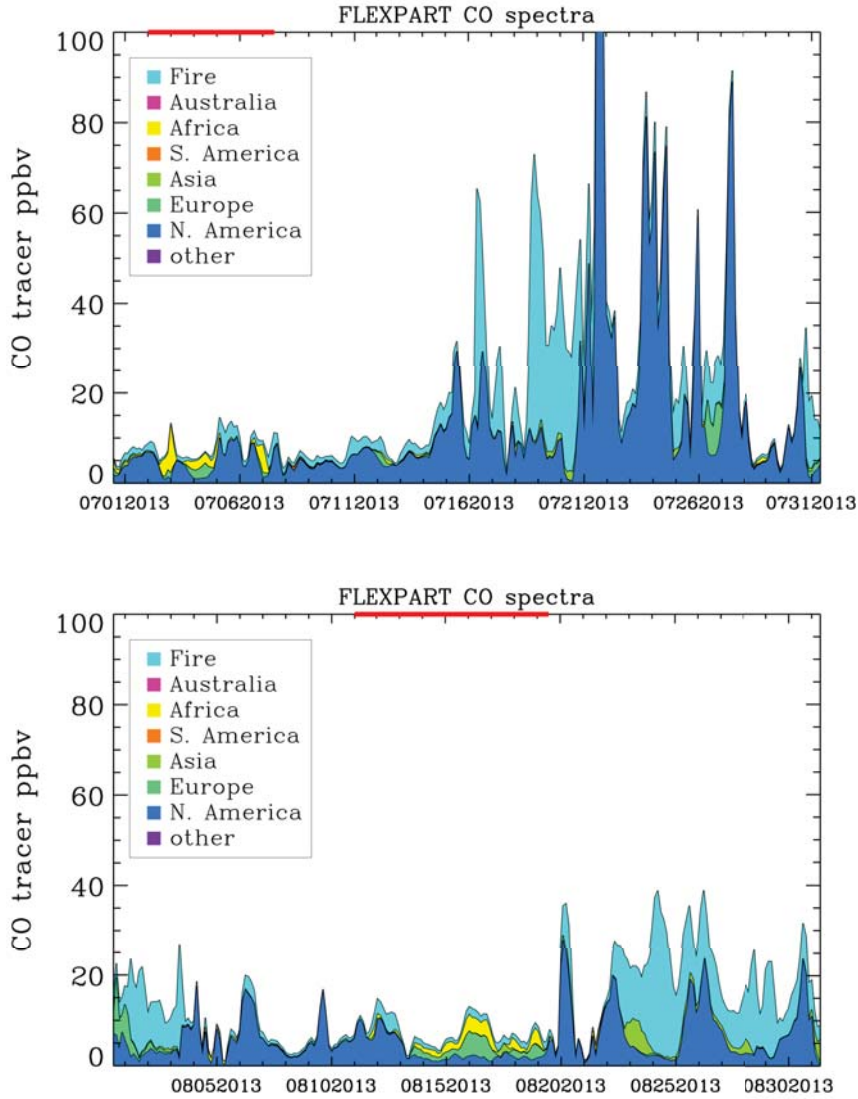


Figure 4.4: FLEXPART simulated CO contributions from anthropogenic emissions of different continents and global wildfire emissions for July and August in 2013 when high ^{210}Po activities were mainly observed. The time windows highlighted on the upper x-axis indicate the periods that are affected by transport from Africa as suggested by FLEXPART RT ratios.

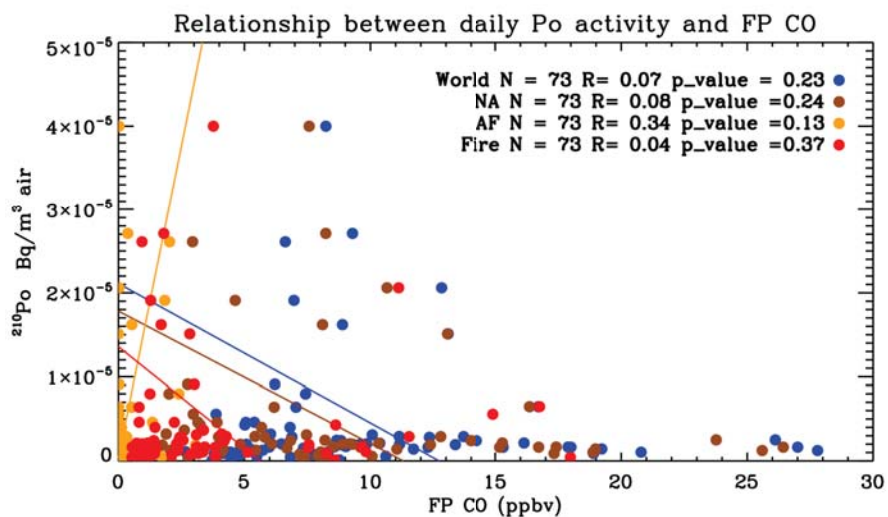


Figure 4.5: Relationships between FLEXPART simulated CO contribution (FP CO) from the world, North America (NA), Africa (AF) and Fire emissions and measured ^{210}Po activities. Only for Africa-derived CO is there a significant correlation.

4.3.3 Estimated aerosol age at PMO

Only 18 aerosol samples could be used for the calculation of aerosol age after the exclusion of dust samples and those below the detection limit. The ages of the 18 samples range from 1.3 to 70.0 days. As shown in Fig. 4.8, the distribution of aerosol ages is skewed, which means the median (19.9 days) and the geometric mean (20.7 days) are better estimates of the central tendency of the sample ages than the mean

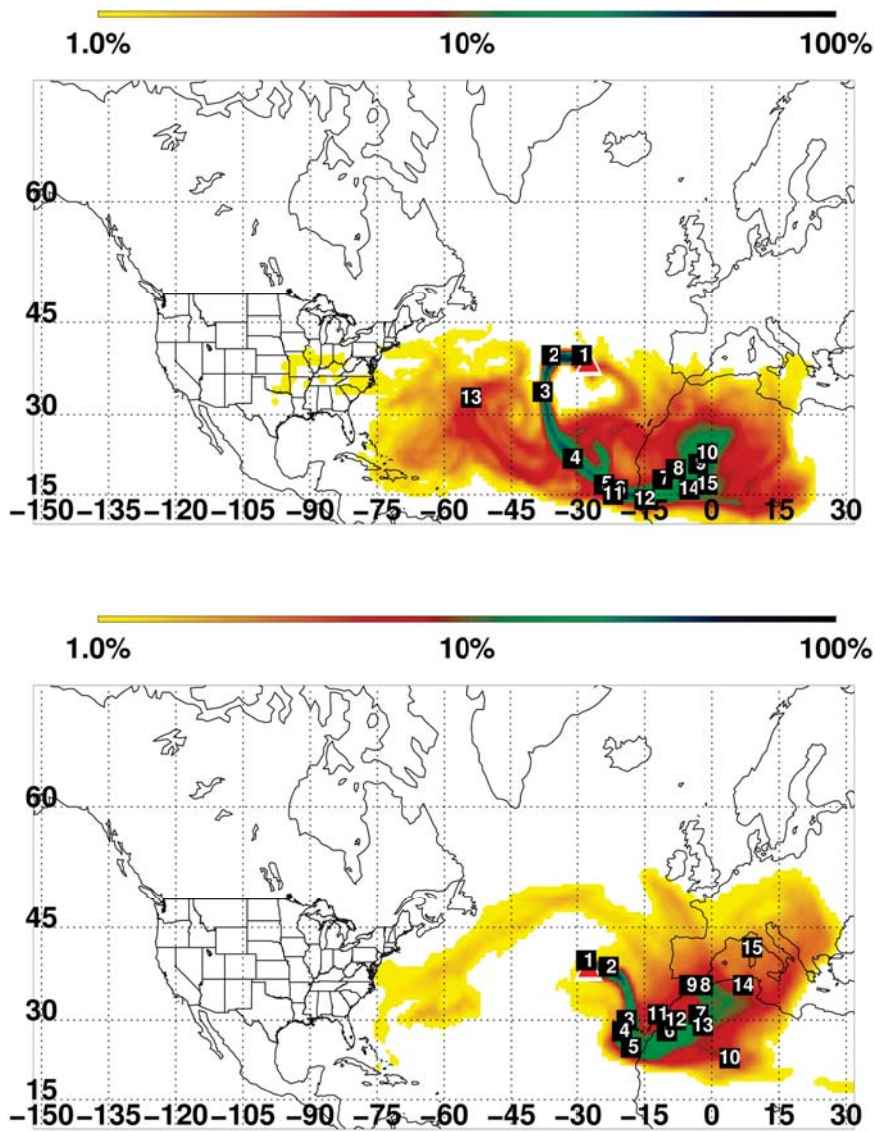


Figure 4.6: Column-integrated residence time distribution of FLEXPART retroplumes for two events (July 3rd, 6:00 AM (upper) and August 16th, 9:00 PM (lower) UTC) during early-July and mid-August when high ^{210}Po activities were observed. Residence time is color coded by a liner grade showing the relative abundance on a map view. The numbers on the maps show the locations of the major portion of the plume on each upwind day.

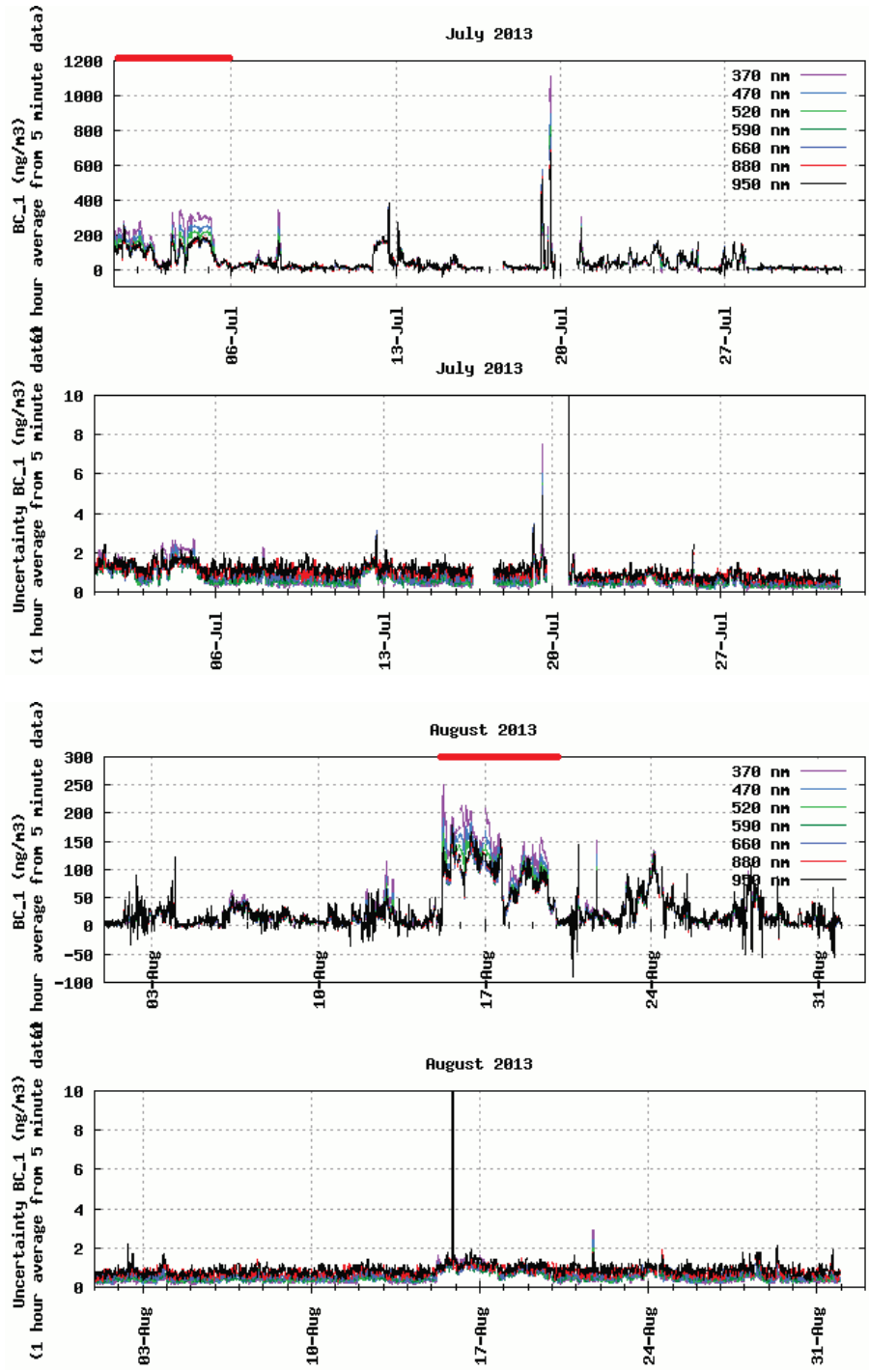


Figure 4.7: Particle equivalent black carbon mass concentration measured by Aethalometer for July and August 2013. The colors show measurements at different wavelengths. The time windows highlighted on the upper x-axis indicate the periods that are affected by transport from Africa.

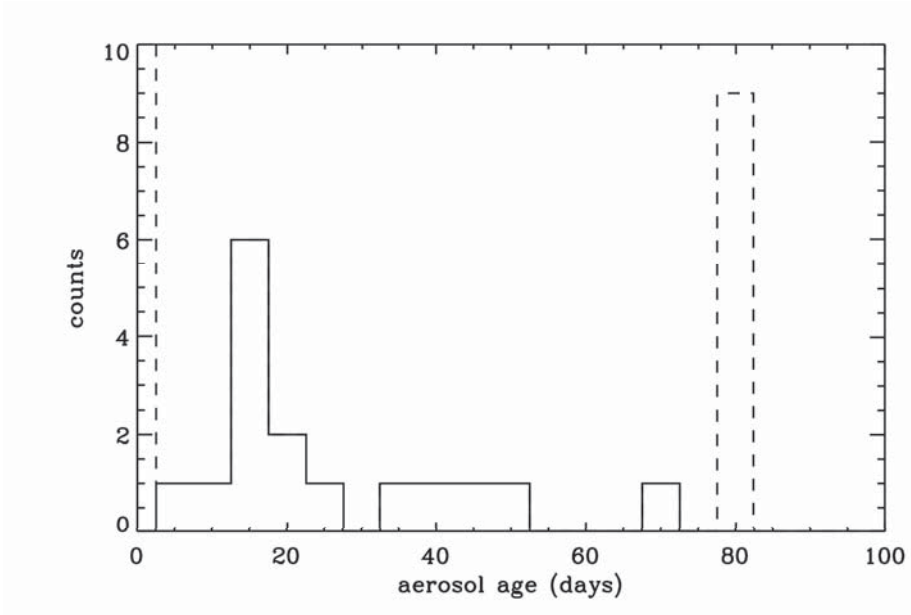


Figure 4.8: Distribution of the estimated aerosol ages. Dashed lines indicate the samples that are below detection limit or that are affected by African dust.

(26.3 days), which has a standard deviation of 17.0 days. The large standard deviation came from propagated uncertainties generated in the measurement of ^{210}Po activities and in solving Eq. 4.1.

In an attempt to look for sources of the ^{210}Po activities for these 18 samples, we were not able to find a clear correlation between ^{210}Po activities and retroplume residence time over the surrounding continents. As shown in Fig. 4.9, ^{210}Po activities for these 18 samples were plotted against residence time ratios over North America, Africa and Europe. The correlation coefficients (R) are small (<0.1) for all the three potential sources, possibly implying the samples are highly aged and contain particles from different places. The lack of a common origin suggests that the ^{210}Po in

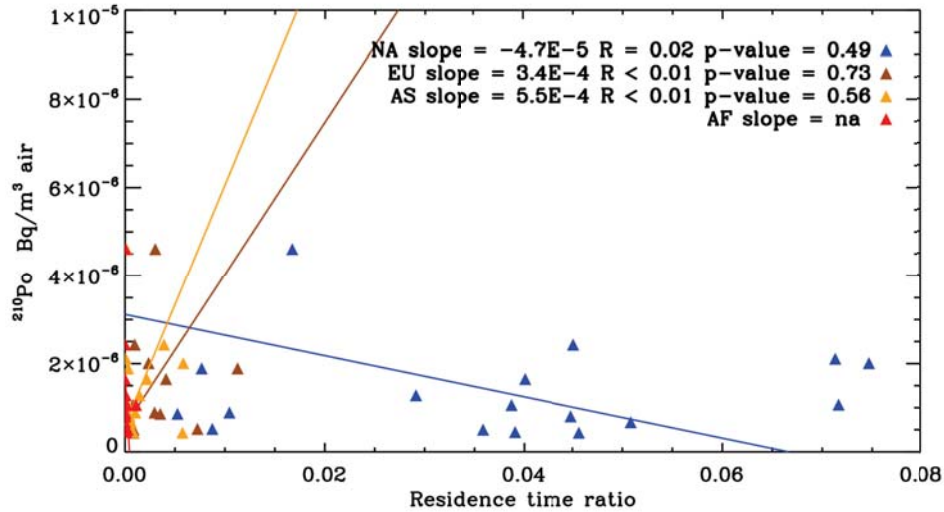


Figure 4.9: Relationships between observed ^{210}Po activities and ratios in the lower troposphere (0-2500 m) over North America (NA), Europe (EU), Asia (AS) and Africa (AF) for the aerosol samples that are determined as non-affected by African dust.

these samples is not derived from dust storms originating from a common continental source. The linear regression between particle mass concentration and estimated aerosol ages shows a very weak ($R = 0.02$ *pvalue* = 0.30) negative (slope = -3421.2) correlation (Fig. 4.10), which suggests that the more heavily loaded aerosols have ages similar to those of the lightly loaded ones. The reason for this is not quite clear, because usually high concentration of aerosols is likely observed in quick transport from the continent, in which there is shorter time for aerosol deposition. A significant correlation might indicate that even these samples were influenced by excess ^{210}Po .

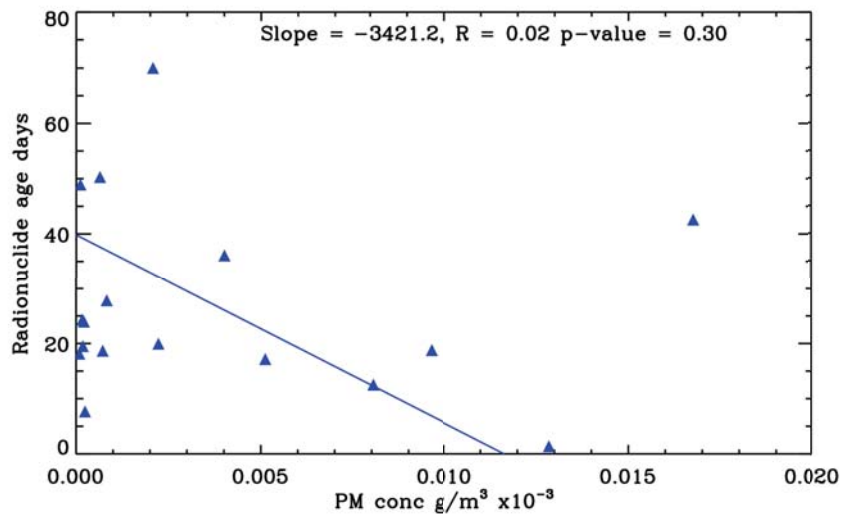


Figure 4.10: Relationships between estimated aerosol ages and particle mass concentrations for the aerosol samples that are determined as non-affected by African dust.

The absence of a correlation is reassuring, and helps to support the validity of the calculated aerosol ages.

Table 4.1
A summary of estimated atmospheric aerosol ages using $^{210}\text{Po}/^{210}\text{Pb}$ ratios

Location	Sampling time	Elevation (m)	$^{210}\text{Po} \times 10^{-5} (\text{Bq}/\text{m}^3)$ (average)(range)(n)	Estimated aerosol age (days) (average)(range)(n)	Air type	Reference
Pico, Azores Boulder, Colorado	May-Sep. 2013 1967-1972	2 225 ground	0.493 ± 0.91 (BDL) ^a - 2.71)(73) 3.5 ± 3.2 (0.18-11.5)(20)	20. (7.4-70.0) (18) (11- 77) (20)	free troposphere university campus	this work ^c
Arctic region South Pole	Jan. -Mar. 1996 Nov. 2000- Jan. 2001	ground 2841	^a (0.0-1.52)(10) 2.2 ± 0.11 () (4.5 - 7.0)	- (0 - 39) (10) 35 - 47 (9 & 33) ^b	Arctic haze South Pole	^d ^e
Malaga Lodz, Poland	1996 - 2001 Feb. & July 2009	ground ground	- -	31 (31-36) (-) - (7-120)(18)	coastal site urban	^f ^g
Detroit, U.S. Kapur	Sep. 1999 - Mar. 2001 Jan. 2007 - Apr. 2009	ground 142	- 9.4 (0.2-28) (21)	22.0 (0.0-61.0)(-) 23.4 (2.5-59.3) (99) ^b	urban urban	^h ⁱ
Lodz, Poland Lodz, Poland Xiamen, China	2010-2011 2010-2011 2010-2012	ground ground ground	- - 3.4 ± 0.15 (0.14-41.02) (32)	- (1 - 25)(-) - (103- 205)(-) 28.3 ± 3.0 (3.1 - 57.5) (42)	urban stratosphere urban	^j ^k ^l

^a Below detection limit

^b Aerosol age was not reported directly. The estimated value is calculated from the $^{210}\text{Po}/^{210}\text{Pb}$ in the original work using Newton-Raphson method.

^c Poet et al. (1972); ^d Baskaran and Shaw (2001); ^e Arimoto et al. (2004); ^f Duenas et al. (2004);

^g Dhugosz et al. (2010); ^h McNeary and Baskaran (2007); ⁱ Ram and Sarin (2012); ^j Dhugosz-Lisiecka and Bem (2012);

^k Dhugosz-Lisiecka and Bem (2012); ^l Wang et al. (2014).

The estimated aerosol atmospheric ages reported here and in other studies vary over a wide range. Other studies using the same radionuclide approach have also reported widely-varying aerosol atmospheric ages and large uncertainties in their results. If the aerosol ages were not directly reported in the original references, estimated ages were calculated from $^{210}\text{Po}/^{210}\text{Pb}$ ratios reported in the studies using Eq. 4.1 (solved by Newton-Raphson method (Chapra, 2007)). Ages of aerosol samples collected in urban areas were estimated to be in the same range as or younger than those at PMO. Poet et al. (1972) estimated a range of age of 11-77 days in surface air, which was greater than that estimated by $^{210}\text{Bi}/^{210}\text{Pb}$ (4 days) due to influence of excess isotope sources. In a more recent study of urban aerosol at Lodz, Poland, Długosz-Lisiecka and Bem (2012) estimated ages of 1-25 days in the troposphere. At a remote site, Baskaran and Shaw (2001) measured a range of age of 0-39 days in Arctic regions. A few studies reported longer ages. Długosz-Lisiecka and Bem (2012) reported ages of 103-205 days in the lower stratosphere. Duenas et al. (2004) found the values of aerosol age did not vary much seasonally (31-36 days) at Maraga, Spain, a Mediterranean costal site, based on six years of observation, even though some degree of variation was found for ^{210}Po and ^{210}Pb activities. Local climate and meteorological conditions could also be a reason for the variability in the values of age, because aerosol ages largely depend on latitude and altitude due to the differences in precipitation, humidity and land use (Papastefanou, 2006).

The geometric mean of the aerosol ages at PMO (20.7 days) is longer than that measured at continental sites, suggesting that aerosol collected at PMO results from long-range transport. In general, aerosol age in the troposphere was found to be 4.8-15.3 days based on measurements of radionuclides attached on aerosols (Papastefanou, 2006). The estimated aerosol age at PMO is higher than the time that the anthropogenic pollution plumes usually take to travel from North America to PMO (5-7 days as estimated in Honrath et al. (2004)). In a non-event-specific study on non-methane hydrocarbons observed during 2004 and 2005 at PMO, Helmig et al. (2008) estimated the air masses were 1-2 weeks old based on measured bulk NMHC ratios. Zhang et al. (2014), using chemical transport modeling, found the non-methane hydrocarbons aged 5-6 days in two transport events of North American plumes. In previous studies, PMO was shown to be an elevated site that is ideal for observation of long-range transport in the free troposphere. Deposition processes are not as efficient as in the boundary layer, so aerosols collected at high altitude may have longer half-lives. The most aged of aerosols in the stratosphere can be as old as hundreds of days (Długosz-Lisiecka and Bem (2012)), and mixing of upper tropospheric and stratospheric air is possible at PMO. The aerosol age estimated here and the air plume travel times based on gaseous species in the previous PMO studies are not necessarily contradictory. Aerosols undergo efficient removal processes and behave differently than gases. It is possible that the gas compositions indicate the travel times from the North American continent while the isotopes indicate the ages of long-lived, fine

aerosols. The long-lived aerosol age is also in agreement with electron microscopy analysis conducted on filter samples collected in 2012, in which we visually identified compacted and aged soot particles (China et al., 2015).

4.4 Conclusions and suggestions for methods improvement

We measured an atmospheric radionuclide tracer, ^{210}Po , during summer 2013 at PMO, and estimated ages of the aerosol samples by analyzing the in situ decay rate of ^{210}Po . Due to the remote location of PMO and the long transport time from the neighboring continents (usually longer than 5 days), aerosol load usually is much lower compared to that at continental sites. As a result, ^{210}Po activities on more than 33% of the filter samples we collected during summer 2013 were found to be below the detection limit. High ^{210}Po activities ($> 1.0 \times 10^{-5} \text{ Bq/m}^3$) were observed for two specific time periods, early-July and mid-August. These two time periods were associated with transport from Africa to PMO, as shown by FLEXPART simulated retroplumes and the CO contribution from Africa. The equivalent black carbon mass concentrations measured by Aethalometer indicated that the high ^{210}Po activities were due to transported dust aerosols. Estimated ages of the affected aerosol samples were high (> 100 days). These samples were all excluded for the estimate aerosol

age, because dust could potentially carry excess ^{210}Po , which can be aged for years before being re-suspended.

Only 18 aerosol samples out of the total 73 samples were qualified for aerosol age calculation, showing the median aerosol age of 20.7 ± 17.0 days at PMO. This estimated aerosol age is about three times the previous estimates of transport from North America. The common estimate of aerosol lifetime in the atmosphere is about two weeks but the long age of PMO aerosols could be due to the unique location of PMO as a remote free troposphere site. The deposition rates should be less efficient in the free troposphere. The large and more easily deposited aerosol particles are likely removed during long range transport, which leaves the fine and long-range transported aerosol particles in the free troposphere. The high uncertainty of the estimated average age can be possibly improved by enhancing the mass of aerosols used for alpha counting and reducing the time period between filter sampling and the first alpha counting. We suggest that ^{210}Po extraction and plating be carried out at PMO using a greater amount of filter sample, which could reduce the uncertainty (generated during error propagation) and enhance ^{210}Po signals in the alpha spectrometry.

Chapter 5

Conclusions and future research

This dissertation developed three detailed studies on the characteristics of long-range transport to PMO and chemical observations conducted there. The work explored ozone production tendency during the transport of air pollution from North America to PMO, characterized chemical signatures for different transport patterns and estimated aerosol atmospheric residence time using measurements of atmospheric radionuclide tracers. The dissertation answers questions raised in previous studies, such as reasons for ozone enhancement at PMO, and provides more insights on variation in air mass composition in the free troposphere over the central North Atlantic.

5.1 Ozone production tendency during transport from North American to PMO

Both anthropogenic and wildfire emissions were found to cause ozone enhancement at PMO in previous studies. The value of $d[\text{O}_3]/d[\text{CO}]$, which has been used to indicate ozone production tendency, was found to be higher at PMO (~ 1) than observations at sites along the east coast of North America. In order to determine the reasons for this high $d[\text{O}_3]/d[\text{CO}]$, FLEXPART retroplumes were combined with GEOS-Chem output to provide a semi-Lagrangian view of ozone chemistry during transport from North America to PMO.

Two transport events of North America anthropogenic pollution plumes were identified by examining CO sources, trajectory analyses, and excluding influence of mechanically forced upslope flow to PMO. The folded FLEXPART and GEOS-Chem results indicate that meteorological conditions and transport pathways largely determined the chemical transformation in the two pollution plumes. In the plume that was lifted by a warm conveyor belt, NO_x was converted into PAN, which led to ozone production in the subsidence driven by the Azores-Bermuda anticyclone when the plume approached PMO. In another plume, the potential for ozone production was low due to active mixing at low altitude, and ozone was primarily destroyed during

the transport. In the analysis of $d[\text{O}_3]/d[\text{CO}]$ transformation during transport, it was found that high ozone and OH levels in the pollution plumes accelerated CO loss, which was partially responsible for the high $d[\text{O}_3]/d[\text{CO}]$.

5.2 Characterization of chemical signatures for different transport patterns

It was realized that transport pathways could affect the air composition observed at PMO after long-range transport. The important transport patterns include North Atlantic free troposphere background, transport of North American anthropogenic emissions, transport of wildfire emissions, subsidence flow and upslope flow. The frequent transport patterns and the associated chemical signatures were studied in Chapter 3.

Both pollution types of pollution emissions were found to contribute enhancement of tracer gas at PMO. Anthropogenic emissions contribute 14–23 ppbv (13%–28%) CO and 10 ppbv (25%–30%) ozone to the background levels at PMO. Summertime wildfires cause even more pollution (25 ppbv (30%) of CO and 16 ppbv (45%) of ozone). Downward transport contributes higher ozone enhancement to Anthropogenic emissions but occurs less frequent. Transport at high altitude (>5 km) alters ozone

production tendency during transport by converting NO_x to PAN during lifting of air pollution plumes.

Relationships between trace gases for different transport patterns were also studied. The indicator of ozone production tendency, $d[O_3]/d[CO]$, for Fire (0.12-0.33) was lower than NA-anthro and NATL, which was due to much larger magnitude of CO emission from wildfires. The high $d[O_3]/d[CO]$ values of NATL (0.66-0.75) could be a distinct characteristic of the free troposphere over central North Atlantic. The photochemical ages (7-20 days) indicated by NMHC photochemical clock are generally in agreement with the understanding of transport time from North America to PMO.

5.3 Aerosol atmospheric residence time estimated using radionuclide tracers

Atmospheric aerosols are involved in cloud formation, and thus can largely affect global radiative forcing. Understanding aerosol age is critical to improve chemical transport modeling. For better understanding of aerosol residence time, use of atmospheric radionuclide tracers has the advantage that is their sources and reactions are easier to determine than chemical composition of aerosols.

Aerosol atmospheric residence time was determined using Po alpha spectrometry.

^{210}Po ($t_{1/2} = 138$ days) is a long-lived daughter of ^{222}Rn . It can be produced on aerosols in the atmosphere in the decay chain of ^{222}Rn , and its decay rate can be used to estimate the source and atmospheric residence time of the attached aerosols. For the 73 aerosol samples that were collected during summer 2013, the highest ^{210}Po activities ($> 1.0 \times 10^{-5} \text{ Bq/m}^3$) were observed for two specific time periods, early-July and mid-August. These two time periods were identified as transport from Africa to PMO, as supported by FLEXPART simulations and the equivalent black carbon mass concentrations. These samples were affected by re-suspended dust, and thus were excluded for the estimate of atmospheric residence time of PMO aerosol. Only 18 aerosol samples were qualified for aerosol age calculation, showing the median atmospheric residence time of 20.7 ± 17.0 days at PMO. This estimated aerosols age is about three times the previous estimates of transport time from North America (5-7 days) and much higher than the common estimate of aerosol lifetime in the atmosphere (1-2 weeks). The highly aged aerosol at PMO could be due to low deposition rates in the free troposphere. The large and more easily deposited aerosol particles are likely removed during long range transport, which leaves the fine and long-range transported aerosol particles in the free troposphere.

5.4 Future research

The findings in Chapters 2 and 3 of this work suggests that it is necessary to more closely study the comprehensive chemical and physical processes during transport, especially when weather systems and frequent changes of environment conditions are involved. This kind of study will provide detailed characterizations of chemical transformation, and thus will help with accurate prediction of air quality and also improve parametrizations in climate models. Chapter 2 uses a combination of a LPDM and CTM to provide a semi-Lagrangian view of chemical transformation for pollution plume transport from North America to PMO. Although the findings in the chapter provide credible explanations for ozone enhancement, more refined modelling techniques are necessary for understanding the details such as accurate prediction of ozone production in subsiding pollution plumes. The methods provided in Chapter 2 are limited by the coarse resolution of CTMs and differing meteorology data used in GEOS-Chem and FLEXPART, so that it cannot be used to resolve chemical transformation at a finer scale, such as a mid-latitude anticyclone. The release of FLEXPART-WRF may perfectly solve the problem. It adapts WRF meteorology fields and should be combined with WRF-Chem flawlessly. FLEXPART-WRF and WRF-Chem are able to share the same grid settings, which will save the step of matching the grids in the models and increase the accuracy in the folding calculation. FLEXPART-WRF is armed with OpenMP and MPI parallel computation features,

which will speed up the simulations and enable running under much higher resolutions. With proper settings, the combination of FLEXPART-WRF and WRF-Chem should be able to provide high quality prediction of chemical transformation. For example, in an intense fire event, ozone production, aerosol formation, particle nucleation, cloud formation and impacts on precipitation can be simulated more accurately.

There are two important limitations that prevent accurate estimation of aerosol ages in Chapter 4. Use of atmospheric radionuclide tracers has been verified in many previous studies as a proper method. However, PMO is a remote site on an island and has low aerosol loads. The samples that are not affected by excess radionuclide attached on dust showed very low activities of atmospheric radionuclide tracers, which undermined the accuracy of the spectrometric analysis because background activities of the atmospheric radionuclide tracers exist everywhere. Therefore, increasing the sampling period is suggested for future collections. Two to five days collection may show better signals given the current lab equipments. The second aspect that may reduce the uncertainty of this method is to shorten the time between finishing up the sampling and solvent extraction. The extraction is suggested to be done at Pico, which would require installation of a tube furnace and an oven. Timely extraction can prevent artificial ageing after finishing up the sampling.

The transport classification developed in Chapter 3 can be used to understand the selected aerosol samples that were used for aerosol age estimation in Chapter 4. Due

to the heavy calculations of transport classification, the dissertation does not include the transport classification and the chemical signature analyses for the aerosol samples collected in 2013. In the future work, when all the measurements of trace gases and modeling results are in place, the selected aerosol samples can be studied in detail. We will be able to understand the sources and transport pathways of the aerosol samples in different ages.

References

- Alvarado, M. J., Logan, J. A., Mao, J., Apel, E., Riemer, D., Blake, D., Cohen, R. C., Min, K.-E., Perring, A. E., Browne, E. C., Wooldridge, P. J., Diskin, G. S., Sachse, G. W., Fuelberg, H., Sessions, W. R., Harrigan, D. L., Huey, G., Liao, J., Case-Hanks, A., Jimenez, J. L., Cubison, M. J., Vay, S. A., Weinheimer, A. J., Knapp, D. J., Montzka, D. D., Flocke, F. M., Pollack, I. B., Wennberg, P. O., Kurten, A., Crouse, J., Clair, J. M. S., Wisthaler, A., Mikoviny, T., Yantosca, R. M., Carouge, C. C., and Le Sager, P.: Nitrogen oxides and PAN in plumes from boreal fires during ARCTAS-B and their impact on ozone: an integrated analysis of aircraft and satellite observations, *Atmos. Chem. and Phys.*, 10, 9739–9760, 2010.
- Arimoto, R., Hogan, A., Grube, P., Davis, D., Webb, J., Schloesslin, C., Sage, S., and Raccach, F.: Major ions and radionuclides in aerosol particles from the South Pole during ISCAT-2000, *Atmospheric Environment*, 38, 5473–5484, 2004.
- Auvray, M. and Bey, I.: Long-range transport to Europe: Seasonal variations and implications for the European ozone budget, *J. Geophys. Res.*, 110, 2005.
- Auvray, M., Bey, I., Llull, E., Schultz, M., and Rast, S.: A model investigation of tropospheric ozone chemical tendencies in long-range transported pollution plumes, *J. Geophys. Res.*, 112, 2007.
- Ayers, G.: Comment on regression analysis of air quality data, *Atmos. Environ.*, 35, 2423–2425, 2001.
- Baker, M. B. and Charlson, R. J.: Bistability of CCN concentrations and thermodynamics in the cloud-topped boundary layer, *Nature*, 345, 142–145, 1990.
- Balkanski, Y., Jacob, D., Gardener, G., Graustein, W., and Turekian, K.: Transport and residence times of tropospheric aerosols inferred from a global 3-dimensional simulations of PB-210, *J. Geophys. Res.*, 98, 573–20, 1998.
- Baskaran, M.: Po-210 and Pb-210 as atmospheric tracers and global atmospheric Pb-210 fallout: a review, *Journal of Environmental Radioactivity*, 102, 500–513, 2011.

- Baskaran, M. and Shaw, G. E.: Residence time of arctic haze aerosols using the concentrations and activity ratios of ^{210}Po , ^{210}Pb and ^7Be , *Journal of Aerosol Science*, 32, 443–452, 2001.
- Berkowitz, C. M., Daum, P. H., Spicer, C. W., and Busness, K. M.: Synoptic patterns associated with the flux of excess ozone to the western North Atlantic, *Journal of Geophysical Research: Atmospheres* (1984–2012), 101, 28 923–28 933, 1996.
- Bey, I., Jacob, D. J., Yantosca, R. M., Logan, J. A., Field, B. D., Fiore, A. M., Li, Q. B., Liu, H. G. Y., Mickley, L. J., and Schultz, M. G.: Global modeling of tropospheric chemistry with assimilated meteorology: Model description and evaluation, *J. Geophys. Res.*, 106, 23 073–23 095, doi:10.1029/2001JD000807, 2001.
- Brioude, J., Arnold, D., Stohl, A., Cassiani, M., Morton, D., Seibert, P., Angevine, W., Evan, S., Dingwell, A., and Fast, J. D.: The Lagrangian particle dispersion model FLEXPART-WRF version 3.1, *Geoscientific Model Development*, 6, 1889–1904, 2013.
- Cain, M., Methven, J., and Highwood, E. J.: Quantification of chemical and physical processes influencing ozone during long-range transport using a trajectory ensemble, *Atmos. Chem. and Phys.*, 12, 7015–7039, 2012.
- Cape, J., Coyle, M., and Dumitrean, P.: The atmospheric lifetime of black carbon, *Atmospheric Environment*, 59, 256–263, 2012.
- Chameides, W. L., Fehsenfeld, F., Rodgers, M. O., Cardelino, C., Martinez, J., Parrish, D., Lonneman, W., Lawson, D. R., Rasmussen, R. A., Zimmerman, P., Greenberg, J., Middleton, P., and Wang, T.: Ozone precursor relationships in the ambient atmosphere, *J. Geophys. Res.*, 97, 6037–6055, doi:10.1029/91JD03014, 1992.
- Chapra, S.: *Applied Numerical Methods with MATLAB for Engineers and Scientists*, The McGraw-Hill Companies, Inc., 2007.
- Chin, M., Jacob, D. J., Munger, J. W., Parrish, D. D., and Doddridge, B. G.: Relationship of ozone and carbon monoxide over North America, *J. Geophys. Res.*, 99, 14 565–14 573, times Cited: 123, 1994.
- China, S., Scarnato, B., Owen, R. C., Zhang, B., Ampadu, M. T., Kumar, S., Dzepina, K., Dziobak, M. P., Fialho, P., Perlinger, J. A., Hueber, J., Helmig, D., Mazzoleni, L. R., and Mazzoleni, C.: Morphology and Mixing State of Aged Soot Particles at a Remote Marine Free Troposphere Site: Implications for Optical Properties, *Geophysical Research Letters*, 2015.
- Cooper, O. R., Moody, J. L., Parrish, D. D., Trainer, M., Ryerson, T. B., Holloway, J. S., Hubler, G., Fehsenfeld, F. C., Oltmans, S. J., and Evans, M. J.: Trace gas signatures of the airstreams within North Atlantic cyclones: Case studies from the

- North Atlantic Regional Experiment (NARE '97) aircraft intensive, *J. Geophys. Res.*, 106, 5437–5456, times Cited: 77 2nd AGU Chapman Conference on Water Vapor in the Climate System OCT 12-15, 1999 POTOMAC, MARYLAND Amer Geophysic Union, 2001a.
- Cooper, O. R., Moody, J. L., Thornberry, T. D., Town, M. S., and Carroll, M. A.: PROPHET 1998 meteorological overview and air-mass classification, *Journal of Geophysical Research*, 106, 24 289–24 299, 2001b.
- Cooper, O. R., Moody, J. L., Thornberry, T. D., Town, M. S., and Carroll, M. A.: PROPHET 1998 meteorological overview and air-mass classification, *Journal of Geophysical Research: Atmospheres*, 106, 24 289–24 299, doi:10.1029/2000JD900409, URL <http://dx.doi.org/10.1029/2000JD900409>, 2001c.
- Cooper, O. R., Gao, R.-S., Tarasick, D., Leblanc, T., and Sweeney, C.: Long-term ozone trends at rural ozone monitoring sites across the United States, 1990–2010, *J. Geophys. Res.: Atmospheres (1984–2012)*, 117, 2012.
- Creilson, J. K., Fishman, J., and Wozniak, A. E.: Intercontinental transport of tropospheric ozone: a study of its seasonal variability across the North Atlantic utilizing tropospheric ozone residuals and its relationship to the North Atlantic Oscillation, *Atmos. Chem. Phys.*, 3, 2053–2066, 2003.
- Cuevas, E., González, Y., Rodríguez González, S., Guerra, J., Gómez Pélaez, A., Alonso Pérez, S., Bustos, J., and Milford, C.: Assessment of atmospheric processes driving ozone variations in the subtropical North Atlantic free troposphere, 2013.
- Daum, P. H., Kleinman, L. I., Newman, L., Luke, W. T., WeinsteinLloyd, J., Berkowitz, C. M., and Busness, K. M.: Chemical and physical properties of plumes of anthropogenic pollutants transported over the North Atlantic during the North Atlantic Regional Experiment, *J. Geophys. Res.*, 101, 29 029–29 042, doi:10.1029/95JD03163, 1996.
- DeCaria, A. J., Pickering, K. E., Stenchikov, G. L., and Ott, L. E.: Lightning-generated NO_x and its impact on tropospheric ozone production: A three-dimensional modeling study of a Stratosphere-Troposphere Experiment: Radiation, Aerosols and Ozone (STERAO-A) thunderstorm, *J. Geophys. Res.*, 110, D14 303, 2005.
- Długosz, M., Grabowski, P., and Bem, H.: ²¹⁰Pb and ²¹⁰Po radionuclides in the urban air of Lodz, Poland, *Journal of radioanalytical and nuclear chemistry*, 283, 719–725, 2010.
- Długosz-Lisiecka, M. and Bem, H.: Determination of the mean aerosol residence times in the atmosphere and additional ²¹⁰Po input on the base of simultaneous

- determination of ^7Be , ^{22}Na , ^{210}Pb , ^{210}Bi and ^{210}Po in urban air, *Journal of Radioanalytical and Nuclear Chemistry*, 293, 135–140, 2012.
- Duenas, C., Fernandez, M., Carretero, J., Liger, E., and Canete, S.: Long-term variation of the concentrations of long-lived Rn descendants and cosmogenic ^7Be and determination of the MRT of aerosols, *Atmospheric Environment*, 38, 1291–1301, 2004.
- Duncan, B. N., Logan, J. A., Bey, I., Megretskaia, I. A., Yantosca, R. M., Novelli, P. C., Jones, N. B., and Rinsland, C. P.: Global budget of CO, 1988-1997: Source estimates and validation with a global model, *J. Geophys. Res.*, 112, D22 301, doi: 10.1029/2007JD008459, 2007.
- Dunlea, E. J., DeCarlo, P. F., Aiken, A. C., Kimmel, J. R., Peltier, R. E., Weber, R. J., Tomlinson, J., Collins, D. R., Shinozuka, Y., McNaughton, C. S., Howell, S. G., Clarke, A. D., Emmons, L. K., Apel, E. C., Pfister, G. G., van Donkelaar, A., Martin, R. V., Millet, D. B., Heald, C. L., and Jimenez, J. L.: Evolution of Asian aerosols during transpacific transport in INTEX-B, *Atmos. Chem. Phys.*, 9, 7257–7287, times Cited: 56, 2009.
- Dzepina, K., Mazzoleni, C., Fialho, P., China, S., Zhang, B., Owen, R. C., Helmig, D., Hueber, J., Kumar, S., Perlinger, J. A., Kramer, L., Dziobak, M. P., Ampadu, M. T., Olsen, S., Wuebbles, D. J., and Mazzoleni, L. R.: Molecular characterization of free tropospheric aerosol collected at the Pico Mountain Observatory: a case study with long range transported biomass burning plumes, *Atmospheric Chemistry and Physics Discussions*, 14, 24 753–24 810, doi:10.5194/acpd-14-24753-2014, URL <http://www.atmos-chem-phys-discuss.net/14/24753/2014/>, 2014.
- Eakins, J. D. and Morrison, R. T.: A new procedure for the determination of lead-210 in lake and marine sediments, *Int. J. Appl. Radiat. Isot.*, 29, 531–536, times Cited: 205, 1978.
- Eckhardt, S., Stohl, A., Wernli, H., James, P., Forster, C., and Spichtinger, N.: A 15-year climatology of warm conveyor belts, *J. Climate*, 17, 218–237, times Cited: 79, 2004.
- Evans, M. and Jacob, D. J.: Impact of new laboratory studies of N_2O_5 hydrolysis on global model budgets of tropospheric nitrogen oxides, ozone, and OH, *Geophysical Research Letters*, 32, 2005.
- Fehsenfeld, F. C., Daum, P., Leaitch, W. R., Trainer, M., Parrish, D. D., and Hubler, G.: Transport and processing of O-3 and O-3 precursors over the North Atlantic: An overview of the 1993 North Atlantic Regional Experiment (NARE) summer intensive, *J. Geophys. Res.*, 101, 28 877–28 891, doi:10.1029/2006JD007829, 1996.

- Fehsenfeld, F. C., Ancellet, G., Bates, T. S., Goldstein, A. H., Hardesty, R. M., Honrath, R., Law, K. S., Lewis, A. C., Leaitch, R., McKeen, S., Meagher, J., Parrish, D. D., Pszenny, A. A. P., Russell, P. B., Schlager, H., Seinfeld, J., Talbot, R., and Zbinden, R.: International Consortium for Atmospheric Research on Transport and Transformation (ICARTT): North America to Europe - Overview of the 2004 summer field study, *J. Geophys. Res.*, 111, D23S01, doi:10.1029/2006JD007829, 2006.
- Fialho, P., Hansen, A., and Honrath, R.: Absorption coefficients by aerosols in remote areas: a new approach to decouple dust and black carbon absorption coefficients using seven-wavelength Aethalometer data, *Journal of Aerosol Science*, 36, 267–282, 2005.
- Fischer, E. V., Talbot, R. W., Dibb, J. E., Moody, J. L., and Murray, G. L.: Summertime ozone at Mount Washington: Meteorological controls at the highest peak in the northeast, *Journal of Geophysical Research: Atmospheres* (1984–2012), 109, 2004.
- Fischer, E. V., Jaffe, D. A., and Weatherhead, E. C.: Free tropospheric peroxyacetyl nitrate (PAN) and ozone at Mount Bachelor: potential causes of variability and timescale for trend detection, *Atmos. Chem. Phys.*, 11, 5641–5654, 2011.
- Fishman, J. and Seiler, W.: Correlative nature of ozone and carbon monoxide in the troposphere: Implications for the tropospheric ozone budget, *J. Geophys. Res.*, 88, 3662–3670, doi:10.1029/JC088iC06p03662, 1983.
- Gaffney, J. S., Marley, N. A., and Cunningham, M. M.: Natural radionuclides in fine aerosols in the Pittsburgh area, *Atmos. Environ.*, 38, 3191–3200, times Cited: 19, 2004.
- GDAS: NCEP Global Data Assimilation System, URL <http://ready.arl.noaa.gov/gdas1.php>, accessed: Nov. 2014, 2014.
- Giorgi, F. and Chameides, W. L.: Rainout lifetimes of highly soluble aerosols and gases as inferred from simulations with a general circulation model, *Journal of Geophysical Research: Atmospheres* (1984–2012), 91, 14 367–14 376, 1986.
- Guerova, G., Bey, I., Attie, J. L., Martin, R. V., Cui, J., and Sprenger, M.: Impact of transatlantic transport episodes on summertime ozone in Europe, *Atmos. Chem. Phys.*, 6, 2057–2072, 2006.
- Hammer, S., Wagenbach, D., Preunkert, S., Pio, C., Schlosser, C., and Meinhardt, F.: Lead-210 observations within CARBOSOL: A diagnostic tool for assessing the spatiotemporal variability of related chemical aerosol species?, *J. Geophys. Res.*, 112, times Cited: 5, 2007.

- Heald, C. L., Jacob, D. J., Park, R. J., Alexander, B., Fairlie, T. D., Yantosca, R. M., and Chu, D. A.: Transpacific transport of Asian anthropogenic aerosols and its impact on surface air quality in the United States, *Journal of Geophysical Research: Atmospheres* (1984–2012), 111, 2006.
- Hegarty, J., Mao, H., and Talbot, R.: Synoptic influences on springtime tropospheric O(3) and CO over the North American export region observed by TES, *Atmos. Chem. Phys.*, 9, 3755–3776, 2009.
- Helmig, D., Tanner, D. M., Honrath, R. E., Owen, R. C., and Parrish, D. D.: Non-methane hydrocarbons at Pico Mountain, Azores: 1. Oxidation chemistry in the North Atlantic region, *J. Geophys. Res.*, 113, times Cited: 8, 2008.
- Hertel, O., Christensen, J., Runge, E. H., Asman, W. A. H., Berkowicz, R., Hovmand, M. F., and Hov, O.: DEVELOPMENT AND TESTING OF A NEW VARIABLE SCALE AIR-POLLUTION MODEL - ACDEP, *Atmos. Environ.*, 29, 1267–1290, times Cited: 55, 1995.
- Holton, J. R., Haynes, P. H., McIntyre, M. E., Douglass, A. R., Rood, R. B., and Pfister, L.: Stratosphere-troposphere exchange, *Reviews of Geophysics*, 33, 403–439, 1995.
- Honrath, R. E., Owen, R. C., Val Martin, M., Reid, J. S., Lapina, K., Fialho, P., Dziobak, M. P., Kleissl, J., and Westphal, D. L.: Regional and hemispheric impacts of anthropogenic and biomass burning emissions on summertime CO and O3 in the North Atlantic lower free troposphere, *J. Geophys. Res.*, 109, D24 310, doi: 10.1029/2004JD005147, 2004.
- Honrath, R. E., Helmig, D., Owen, R. C., Parrish, D. D., and Tanner, D. M.: Non-methane hydrocarbons at Pico Mountain, Azores: 2. Event-specific analyses of the impacts of mixing and photochemistry on hydrocarbon ratios, *J. Geophys. Res.*, 113, D20S92–, URL <http://dx.doi.org/10.1029/2008JD009832>, 2008.
- Hopkins, J., Jones, I., Lewis, A., McQuaid, J., and Seakins, P.: Non-methane hydrocarbons in the Arctic boundary layer, *Atmospheric Environment*, 36, 3217–3229, 2002.
- Huang, Y., Wu, S., Dubey, M., and French, N.: Impact of aging mechanism on model simulated carbonaceous aerosols, *Atmos. Chem. Phys.*, 13, 6329–6343, 2013.
- Hudman, R. C., Jacob, D. J., Cooper, O. R., Evans, M. J., Heald, C. L., Park, R. J., Fehsenfeld, F., Flocke, F., Holloway, J., Hubler, G., Kita, K., Koike, M., Kondo, Y., Neuman, A., Nowak, J., Oltmans, S., Parrish, D., Roberts, J. M., and Ryerson, T.: Ozone production in transpacific Asian pollution plumes and implications for ozone air quality in California, *J. Geophys. Res.*, 109, 2004.

- Hudman, R. C., Jacob, D. J., Turquety, S., Leibensperger, E. M., Murray, L. T., Wu, S., Gilliland, A. B., Avery, M., Bertram, T. H., Brune, W., Cohen, R. C., Dibb, J. E., Flocke, F. M., Fried, A., Holloway, J., Neuman, J. A., Orville, R., Perring, A., Ren, X., Sachse, G. W., Singh, H. B., Swanson, A., and Wooldridge, P. J.: Surface and lightning sources of nitrogen oxides over the United States: Magnitudes, chemical evolution, and outflow, *J. Geophys. Res.*, 112, 14, 2007.
- Hudman, R. C., Murray, L. T., Jacob, D. J., Turquety, S., Wu, S., Millet, D. B., Avery, M., Goldstein, A. H., and Holloway, J.: North American influence on tropospheric ozone and the effects of recent emission reductions: Constraints from ICARTT observations, *J. Geophys. Res.*, 114, D07302, doi:10.1029/2008JD010126, 2009.
- Huntrieser, H., Heland, J., Schlager, H., Forster, C., Stohl, A., Aufmhoff, H., Arnold, F., Scheel, H. E., Campana, M., Gilge, S., Eixmann, R., and Cooper, O.: Intercontinental air pollution transport from North America to Europe: Experimental evidence from airborne measurements and surface observations, *J. Geophys. Res.*, 110, times Cited: 41, 2005.
- IPCC: Climate Change 2014: Impacts, Adaptation, and Vulnerability. Part A: Global and Sectoral Aspects. Contribution of Working Group II to the Fifth Assessment Report of the Intergovernmental Panel on Climate Change, 2014.
- Jacob, D. J., Logan, J. A., Yevich, R. M., Gardner, G. M., Spivakovsky, C. M., Wofsy, S. C., Munger, J. W., Sillman, S., Prather, M. J., Rodgers, M. O., Westberg, H., and Zimmerman, P. R.: Simulation of summertime ozone over North America, *J. Geophys. Res.*, 98, 14797–14816, doi:10.1029/93JD01223, 1993.
- Jacobson, M. Z. and Turco, R. P.: SMVGEAR: A sparse-matrix, vectorized Gear code for atmospheric models, *Atmos. Environ.*, 28, 273–284, 1994.
- Jaffe, D.: Relationship between surface and free tropospheric ozone in the western US, *Environmental science & technology*, 45, 432–438, 2010.
- Jaffe, D. A. and Wigder, N. L.: Ozone production from wildfires: A critical review, *Atmospheric Environment*, 51, 1–10, 2012.
- Kaiser, J. W., Heil, A., Andreae, M. O., Benedetti, A., Chubarova, N., Jones, L., Morcrette, J.-J., Razinger, M., Schultz, M. G., Suttie, M., and van der Werf, G. R.: Biomass burning emissions estimated with a global fire assimilation system based on observed fire radiative power, *Biogeosciences*, 9, 527–554, 2012.
- Kim, G., Hussain, N., and Church, T. M.: Excess ^{210}Po in the coastal atmosphere, *Tellus B*, 52, 74–80, 2000.
- Kim, G., Hong, Y.-L., Jang, J., Lee, I., Hwang, D.-W., and Yang, H.-S.: Evidence for anthropogenic ^{210}Po in the urban atmosphere of Seoul, Korea, *Environmental science & technology*, 39, 1519–1522, 2005.

- Kim, P., Jacob, D., Liu, X., Warner, J., Yang, K., Chance, K., Thouret, V., and Nedelec, P.: Global ozone–CO correlations from OMI and AIRS: constraints on tropospheric ozone sources, *Atmospheric Chemistry and Physics*, 13, 9321–9335, 2013.
- Kleindienst, T. E.: Recent developments in the chemistry and biology of peroxyacetyl nitrate, *Res. Chem. Intermed.*, 20, 335–384, doi:10.1163/156856794X00379, 1994.
- Kleissl, J., Honrath, R. E., Dziobak, M. P., Tanner, D., Martin, M. V., Owen, R. C., and Helmig, D.: Occurrence of upslope flows at the Pico mountaintop observatory: A case study of orographic flows on a small, volcanic island, *J. Geophys. Res.*, 112, D10S35, doi:10.1029/2006JD007565, 2007.
- Kotchenruther, R. A., Jaffe, D. A., and Jaegle, L.: Ozone photochemistry and the role of peroxyacetyl nitrate in the springtime northeastern Pacific troposphere: Results from the Photochemical Ozone Budget of the Eastern North Pacific Atmosphere (PHOBEA) campaign, *J. Geophys. Res.*, 106, 28 731–28 742, doi: 10.1029/2000JD000060, 2001.
- Kraemer, T. F.: Radon in unconventional natural gas from Gulf coast geopressured-geothermal reservoirs, *Environ. Sci. Technol.*, 20, 939–942, 1986.
- Kumar, A., Wu, S., Weise, M., Honrath, R., Owen, R., Helmig, D., Kramer, L., Val Martin, M., and Li, Q.: Free-troposphere ozone and carbon monoxide over the North Atlantic for 2001–2011, *Atmospheric Chemistry and Physics*, 13, 12 537–12 547, 2013.
- Lambert, G., Le Cloarec, M., Ardouin, B., and Le Roulley, J.: Volcanic emission of radionuclides and magma dynamics, *Earth and planetary science letters*, 76, 185–192, 1985.
- Lapina, K., Honrath, R. E., Owen, R. C., Martin, M. V., and Pfister, G.: Evidence of significant large-scale impacts of boreal fires on ozone levels in the midlatitude Northern Hemisphere free troposphere, *Geophys. Res. Lett.*, 33, L10 815, doi:10.1029/2006GL025878, 2006.
- Lee, S. H., Kim, S. W., Trainer, M., Frost, G. J., McKeen, S. A., Cooper, O. R., Flocke, F., Holloway, J. S., Neuman, J. A., Ryerson, T., Senff, C. J., Swanson, A. L., and Thompson, A. M.: Modeling ozone plumes observed downwind of New York City over the North Atlantic Ocean during the ICARTT field campaign, *Atmos. Chem. Phys.*, 11, 7375–7397, 2011.
- Li, Q. B., Jacob, D. J., Bey, I., Palmer, P. I., Duncan, B. N., Field, B. D., Martin, R. V., Fiore, A. M., Yantosca, R. M., Parrish, D. D., Simmonds, P. G., and Oltmans, S. J.: Transatlantic transport of pollution and its effects on surface ozone in Europe and North America, *J. Geophys. Res.*, 107, times Cited: 106, 2002a.

- Li, Q. B., Jacob, D. J., Fairlie, T. D., Liu, H. Y., Martin, R. V., and Yantosca, R. M.: Stratospheric versus pollution influences on ozone at Bermuda: Reconciling past analyses, *J. Geophys. Res.*, 107, times Cited: 31, 2002b.
- Li, Q. B., Jacob, D. J., Munger, J. W., Yantosca, R. M., and Parrish, D. D.: Export of NO_y from the North American boundary layer: Reconciling aircraft observations and global model budgets, *J. Geophys. Res.*, 109, times Cited: 42, 2004.
- Li, Q. B., Jacob, D. J., Park, R., Wang, Y. X., Heald, C. L., Hudman, R., Yantosca, R. M., Martin, R. V., and Evans, M.: North American pollution outflow and the trapping of convectively lifted pollution by upper-level anticyclone, *J. Geophys. Res.*, 110, times Cited: 67, 2005.
- Liang, J. Y., Horowitz, L. W., Jacob, D. J., Wang, Y. H., Fiore, A. M., Logan, J. A., Gardner, G. M., and Munger, J. W.: Seasonal budgets of reactive nitrogen species and ozone over the United States, and export fluxes to the global atmosphere, *J. Geophys. Res.*, 103, 13 435–13 450, times Cited: 89, 1998.
- Liang, Q., Jaegle, L., Jaffe, D. A., Weiss-Penzias, P., Heckman, A., and Snow, J. A.: Long-range transport of Asian pollution to the northeast Pacific: Seasonal variations and transport pathways of carbon monoxide, *J. Geophys. Res.*, 109, times Cited: 81, 2004.
- Liang, Q., Rodriguez, J. M., Douglass, A. R., Crawford, J. H., Olson, J. R., Apel, E., Bian, H., Blake, D. R., Brune, W., Chin, M., Colarco, P. R., da Silva, A., Diskin, G. S., Duncan, B. N., Huey, L. G., Knapp, D. J., Montzka, D. D., Nielsen, J. E., Pawson, S., Riemer, D. D., Weinheimer, A. J., and Wisthaler, A.: Reactive nitrogen, ozone and ozone production in the Arctic troposphere and the impact of stratosphere-troposphere exchange, *Atmospheric Chemistry and Physics*, 11, 13 181–13 199, 2011.
- Liu, H., Jacob, D. J., Bey, I., and Yantosca, R. M.: Constraints from ²¹⁰Pb and ⁷Be on wet deposition and transport in a global three-dimensional chemical tracer model driven by assimilated meteorological fields, *Journal of Geophysical Research: Atmospheres* (1984–2012), 106, 12 109–12 128, 2001.
- Liu, S. C., Trainer, M., Fehsenfeld, F. C., Parrish, D. D., Williams, E. J., Fahey, D. W., Hubler, G., and Murphy, P. C.: Ozone production in the rural troposphere and the implications for regional and global ozone distributions, *J. Geophys. Res.*, 92, 4191?4207, doi:10.1029/JD092iD04p04191, 1987.
- Logan, J. A.: An analysis of ozonesonde data for the lower stratosphere: Recommendations for testing models, *J. Geophys. Res.*, 104, 16 151–16 170, iSI Document Delivery No.: 218CE Times Cited: 54 Cited Reference Count: 82 Logan, JA AMER GEOPHYSICAL UNION WASHINGTON, 1999.

- Logan, J. A., Prather, M. J., Wofsy, S. C., and McElroy, M. B.: Tropospheric chemistry: A global perspective, *Journal of Geophysical Research: Oceans* (1978–2012), 86, 7210–7254, 1981a.
- Logan, J. A., Prather, M. J., Wofsy, S. C., and McElroy, M. B.: Tropospheric chemistry: A global perspective, *Journal of Geophysical Research: Oceans* (1978–2012), 86, 7210–7254, 1981b.
- Macdonald, A., Anlauf, K., Leaitch, W., Chan, E., and Tarasick, D.: Interannual variability of ozone and carbon monoxide at the Whistler high elevation site: 2002–2006, *Atmos. Chem. Phys.*, 11, 11 431–11 446, 2011.
- Mahlman, J., Levy, H., and Moxim, W.: Three-dimensional tracer structure and behavior as simulated in two ozone precursor experiments, *Journal of the Atmospheric Sciences*, 37, 655–685, 1980.
- Mao, H., Talbot, R., Troop, D., Johnson, R., Businger, S., and Thompson, A. M.: Smart balloon observations over the North Atlantic: O³ data analysis and modeling, *J. Geophys. Res.*, 111, D23S56, doi:10.1029/2005JD006507, 2006.
- Mao, H. T. and Talbot, R.: O-3 and CO in New England: Temporal variations and relationships, *J. Geophys. Res.*, 109, 2004.
- Martin, R. V., Jacob, D. J., Logan, J. A., Bey, I., Yantosca, R. M., Staudt, A. C., Li, Q., Fiore, A. M., Duncan, B. N., Liu, H., Ginoux, P., and Thouret, V.: Interpretation of TOMS observations of tropical tropospheric ozone with a global model and in situ observations, *Journal of Geophysical Research: Atmospheres* (1984–2012), 107, ACH-4, 2002.
- McKeen, S. and Liu, S.: Hydrocarbon ratios and photochemical history of air masses, *Geophysical research letters*, 20, 2363–2366, 1993.
- McKeen, S., Wotawa, G., Parrish, D., Holloway, J., Buhr, M., Hübler, G., Fehsenfeld, F., and Meagher, J.: Ozone production from Canadian wildfires during June and July of 1995, *Journal of Geophysical Research: Atmospheres* (1984–2012), 107, ACH-7, 2002.
- McNeary, D. and Baskaran, M.: Residence times and temporal variations of ²¹⁰Po in aerosols and precipitation from southeastern Michigan, United States, *Journal of Geophysical Research: Atmospheres* (1984–2012), 112, 2007.
- Millet, D. B., Goldstein, A. H., Holzinger, R., Williams, B. J., Allan, J. D., Jimenez, J. L., Worsnop, D. R., Roberts, J. M., White, A. B., Hudman, R. C., Bertschi, I. T., and Stohl, A.: Chemical characteristics of North American surface layer outflow: Insights from Chebogue Point, Nova Scotia, *J. Geophys. Res.*, 111, 15, iSI Document Delivery No.: 081RK Times Cited: 45 Cited Reference Count: 77

- Millet, Dylan B. Goldstein, Allen H. Holzinger, Rupert Williams, Brent J. Allan, James D. Jimenez, Jose L. Worsnop, Douglas R. Roberts, James M. White, Allen B. Hudman, Rynda C. Bertschi, Isaac T. Stohl, Andreas AMER GEOPHYSICAL UNION WASHINGTON, 2006.
- Mu, M., Randerson, J. T., van der Werf, G. R., Giglio, L., Kasibhatla, P., Morton, D., Collatz, G. J., DeFries, R. S., Hyer, E. J., Prins, E. M., Griffith, D. W. T., Wunch, D., Toon, G. C., Sherlock, V., and Wennberg, P. O.: Daily and 3-hourly variability in global fire emissions and consequences for atmospheric model predictions of carbon monoxide, *J. Geophys. Res.*, 116, D24303, doi:10.1029/2011JD016245, 2011.
- NCAR: Meteorological case study selection kit, URL <http://www.mmm.ucar.edu/imagearchive/>, last accessed: November 2013, 2009.
- Neuman, J. A., Parrish, D. D., Trainer, M., Ryerson, T. B., Holloway, J. S., Nowak, J. B., Swanson, A., Flocke, F., Roberts, J. M., Brown, S. S., Stark, H., Sommariva, R., Stohl, A., Peltier, R., Weber, R., Wollny, A. G., Sueper, D. T., Hubler, G., and Fehsenfeld, F. C.: Reactive nitrogen transport and photochemistry in urban plumes over the North Atlantic Ocean, *J. Geophys. Res.*, 111, D23S54, doi:10.1029/2005JD007010, 2006.
- Neuman, J. A., Trainer, M., Aikin, K. C., Angevine, W. M., Brioude, J., Brown, S. S., de Gouw, J. A., Dube, W. P., Flynn, J. H., Graus, M., Holloway, J. S., Lefer, B. L., Nedelec, P., Nowak, J. B., Parrish, D. D., Pollack, I. B., Roberts, J. M., Ryerson, T. B., Smit, H., Thouret, V., and Wagner, N. L.: Observations of ozone transport from the free troposphere to the Los Angeles basin, *Journal of Geophysical Research: Atmospheres* (1984–2012), 117, 2012.
- Nevissi, A. E.: MEASUREMENT OF PB-210, BI-210, AND PO-210 IN ENVIRONMENTAL-SAMPLES, *Journal of Radioanalytical and Nuclear Chemistry-Articles*, 148, 121–131, times Cited: 18, 1991.
- Nho, E.-Y., Ardouin, B., Le Cloarec, M., and Ramonet, M.: Origins of ²¹⁰Po in the atmosphere at Lamto, Ivory Coast: Biomass burning and Saharan dusts, *Atmospheric Environment*, 30, 3705–3714, 1996.
- Olivier, J. and Berdowski, J.: *The Climate System*, chap. Global emission sources and sinks, pp. 33–78, A.A. Balkema, Swets & Zeitlinger, ISBN 9058092550, 2001.
- Owen, R.: A Climatological Study of Transport to the PICO-NARE Site Using Atmospheric Backward Trajectories, Master's thesis, Michigan Technological University, 2003.
- Owen, R.: Long-range pollution transport: Trans-Atlantic mechanisms and Lagrangian modeling methods, Ph.D. thesis, Michigan Technological University, 2009.

- Owen, R. C. and Honrath, R. E.: Technical note: a new method for the Lagrangian tracking of pollution plumes from source to receptor using gridded model output, *Atmos. Chem. Phys.*, 9, 2577–2595, 2009.
- Owen, R. C., Cooper, O. R., Stohl, A., and Honrath, R. E.: An analysis of the mechanisms of North American pollutant transport to the central North Atlantic lower free troposphere, *J. Geophys. Res.*, 111, D23S58, doi:10.1029/2006JD007062, 2006.
- Papastefanou, C.: Residence time of tropospheric aerosols in association with radioactive nuclides, *Applied Radiation and Isotopes*, 64, 93–100, 2006.
- Parrington, M., Palmer, P. I., Lewis, A. C., Lee, J. D., Rickard, A. R., Di Carlo, P., Taylor, J. W., Hopkins, J. R., Punjabi, S., Oram, D. E., Forster, G., Aruffo, E., Moller, S. J., Bauguutte, S. J.-B., Allan, J. D., Coe, H., and Leigh, R. J.: Ozone photochemistry in boreal biomass burning plumes, 13, 7321–7341, 2013.
- Parrish, D., Aikin, K., Oltmans, S., Johnson, B., Ives, M., and Sweeny, C.: Impact of transported background ozone inflow on summertime air quality in a California ozone exceedance area, *Atmospheric Chemistry and Physics*, 10, 10 093–10 109, 2010.
- Parrish, D. D., Hahn, C. J., Williams, E. J., Norton, R. B., Fehsenfeld, F. C., Singh, H. B., Shetter, J. D., Gandrud, B. W., and Ridley, B. A.: Indications of photochemical histories of Pacific air masses from measurements of atmospheric trace species at Point Arena, California, *J. Geophys. Res.*, 97, 15 883–15 901, 1992.
- Parrish, D. D., Holloway, J. S., Trainer, M., Murphy, P. C., Forbes, G. L., and Fehsenfeld, F. C.: Export of North American ozone pollution to the north Atlantic Ocean, *Science*, 259, 1436–1439, doi:10.1126/science.259.5100.1436, 1993.
- Parrish, D. D., Trainer, M., Holloway, J. S., Yee, J. E., Warshawsky, M. S., Fehsenfeld, F. C., Forbes, G. L., and Moody, J. L.: Relationships between ozone and carbon monoxide at surface sites in the North Atlantic region, *J. Geophys. Res.*, 103, 13 357–13 376, doi:10.1029/98JD00376, 1998.
- Parrish, D. D., Stohl, A., Forster, C., Atlas, E. L., Blake, D. R., Goldan, P. D., Kuster, W. C., and de Gouw, J. A.: Effects of mixing on evolution of hydrocarbon ratios in the troposphere, *J. Geophys. Res.*, 112, times Cited: 32, 2007.
- Parrish, D. D., Law, K. S., Staehelin, J., Derwent, R., Cooper, O. R., Tanimoto, H., Volz-Thomas, A., Gilge, S., Scheel, H.-E., Steinbacher, M., and Chan, E.: Long-term changes in lower tropospheric baseline ozone concentrations at northern mid-latitudes, *Atmospheric Chemistry and Physics*, 12, 11 485–11 504, doi: 10.5194/acp-12-11485-2012, URL <http://www.atmos-chem-phys.net/12/11485/2012/>, 2012.

- Petroff, A. and Zhang, L.: Development and validation of a size-resolved particle dry deposition scheme for application in aerosol transport models, *Geoscientific Model Development*, 3, 753–769, 2010.
- Pfister, G. G., Emmons, L. K., Hess, P. G., Honrath, R., Lamarque, J.-F., Val Martin, M., Owen, R. C., Avery, M. A., Browell, E. V., Holloway, J. S., Nedelec, P., Purvis, R., Ryerson, T. B., Sachse, G. W., and Schlager, H.: Ozone production from the 2004 North American boreal fires, *Journal of Geophysical Research: Atmospheres* (1984–2012), 111, 2006.
- Poet, S., Moore, H., and Martell, E.: Lead 210, bismuth 210, and polonium 210 in the atmosphere: accurate ratio measurement and application to aerosol residence time determination, *Journal of Geophysical Research*, 77, 6515–6527, 1972.
- Prados, A., Dickerson, R., Doddridge, B., Milne, P., Moody, J., and Merrill, J.: Transport of ozone and pollutants from North America to the North Atlantic Ocean during the 1996 Atmosphere/Ocean Chemistry Experiment (AEROCE) intensive, *Journal of Geophysical Research: Atmospheres* (1984–2012), 104, 26 219–26 233, 1999.
- Price, H. U., Jaffe, D. A., Cooper, O. R., and Doskey, P. V.: Photochemistry, ozone production, and dilution during long-range transport episodes from Eurasia to the northwest United States, *J. Geophys. Res.*, 109, times Cited: 37, 2004.
- Ram, K. and Sarin, M.: Atmospheric ^{210}Pb , ^{210}Po and $^{210}\text{Po}/^{210}\text{Pb}$ activity ratio in urban aerosols: temporal variability and impact of biomass burning emission, *Tellus B*, 64, 2012.
- Ramanathan, V. and Carmichael, G.: Global and regional climate changes due to black carbon, *Nature geoscience*, 1, 221–227, 2008.
- Real, E., Law, K. S., Weinzierl, B., Fiebig, M., Petzold, A., Wild, O., Methven, J., Arnold, S., Stohl, A., Huntrieser, H., Roiger, A., Schlager, H., Stewart, D., Avery, M., Sachse, G., Browell, E., Ferrare, R., and Blake, D.: Processes influencing ozone levels in Alaskan forest fire plumes during long-range transport over the North Atlantic, *J. Geophys. Res.*, 112, 19, iSI Document Delivery No.: 168AS Times Cited: 47 Cited Reference Count: 60 Real, E. Law, K. S. Weinzierl, B. Fiebig, M. Petzold, A. Wild, O. Methven, J. Arnold, S. Stohl, A. Huntrieser, H. Roiger, A. Schlager, H. Stewart, D. Avery, M. Sachse, G. Browell, E. Ferrare, R. Blake, D. AMER GEOPHYSICAL UNION WASHINGTON, 2007.
- Real, E., Law, K. S., Schlager, H., Roiger, A., Huntrieser, H., Methven, J., Cain, M., Holloway, J., Neuman, J. A., Ryerson, T., Flocke, F., de Gouw, J., Atlas, E., Donnelly, S., and Parrish, D.: Lagrangian analysis of low altitude anthropogenic plume processing across the North Atlantic, *Atmos. Chem. Phys.*, 8, 7737–7754, 2008.

- Reeves, C. E., Penkett, S. A., Bauguitte, S., Law, K. S., Evans, M. J., Bandy, B. J., Monks, P. S., Edwards, G. D., Phillips, G., Barjat, H., Kent, J., Dewey, K., Schmitgen, S., and Kley, D.: Potential for photochemical ozone formation in the troposphere over the North Atlantic as derived from aircraft observations during ACSOE, *J. Geophys. Res.*, 107, 4707, doi:10.1029/2002JD002415, 2002.
- R. Johnson, C.: Matrix theory and applications, the American Mathematical Society, Phoenix, Arizona, USA, 1989.
- Seibert, P. and Frank, A.: Source-receptor matrix calculation with a Lagrangian particle dispersion model in backward mode, *Atmos. Chem. Phys.*, 4, 51–63, 2004.
- Sheppard, P.: Airflow over mountains, *Quart. J. Roy. Meteor. Soc.*, 82, 528–529, 1956.
- Spivakovsky, C., Yevich, R., Logan, J., Wofsy, S., McElroy, M., and Prather, M.: Tropospheric OH in a three-dimensional chemical tracer model: An assessment based on observations of CH₃CCl₃, *Journal of Geophysical Research: Atmospheres* (1984–2012), 95, 18 441–18 471, 1990.
- Stier, P., Feichter, J., Kinne, S., Kloster, S., Vignati, E., Wilson, J., Ganzeveld, L., Tegen, I., Werner, M., Balkanski, Y., Schulz, M., Boucher, O., Minikin, A., and Petzold, A.: The aerosol-climate model ECHAM5-HAM, 5, 1125–1156, 2005.
- Stohl, A., Hittenberger, M., and Wotawa, G.: Validation of the Lagrangian particle dispersion model FLEXPART against large-scale tracer experiment data, *Atmos. Environ.*, 32, 4245–4264, doi:10.1016/S1352-2310(98)00184-8, 1998.
- Stohl, A., Eckhardt, S., Forster, C., James, P., and Spichtinger, N.: On the pathways and timescales of intercontinental air pollution transport, *J. Geophys. Res.*, 107, 4684, doi:10.1029/2001JD001396, times Cited: 140, 2002.
- Stohl, A., Sodemann, H., Eckhardt, S., Frank, A., Seibert, P., and Wotawa, G.: The Lagrangian particle dispersion model FLEXPART version 8.2, FLEXPART user guide, url: <http://zardoz.nilu.no/flexpart/flexpart/flexpart82.pdf> (March 14, 2012), 2011.
- Streets, D. G., Bond, T. C., Carmichael, G. R., Fernandes, S. D., Fu, Q., He, D., Klimont, Z., Nelson, S. M., Tsai, N. Y., Wang, M. Q., Woo, J.-H., and Yarber, K. F.: An inventory of gaseous and primary aerosol emissions in Asia in the year 2000, *J. Geophys. Res.*, 108, 8809–, URL <http://dx.doi.org/10.1029/2002JD003093>, 2003.
- Thompson, A. M.: The Oxidizing Capacity of the Earth's Atmosphere: Probable Past and Future Changes, *Science*, 256, 1157–1165, doi:10.1126/science.256.5060.1157, URL <http://www.sciencemag.org/content/256/5060/1157.abstract>, 1992.

- Turekian, K. Y., Nozaki, Y., and Benninger, L. K.: Geochemistry of atmospheric radon and radon products, *Annual Review of Earth and Planetary Sciences*, 5, 227, 1977.
- Val Martín, M., Honrath, R. E., Owen, R. C., Pfister, G., Fialho, P., and Barata, F.: Significant enhancements of nitrogen oxides, black carbon, and ozone in the North Atlantic lower free troposphere resulting from North American boreal wildfires, *J. Geophys. Res.*, 111, D23S60, doi:10.1029/2006JD007530, 2006.
- Val Martín, M., Honrath, R. E., Owen, R. C., and Lapina, K.: Large-scale impacts of anthropogenic pollution and boreal wildfires on the nitrogen oxides over the central North Atlantic region, *J. Geophys. Res.*, 113, 2008a.
- Val Martín, M., Honrath, R. E., Owen, R. C., and Li, Q. B.: Seasonal variation of nitrogen oxides in the central North Atlantic lower free troposphere, *J. Geophys. Res.*, 113, D17307, doi:10.1029/2007JD009688, 2008b.
- Verma, S., Worden, J., Pierce, B., Jones, D. B. A., Al-Saadi, J., Boersma, F., Bowman, K., Eldering, A., Fisher, B., Jourdain, L., Kulawik, S., and Worden, H.: Ozone production in boreal fire smoke plumes using observations from the Tropospheric Emission Spectrometer and the Ozone Monitoring Instrument, *Journal of Geophysical Research: Atmospheres* (1984–2012), 114, 2009.
- Voulgarakis, A., Telford, P. J., Aghedo, A. M., Braesicke, P., Faluvegi, G., Abraham, N. L., Bowman, K. W., Pyle, J. A., and Shindell, D. T.: Global multi-year O₃-CO correlation patterns from models and TES satellite observations, *Atmos. Chem. Phys.*, 11, 5819–5838, 2011.
- Wang, H., Jacob, D. J., Le Sager, P., Streets, D. G., Park, R. J., Gilliland, A. B., and Van Donkelaar, A.: Surface ozone background in the United States: Canadian and Mexican pollution influences, *Atmospheric Environment*, 43, 1310–1319, 2009.
- Wang, Y., Jacob, D., and Logan, J.: Global simulation of tropospheric O₃-NO_x-hydrocarbon chemistry 3. Origin of tropospheric ozone and effects of nonmethane hydrocarbons, *Journal of Geophysical Research. D. Atmospheres*, 103, 10, 1998a.
- Wang, Y. H., Jacob, D. J., and Logan, J. A.: Global simulation of tropospheric O₃-NO_x-hydrocarbon chemistry 1. Model formulation, *J. Geophys. Res.*, 103, 10713–10725, doi:10.1029/98JD00158, 1998b.
- Wang, Z., Yang, W., Chen, M., Lin, P., and Qiu, Y.: Intra-Annual Deposition of Atmospheric ²¹⁰Pb, ²¹⁰Po and the Residence Times of Aerosol in Xiamen, China, *Aerosol and Air Quality Research*, 14, doi:10.4209/aaqr.2013.05.0170, 2014.

- Weise, M.: Tropospheric ozone and CO over North Atlantic for the past decade, Master's thesis, 2011.
- Wesely, M. L.: PARAMETERIZATION OF SURFACE RESISTANCES TO GASEOUS DRY DEPOSITION IN REGIONAL-SCALE NUMERICAL-MODELS, *Atmos. Environ.*, 23, 1293–1304, times Cited: 619, 1989.
- Whittlestone, S.: Radon daughter disequilibria in the lower marine boundary layer, *J. Atmos. Chem.*, 11, 27–42, 1990.
- Wild, O., Law, K. S., McKenna, D. S., Bandy, B. J., Penkett, S. A., and Pyle, J. A.: Photochemical trajectory modeling studies of the North Atlantic region during August 1993, *J. Geophys. Res.*, 101, 29 269–29 288, iSI Document Delivery No.: VZ788 Times Cited: 49 Cited Reference Count: 33 Wild, O Law, KS McKenna, DS Bandy, BJ Penkett, SA Pyle, JA AMER GEOPHYSICAL UNION WASHINGTON, 1996.
- Worden, H. M., Deeter, M. N., Frankenberg, C., George, M., Nichitiu, F., Worden, J., Aben, I., Bowman, K. W., Clerbaux, C., Coheur, P. F., de Laat, A. T. J., Detweiler, R., Drummond, J. R., Edwards, D. P., Gille, J. C., Hurtmans, D., Luo, M., Martínez-Alonso, S., Massie, S., Pfister, G., and Warner, J. X.: Decadal record of satellite carbon monoxide observations, *Atmospheric Chemistry and Physics*, 13, 837–850, 2013.
- Wu, S., Mickley, L. J., Jacob, D. J., Logan, J. A., Yantosca, R. M., and Rind, D.: Why are there large differences between models in global budgets of tropospheric ozone?, *Journal of Geophysical Research: Atmospheres* (1984–2012), 112, 2007.
- Zhang, B., Owen, R. C., Perlinger, J., Kumar, A., Wu, S., Val Martin, M., Kramer, L., Helmig, D., and Honrath, R.: A semi-Lagrangian view of ozone production tendency in North American outflow in the summers of 2009 and 2010, *Atmospheric Chemistry and Physics*, 14, 2267–2287, 2014.
- Zhang, L., Jacob, D. J., Bowman, K. W., Logan, J. A., Turquety, S., Hudman, R. C., Li, Q., Beer, R., Worden, H. M., Worden, J. R., Rinsland, C. P., Kulawik, S. S., Lampel, M. C., Shephard, M. W., Fisher, B. M., Eldering, A., and Avery, M. A.: Ozone-CO correlations determined by the TES satellite instrument in continental outflow regions, *Geophys. Res. Lett.*, 33, L18 804, doi:10.1029/2006GL026399, 2006.
- Zhang, L., Jacob, D. J., Boersma, K. F., Jaffe, D. A., Olson, J. R., Bowman, K. W., Worden, J. R., Thompson, A. M., Avery, M. A., Cohen, R. C., Dibb, J. E., Flock, F. M., Fuelberg, H. E., Huey, L. G., McMillan, W. W., Singh, H. B., and Weinheimer, A. J.: Transpacific transport of ozone pollution and the effect of recent Asian emission increases on air quality in North America: an integrated analysis using satellite, aircraft, ozonesonde, and surface observations, *Atmos. Chem. Phys.*, 8, 6117–6136, 2008.

Appendix A

Technical instructions for running FLEXPART 8.2

Detailed instructions of running FLEXPART6.2 can be found in a previous dissertation (Owen, 2009). The newer version, FLEXPART8.2, has a Fortran package in the same structure as FLEXPART6.2. (Owen, 2009) explains the structure, options and the input files in detail. Additional modifications that are necessary for running FLEXPART8.2 are introduced here. It is suggested that users should read Owen (2009), Appendix A, prior to the following instructions. An online discussion forum (<http://www.flexpart.eu/>) can be used for searching for help. All modified files and IDL programs are stored on a disk, which is attached with this dissertation.

A.1 Setup

Stohl et al. (2011) provides the steps of setting up FLEXPART8.2 on a Linux machine, including sources and install instructions of required software/libraries. Users are required to read Stohl et al. (2011) to have a general idea of the model. Brioude et al. (2013), which is dedicated to FLEXPART-WRF, discusses the numerical schemes used in FLEXPART. These two documents are very helpful for understanding the work flows and calculations in FLEXPART, but they are not necessary for running FLEXPART on a machine with all required software/libraries installed already. FLEXPART source codes can be found at <http://www.flexpart.eu/>.

The easiest approach for running FLEXPART is to obtain the modified Fortran package from:

/local/reh/bzhang/flex_run/flexpart822_use1-4 (for standard backward simulations, running with GFS-grib2 meteorology)

/local/reh/bzhang/flex_run/flexpart822_fore2-4 (for standard forward simulations, running with GFS-grib2 meteorology)

and use the IDL programs below to compile and execute the model. Users will need to re-assign the directory of these packages in the IDL programs. Please see the next section for the modifications.

A.2 Modified files

As an alternative, users are able to obtain FLEXPART 8.2 from the link provided above and overwrite the following files. All the ready-to-use files can be found in the attached disk, under /modified/flexpart822/

concoutput.f

Line 227-253 modified to output formatted files.

Line 257-291, 326-404, 439-474, commented out for model efficiency. No output for wet and dry deposition in standard runs.

Line 484-558 commented out to omit output of mixing ratios.

Line 562-592 modified to write gridded output.

Line 595-630 commented out to omit sparse output.

writeheader.f

Line 107 and 104 modified to output formatted files.

timemanager.f (optional, for instantaneous output)

Line 182-187 modified to give instantaneous output at the end of each interval, which is also the time used for the time stamp on the file.

Line 203 modified to display days as opposed to seconds.

A.3 Meteorology

ECMWF meteorology data has been difficult to get since 2009. This was the main reason for switching from FLEXPART6.2 to FLEXPART8.2. The latter accepts GFS/FNL grib2 data to drive the simulations. The description of this update and required variables in GFS/FNL data can be found in (Stohl et al., 2011).

GFS (Global Forecast System) data are forecast data, which can be obtained from http://nomads.ncdc.noaa.gov/cgi-bin/ncdc-ui/define-collection.pl?model_sys=gfs-hi&model_name=gfs&grid_name=3. The final analyzed version of GFS is FNL (Final Global Analysis), which is better for running historical simulations and can be obtained from <http://rda.ucar.edu/datasets/ds083.2/>. The FNL data are only available for every 6 hours. The users are free to choose either or a combination of GFS and FNL, depending on application.

A IDL program, "write_available_gfs.pro", can be used to generate the AVAILABLE file for FLEXPART.

A.4 IDL programs for running FLEXPART8.2 and visualizing the standard output

IDL programs are used to write input files, compile FLEXPART code, launch the simulation and process model output. All the IDL programs introduced below and functions used therein are stored in the attached disk under /IDL-Workspace71/FLEX_Bo/. The IDL programs were developed based on the ones used for running FLEXPART6.2. Please see Appendices in (Owen, 2009).

A.4.1 Backward simulation

Related programs are:
doit_run_retro_flex8.pro
doit_auto_retro_flex8.pro
brun_retro_flex
bread_retro_flex_output

bconvert_retro_temps_to_gridded_final
doit_bplot_rt_traj_single.pro

The launching program of backward simulation is *doit_rn_retro_flex8.pro*, which compiles the other four programs before starting the simulation.

doit_auto_retro_flex8.pro is the most controlling program and has all the configurations in it. It takes the required information, including input and output directories, simulation periods, and FLEXPART settings. It launches *brun_retro_flex*, *bread_retro_flex_output*, and *bconvert_retro_temps_to_gridded_final* for a complete simulation.

brun_retro_flex compiles and runs FLEXPART. After receiving the information and settings in *doit_auto_retro_flex8.pro*, it writes the input files of FLEXPART (COMMAND, RELEASES, OUTGRID, AGECLASSES, pathnames and includepar). It generates and launches the FLEXPART executable file, "FLEXPART_GFS_GFORTRAN".

bread_retro_flex_output reads the size and length of the FLEXPART output (.txt files) and saves the data in temporary .idlsav files.

bconvert_retro_temps_to_gridded_final reads the temporary .idlsav files, converts the sparse format into gridded format and stores the results as standard FLEXPART retroplume.

doit_bplot_rt_traj_single.pro reads the specific retroplume for a given time and plots the entire transport trajectory in four separate figures, including a map view of column integrated horizontal distribution of residence time, a vertical distribution on a view of upwind days vs. height, a vertical distribution on a view of longitude vs. height and a vertical distribution on a view of latitude vs. height.

A.4.2 Forward simulation

Related programs are:

doit_run_for_flex8.pro
brun_forward_flexpart.pro
bread_forward_flex_output.pro

bconvert_forward_temps_to_gridded_final.pro
bplot_for_traj.pro

doit_run_for_flex8.pro is both the controlling and launching program, where simulation settings are stored. It compiles *brun_forward_flexpart.pro*, *bread_forward_flex_output.pro* and *bconvert_forward_temps_to_gridded_final.pro* and launches them in sequence.

brun_forward_flexpart.pro compiles and runs FLEXPART. After receiving the information and settings in *doit_auto_retro_flex8.pro*, it writes the input files of FLEXPART (COMMAND, RELEASES, OUTGRID, AGECLASSES, pathnames and includepar). It generates and launches the FLEXPART executable file, "FLEXPART_GFS_GFORTRAN".

bread_forward_flex_output.pro reads the size and length of the FLEXPART output (.txt files) and saves the data in temporary .idsav files.

bconvert_forward_temps_to_gridded_final.pro reads the temporary .idsav files, converts the sparse format into gridded format and stores the results as standard FLEXPART retroplume.

bplot_for_traj.pro reads the standard forward simulation results and plots a snapshot of the distribution of released tracer for a given time. Both the map view and vertical view are plotted.

Emission inventories are required for forecasting pollution transport in forward FLEXPART runs. The anthropogenic emission inventory (EDGAR 3.2) was processed and stored in a compatible way to be called by the programs. Future EDGAR emission inventories (<http://edgar.jrc.ec.europa.eu/index.php>) will likely be given in NetCDF format. Users can try to convert it for FLEXPART use by a program developed for EDGAR 4.2 (*IDLWorkbench71/NetCDF/edgar4_2_2_FP_readable.pro*), but no guarantee is given for future release of EDGAR inventories. Wildfire/biomass burning emission can be obtained from GFAS data (http://www.gmes-atmosphere.eu/about/project_structure/input_data/d_fire/). The users may use *IDLWorkbench71/BBemis/get_fire_emis_gfas.pro* to read the GFAS NetCDF file and convert the gridded results to sparse results for FLEXPART forward runs using *IDLWorkbench71/BBemis/data_convert_gfas_to_sparse.pro*.

A.5 Folded FLEXPART

A.5.1 Folding FLEXPART retroplumes with forward results

Related programs are:

cal_fold_retro.pros

For a given time period, *bplot_for_traj.pro* reads the standard retroplume first. It then locates the forward simulation results associated with each time step of the retroplume. The residence time matrix at each time step of the retroplume is multiplied by the tracer concentrations in the forward simulation, which gives the folded results. The results are saved in a similar structure as standard retroplumes, which can be plotted using the programs provided above. For the applications of this product, please see the related analyses in Chapter 2.

A.5.2 Folding FLEXPART retroplumes with emission inventories

Related programs are:

doit_plot_trj_emis_fire_height.pro

doit_plot_trj_emis_fire_height.pro does the folding calculation and plotting in one. The folding calculation requires the retroplume available for the periods of interest and wildfire and anthropogenic emission inventories as given above. This program saves the contributions of pollution tracer (CO as default) from different continents. The results can be visualized by using */IDLWorkbench71/Pico_wiki/plot_tracer_spec_source.pro*. Figures are generated for the whole month that is specified in the program.

Appendix B

Technical requirements for using Sheppard's model

The description of the model can be found in Sheppard (1956) and Kleissl et al. (2007). The application of Sheppard's model requires meteorological profiles at Pico, which can be obtained using the meteorological data driving FLEXPART, and the following libraries, which read the profiles from the meteorological data.

Wgrib2 is a library that can be used to read grib2 data in a Linux environment. The source code and instructions of Wgrib2 can be found at (<http://www.cpc.noaa.gov/products/wesley/wgrib2/>). An IDL program (*/IDLWorkbench71/Grib_data/cal_split_height.pro*) is used to call Wgrib2, extract the meteorological profiles and calculate the height of dividing stream line that meets the equation of Sheppard's model. Usually, grib2 data have 10-15 vertical levels from ground to the height of PMO. The program does the calculation iteratively starting from the lower layer and performs an interpolation between the layer below or exceed the requirements in Sheppard's model. Both mechanical lifting and latent heat released by cloud formation during lifting are considered in the calculation. */IDLWorkbench71/Grib_data/doi_cal_split_height.pro* enables users to do the calculation for a given time period.

Planetary boundary layer (PBL) height can be obtained from a few sources, including GFS-grib2, GDAS-binary (<ftp://arlftp.arlhq.noaa.gov/pub/archives/gdas1>) and GEOS-5. */IDLWorkbench71/Grib_data/extract_pbl_height.pro* extracts PBL height from GFS data. */IDLWorkbench71/GDAS/read_gdas_pblh.pro* extracts PBL height from GDAS data. When running GEOS-Chem simulations, PBL height in GEOS-5 can be saved separately.

Appendix C

Letters of Permission

Chapter 2 is based entirely on the (Zhang et al., 2014). The author retains copyright of Atmospheric Chemistry and Physics (ACP) articles, which is indicated by the following webpage: http://www.atmospheric-chemistry-and-physics.net/general_information/license_and_copyright.html

License and copyright agreement

The following license and copyright agreement is valid for any article published by Copernicus Publications on behalf of the European Geosciences Union (EGU).

Author's certification

In submitting the manuscript, the authors certify that:

- They are authorized by their co-authors to enter into these arrangements.
- The work described has not been published before (except in the form of an abstract or proceedings-type publication – including discussion papers – or as part of a published lecture or thesis), that it is not under consideration for publication elsewhere, that its publication has been approved by all the author(s) and by the responsible authorities – tacitly or explicitly – of the institutes where the work has been carried out.
- They secure the right to reproduce any material that has already been published or copyrighted elsewhere.
- They agree to the following license and copyright agreement:


Copyright

- Authors retain the Copyright. Regarding copyright transfers please see below.
- Authors grant Copernicus Publications a license to publish the article and identify itself as the original publisher.
- Authors grant Copernicus Publications commercial rights to produce hardcopy volumes of the journal for sale to libraries and individuals.
- Authors grant Copernicus Publications and the Swiss Association of Geography (Association Suisse de Géographie) the right to distribute, reproduce, display, translate, and store the manuscript in all forms, as well as to sublicense the work for commercial purposes. This right shall be exclusive by 1 January of the year subsequent to the publication date.
- Authors are explicitly permitted to post the non-peer-reviewed manuscript (pre-print) as well as the unedited accepted manuscript (post-print) PDF of their articles (and/or supplemental material) on their personal website or in an online institutional repository provided the article in Atmospheric Chemistry and Physics is cited properly and a link to the original publication of the manuscript in Atmospheric Chemistry and Physics appears.
- Authors further retain the right to revise, adapt, present, or distribute the manuscript, as well as to prepare derivative works, provided that all such distribution is for noncommercial benefit and the proper citation of the manuscript in Atmospheric Chemistry and Physics appears together with a link to the original publication of the manuscript in Atmospheric Chemistry and Physics.
- Furthermore, the authors have the right to reprint the manuscript in any publication of which authors serve as an author or editor, under the condition that the manuscript in Atmospheric Chemistry and Physics is cited properly and that a link to the original publication of the manuscript in Atmospheric Chemistry and Physics is shown.
- Under this License and Copyright Agreement, authors grant to the general public, effective at the 1 January of the following year after publication of the edited manuscript in an online issue of Atmospheric Chemistry and Physics, the nonexclusive right to copy, distribute, or display the work subject to the terms of the [Creative Commons Attribution 3.0](#) License:


Creative Commons Attribution 3.0 License

Anyone is free:

 to Share — to copy, distribute and transmit the work

 to Remix — to adapt the work

Under the following conditions:

 **Attribution.** The original authors must be given credit.

- For any reuse or distribution, it must be made clear to others what the license terms of this work are.
- Any of these conditions can be waived if the copyright holders give permission.
- Nothing in this license impairs or restricts the author's moral rights.

The full [legal code](#) of this license.

Copyright transfers

Many authors have strict regulations in their contract of employment regarding their works. A transfer of copyright to the institution or company is usual as well as the reservation of specific usage rights. Please note that in case of Open Access publications in combination with a Creative Commons License a transfer of the **copyright** to the institution is possible as it belongs to the author anyway and is not subject to the publisher.

Any **usage rights** are regulated through the Creative Commons License. As Copernicus Publications is using the Creative Commons Attribution 3.0 License, anyone (the author, his/her institution/company, the publisher, as well as the public) is free to copy, distribute, transmit, and adapt the work as long as the original author is given credit (see above). Therefore, specific usage rights cannot be reserved by the author or his/her institution/company, and the publisher cannot include a statement "all rights reserved" in any published paper.

A copyright transfer from the author to his/her institution/company will be expressed in a special "Copyright Statement" at the end of the publication rather than on the first page in the article citation header. Authors are asked to include the following sentence: "The author's copyright for this publication is transferred to *institution/company*".

Crown copyright

The license and copyright agreement of Copernicus Publications respects the Crown copyright. For works written by authors affiliated with the British Government and its institutions, a copyright statement will be included at the end of the publication. Authors are asked to use the following statement, which has been approved by the Information Policy department of The National Archives:

The works published in this journal are distributed under the Creative Commons Attribution 3.0 License. This license does not affect the Crown copyright work, which is re-usable under the Open Government Licence (OGL). The Creative Commons Attribution 3.0 License and the OGL are interoperable and do not conflict with, reduce or limit each other.

© Crown copyright YEAR

Reproduction Request

All articles published by Copernicus Publications are licensed under the Creative Commons Attribution 3.0 License (see details above) together with an author copyright. Therefore, there is no need from the publisher's side to allow/confirm a reproduction. We would suggest contacting the author to inform him/her about the further usage of the material. But as the author decided to publish the scientific results under the "CC-BY" license, he/she decided to share the work under the condition that the original authors must be given credit.